National Library of Canada
Acquisitions and Bibliographic Services Branch
395 Wellington Street
Ottawa, Ontario
K1A 0N4

Bibliothèque nationale du Canada
Direction des acquisitions et des services bibliographiques
395, rue Wellington
Ottawa (Ontario)
K1A 0N4

Your file Votre référence

Our file Notre référence

NOTICE

The quality of this microform is heavily dependent upon the quality of the original thesis submitted for microfilming. Every effort has been made to ensure the highest quality of reproduction possible.

If pages are missing, contact the university which granted the degree.

Some pages may have indistinct print especially if the original pages were typed with a poor typewriter ribbon or if the university sent us an inferior photocopy.

AVIS

La qualité de cette microforme dépend grandement de la qualité de la thèse soumise au microfilmage. Nous avons tout fait pour assurer une qualité supérieure de reproduction.

S'il manque des pages, veuillez communiquer avec l'université qui a conféré le grade.

La qualité d'impression de certaines pages peut laisser à désirer, surtout si les pages originales ont été dactylographiées à l'aide d'un ruban usé ou si l'université nous a fait parvenir une photocopie de qualité inférieure.

Canada

Structural Investigations of Metastable Epitaxial Metallic Layers by Glancing-incidence X-ray Absorption Fine Structure

by

Detong Jiang

B.Sc. Jilin University, P.R.China, 1982

A THESIS SUBMITTED IN PARTIAL FULFILLMENT OF

THE REQUIREMENTS FOR THE DEGREE OF

DOCTOR OF PHILOSOPHY

in the Department

of

Physics

SIMON FRASER UNIVERSITY

November 1991

ISBN 0-315-83673-3

Approval

Name: Detong Jiang

Degree: Doctor of Philosophy

Title of Thesis: Structural Investigations of Metastable Epitaxial Metallic Layers by Glancing-incidence X-ray Absorption Fine Structure

Examining Committee:

Chairman: Dr. R. F. Frindt

Dr. E. D. Crozier
Senior Supervisor

Dr. B. P. Clayman

Dr. M. Plischke

Dr. B. Heinrich

Dr. S. M. Heald
External Examiner
Brookhaven National Laboratory

Date Approved: November 14, 1991

PARTIAL COPYRIGHT LICENSE

I hereby grant to Simon Fraser University the right to lend my thesis, project or extended essay (the title of which is shown below) to users of the Simon Fraser University Library, and to make partial or single copies only for such users or in response to a request from the library of any other university, or other educational institution, on its own behalf or for one of its users. I further agree that permission for multiple copying of this work for scholarly purposes may be granted by me or the Dean of Graduate Studies. It is understood that copying or publication of this work for financial gain shall not be allowed without my written permission.

Title of Thesis/Project/Extended Essay

Structural Investigations of Metastable Epitaxial Layers by Glancing-incidence X-ray Absorption Fine Structure

Author: _____
(Signature)

DETONG JIANG
(Name)

Nov. 18, 1991
(Date)

Abstract

Novel MBE-grown crystal structures of ultrathin epitaxial Ni films on Fe(001) and Cu on Ag(001) substrates have been studied using glancing-incidence x-ray absorption fine structure spectroscopy (XAFS). Reflection high energy electron diffraction and Auger electron spectroscopy were used to establish that the films grew epitaxially. In order to carry out the glancing-incidence XAFS measurements, a sample positioner was designed for aligning the sample in the synchrotron radiation. Detectors were also designed to permit acquiring the spectra in three modes: reflectivity, fluorescence and total-electron-yield. The interaction between the glancing-incidence x-rays and a multilayer system was considered theoretically and experimentally to establish a data analysis scheme.

It is shown that the Cu, 8 monolayers (ML) thick grown on Ag(001), is body centered tetragonal with the c-axis being expanded 7.6% relative to the a-axis. The significance of this result is in the context of using Cu as a buffer between two magnetically coupled ultrathin 3-d metal films.

Ni can be epitaxially grown on a Fe(001) surface in a metastable bcc structure up to 3 ~ 6 ML, then a phase transition occurs, but the structure is not stabilized until after 13 ML of Ni are grown. This thicker Ni has some unique magnetic properties including a 4^{th} order in-plane magnetic anisotropy which is more than 10 times larger than that of fcc Ni. Our Ni films had thicknesses 3, 6, 9 and 37 ML. The local atomic structure of both the stabilized phase (>13ML) and transition phase (<13ML) have been characterized. It is shown that the structure of the stabilized phase consists of local fcc building blocks and requires defects. For a transition state (9ML) it is shown that there is an intermediate local structure different from either bcc or fcc. These results lead to the proposing of a defect-induced model for the observed magnetic properties.

Acknowledgements

I would like to thank my supervisor, Prof. E.Daryl Crozier, for his sustained support and encouragement during the course of this work. It has been an educational experience to have worked with him.

I am indebted to Dr. Neil Alberding for useful advices on numerous occasions. Neil's work on the structure of epitaxial thin films was a starting point for me. Thanks go to Andrew Seary and Dr. K. Rudolf Bauchspiess for the data analysis programs used in this work and for many helpful suggestions regarding computing and data analysis.

Dr. Bretislav Heinrich introduced me to the field of molecular beam epitaxy. I thank him for many useful discussions and for the time he spent with me. I also thank Dr. Stephen Purcell and Ken Myrtle for their valuable advice and help in sample preparations.

I thank my wife and my fellow student, Xiaorong Qin, for her support which helped me out in many occasions and for her artistic touches on most of the drawings in the thesis which made the work much more presentable.

To machinists Ken Stowe and Don Smith, and machine shop supervisor Frank Wick and Les Bird goes my gratitude for their valuable suggestions in building the apparatus used in this work.

I wish to thank the members of my examining committee for their comments on this thesis. I also wish to thank my external examiner Dr. S.M. Heald. His initial work on the contributions of anomalous dispersion to glancing-incidence absorption spectra motivated the analysis in Chapter II of this thesis.

Sincere thanks go to my mother Qiying Duan and my mother-in-law Changchun Wu for their understanding, patience and moral support during my writing of this thesis.

Finally, I gratefully acknowledge the generous financial support provided by Simon Fraser University and Jilin University.

Table of Contents

List of Tables

List of Figures

Chapter II

Chapter III

Chapter IV

Chapter V

Chapter VI

Chapter I. Introduction

Artificially altering what nature can offer to obtain new physical properties, magnetic properties in particular, is of great interest in both science and technology. One way of achieving this is by applying the molecular-beam expitaxy (MBE) technique to generate and stabilize metallic metastable structures. Such structures have attracted increasing interest in recent years. Under the well-controlled MBE conditions, atoms of one element can be deposited onto a suitable template crystal substrate of another element in a layer-by-layer fashion following a particular atomic registry which does not exist otherwise in nature. In general, this kind of oriented growth of one crystal upon another is referred to as epitaxial growth. In the case of layered 3d transition metal systems, novel crystalline structures with various interesting magnetic properties have been engineered.[1-5]

To understand thoroughly the properties of the metastable films, it is obviously crucial to characterize the structure in detail. Various surface structure techniques have been applied in this field. Reflection high-energy electron diffraction, RHEED, is used during the growth to monitor the film thickness,[6] in-plane lattice constants and symmetry.[7] However, under the current level of understanding of RHEED, one can not accurately obtain the lattice spacing perpendicular to the surface, nor can one determine the arrangement of different atomic species in the surface unit cell. X-ray photoelectron diffraction, XPD,[8] has been used to determine relative lattice expansions and contractions in the surface normal direction.[9] It involves intrinsically an electron multiple scattering process, and consequently it is limited to the study of the top 2 to 4 monolayers of a noncovered surface.[10] The quantitative interpretation of low-energy electron diffraction (LEED) patterns requires a thorough consideration of electron multiple scattering but it is a more established technique and has been applied to some metastable metallic films.[11-15] In the case of Ni on Fe(001) LEED studies showed that Ni grows in a pure bcc structure up

to 6 monolayers (ML), but the attempt to decipher the structure of thicker Ni films, which stabilize after 13 ML and retain the same structure up to more than 100 ML, was not successful.[11] In contrast to the complex quantitative analysis of LEED, x-ray diffraction can be interpreted by relatively simple kinematic theories. Normally x-rays are not regarded as a surface sensitive tool due to the large penetration depth (~ micrometers). However, when combined with the glancing-incidence technique (see chapter II), x-rays can have a surface sensitivity of the first 20-30 Å that is comparable to other surface techniques. This glancing-incidence x-ray technique has been exploited in reflectivity, diffraction and x-ray-absorption to study surfaces and interfacial regions. Glancing-incidence (also referred to as grazing-incidence) x-ray diffraction has been shown to be very powerful in determining the structure of reconstructed surfaces[16-20] when the noninteger indexes of the surface Bragg rods can be easily separated from the bulk signal. In principle, the technique is also applicable to the epitaxial ultrathin films.

The technique to be discussed in this thesis, X-ray absorption fine structure (XAFS) which includes both extended X-ray absorption fine structure (EXAFS) and X-ray absorption near edge structure (XANES), has also been applied to epitaxially-grown films.[21-27] Being a local atomic structure probe, XAFS has difficulty in solving a crystal structure independently. But, by the same token, it can provide valuable complementary structural information which is difficult to obtain by the long-range-order diffraction techniques. Information of the nearest and the second nearest neighboring shells provided by XAFS can be used to distinguish easily different close-packed structures such as bcc and fcc for 3-d metal ultrathin films and, to characterize the distortion of the lattice when it occurs. The XAFS technique is intrinsically element selective, therefore the information of two neighboring ultrathin films (e.g. Ni/Fe bilayers on a substrate and covered with another passive layer) can be unambiguously separated and studied independently. One can have a higher level understanding of the system under consideration if the information from both diffraction and XAFS are available.[28]

In this thesis novel MBE-grown crystal structures of ultrathin epitaxial Ni films on bulk Fe(001) or Fe/Ag(001) and Cu on bulk Ag(001) were investigated using glancing-incidence XAFS. The thickness of the films varied from 3 ML to 37 ML. Reflection High Energy Electron Diffraction (RHEED) and Auger Electron spectroscopy (AES) were used to establish that the films grew epitaxially (see chapter IV). In order to carry out the glancing-incidence XAFS measurements, a sample positioner[23] was designed for placing the sample in the synchrotron radiation (SR) with the incident angle adjustable in steps of 13.5 μrad. Fluorescence and total-electron-yield detectors[29] were also designed to permit acquiring the spectra simultaneously in three modes: fluorescence, total-electron-yield and reflectivity (see chapter III).

XAFS data obtained in the glancing-incidence mode differ from that obtained in a standard mode such as transmission. That is because the anomalous dispersion effects accompanied with glancing-incidence often have a non-negligible effect on the EXAFS amplitude and distort the XANES. In a favorable case, such as thick films (several hundred Å) evaporated on glass, the effect of the anomalous dispersion can be corrected quantitatively as demonstrated by Martens and Rabe in the reflectivity case and, by Heald, Chen and Tranquada in the fluorescence yield case.[30] In both of these cases, flat glass surfaces ensured that the x-ray reflectivity curves could be explained quantitatively by a relatively simple model.[31] This was essential for the effect of anomalous dispersion in XAFS to be taken into account reliably.

In our samples, the surfaces of the metal substrates were not as macroscopically flat as that of float glass and the total film thickness was not large enough to show any clearly identifiable features such as the Kiessig fringes [32]which could help the theoretical fitting. Therefore it was difficult to extract necessary parameters for doing the correction quantitatively. To establish the upper bound of the errors introduced by the anomalous dispersion, we expanded Parratt's theory [31] to calculate the electric field distribution in the sample with the anomalous scattering factors computed using the Cromer and Liberman

relativistic anomalous scattering factor program.[33-35] Heald's correction scheme[30] was then applied to obtain the EXAFS phase and amplitude corrections in various modeled structures (see chapter II). Our results indicate that in the thin film limit (< 10 ML) the spectrum obtained in the glancing-incidence mode is virtually distortion free. For somewhat thicker films, e.g. 37 ML of Ni on Fe, interatomic distances and the ratio of coordination numbers can be readily extracted from the data without relying on the amplitude correction.

Ni epitaxially grown on a Fe(001) surface is one of the few systems in which the overlayers are forced by the substrate template to form a new metastable phase. For less than 3-6 ML, Ni grows in a bcc structure with the same lattice constants of the Fe substrate.[11] Above this critical thickness region, RHEED and LEED studies showed that there is some sort of structure modulation of the initially pure bcc Ni structure indicated by some superlattice patterns, but no definitive conclusions could be drawn from either technique.[11, 12, 36] For Ni overlayers thicker than 13 ML, Ni was in a stabilized structure state again as indicated by both the same LEED and RHEED studies. This structure lasts to a thickness of at least 100 ML. In this state, the RHEED patterns indicative of the structure modulation started around 6 ML and became stronger but they were always much weaker than the original patterns from the bcc structure.

The bcc Ni (first 3-6 ML) was of interest to surface science since it was a new phase of Ni. However, it was the structure modulated Ni overlayers that were more attractive because they possess a 4^{th} order in-plane magnetic anisotropy which is more than 10 times larger than that of fcc Ni.[37] From the structural characterization point of view, the questions to be answered at the time were: (1) Does the structure modulated Ni still have a bcc structure and do those weak additional RHEED and LEED superlattice patterns simply mean a surface reconstruction or some sort of minor distortion of the basic bcc lattice? (In fact the initial purpose of applying EXAFS to the system was to try to provide a positive answer to this question.); (2) What are the structural differences between the transition state (above 6 ML and below 13 ML) and the stabilized state (above 13 ML)? Our XAFS results

on the Ni/Fe systems indicate that in the stabilized state Ni (e.g. 37 ML) has a local structure almost identical to that of fcc Ni metal and in the transition state Ni (e.g. 9 ML) has a local structure distinctly different from either bcc Fe or fcc Ni (see chapter V).

The second system (see chapter VI) studied in this thesis is a single 8 ML Cu film epitaxially grown on a Ag(001) surface and covered with 10 ML of Au. The structure of the Cu in the Cu/Ag(001) system as determined by using XPD and RHEED has been reported[4, 9] to be close to bcc. This system is important in the context of the magnetic behavior of Fe/Cu/Fe trilayers on Ag(001). Heinrich and coworkers have shown that the exchange coupling depends on the thickness of the Cu interlayer, changing from ferromagnetic to antiferromagnetic for greater than 8 ML of Cu.[4] Initial theoretical attempts to explain the antiferromagnetism assuming a pure bcc structure of Cu were unsuccessful.[38] Our EXAFS shows that the Cu is body centered tetragonal with the c-axis (perpendicular to the substrate) being expanded 7.6% relative to the a-axis and a-axis lattice constant being 2.88 Å.

The material in this thesis is organized in the following way. Chapter II provides some basic information about XAFS and the glancing-incidence technique. Chapter III describes the instruments and methods used in the glancing-incidence XAFS measurements. The sample preparation and related MBE techniques are discussed in chapter IV. The experimental data are analyzed and the results discussed in chapter V and VI for Ni/Fe and Cu/Ag systems respectively. Finally chapter VII provides some general remarks about the technique and suggests future work.

Chapter II. Theoretical Aspects of Glancing-incidence XAFS

In this chapter we first briefly review the EXAFS formula, then we discuss in some detail the interaction between plane wave x-rays and a stratified system under glancing-incidence geometry. Finally we combine the two techniques, i.e. EXAFS and glancing-incidence together and discuss three different detection methods.

II.1) Principles of the XAFS technique

When a monochromatic x-ray wave is incident on an atom, the absorption coefficient, μ, of the atom can be described by Fermi's Golden Rule within the dipole approximation* for the photon-induced transition of an electron from an initial state $|i>$ to a final state $|f>$:[1]

$$\mu = \frac{4\pi^2\omega e^2}{c} |<f|\varepsilon\cdot\mathbf{r}|i>|^2 \rho(E) . \qquad \text{(II-1)}$$

Here ε is the polarization vector of the electric field and $\mathbf{r}$ is the electron coordinate, $\rho(E)$ is the density of final states, $E = E_i + \hbar\omega$ where E_i is the energy of $|i>$ and $\hbar\omega$ is the photon energy.

If the absorbing atom has no neighboring atoms, such as in a monoatomic gas, μ would be a smooth function of energy above the absorption edge threshold. In the presence of neighboring atoms, however, the outgoing part of the photoelectron wave may be reflected back toward the origin. Since the initial state $|i>$ at the origin is highly localized, the matrix element in (II-1) will be modulated by well-defined interference between the outgoing and backscattered wave which results in some oscillating fine structure as a function of the incident photon energy $\hbar\omega$ as shown in Fig. 1. The fine structure is usually referred to as x-ray absorption fine structure (XAFS). The higher energy part is usually

---

* Usually the initial state $|i>$ involved in XAFS is a deep core state, e.g. K-edge as to be discussed in this thesis. In this case the wavelength of the x-ray is much larger than the size of the initial state, i.e. the dipole approximation is valid.

referred to as extended x-ray-absorption fine structure (EXAFS) while the lower energy part is referred to as x-ray-absorption near edge structure (XANES).

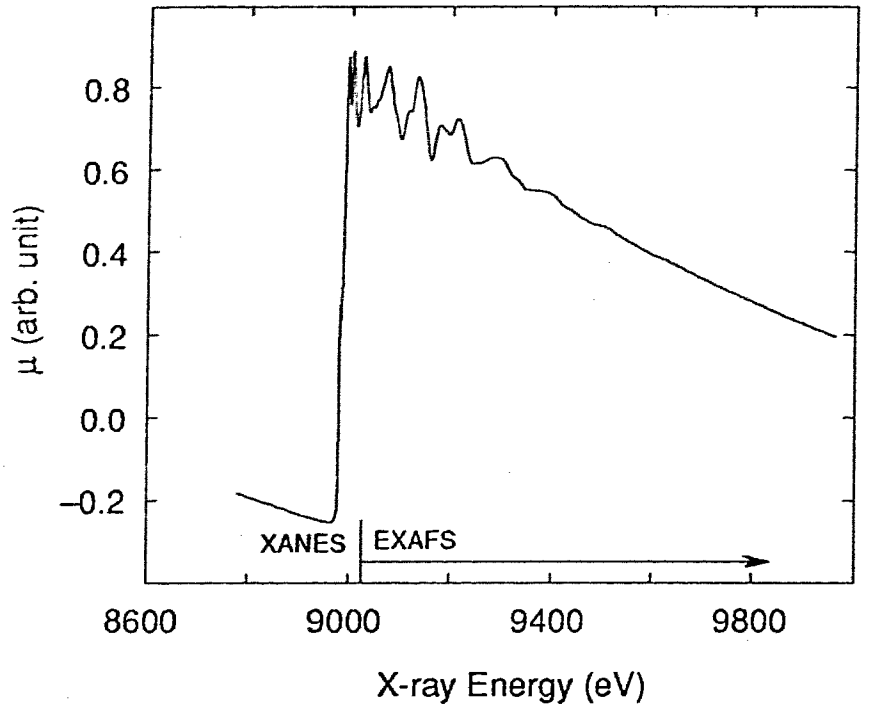

Fig. 1 A K-edge x-ray absorption spectrum of Cu metal, the ranges of XANES and EXAFS are loosely indicated.

EXAFS is well understood and has been applied widely in many fields of science. Comparatively, a quantitative interpretation of XANES is not that straightforward. In the language of scattering theory, the basic difference between the two parts of the absorption spectrum is that in EXAFS a single scattering theory is usually sufficient due to the high energy of the excited electrons, while in XANES one would have to face a multiple scattering question.[2] In this work we will focus on the application of EXAFS while using XANES only in a qualitative way by comparing the unknown with the references.

In EXAFS the frequency of the oscillatory modulation in μ as a function of incident photon energy is determined by the internuclear distance between the absorbing and neighboring atoms and the amplitude of the oscillatory modulation is related to the species

and coordination of the neighboring atoms. Introducing a dimensionless function of x-ray photon energy χ to describe the oscillatory part, we have

$$\mu = \mu_o (1 + \chi) \qquad \text{or} \qquad \chi = \frac{\mu - \mu_o}{\mu_o} \tag{II-2}$$

where μ_o is the absorption of an isolated atom.

The commonly used K-edge expression of χ for a crystalline sample in the limit of small disorder is given by[3]

$$\chi(k) = \sum_j \frac{3 \cos^2\theta_j}{kR_j^2} \, | f_j(k) | \, S_0^2 \, e^{-2k^2\sigma_j^2} \, e^{-2R_j/\lambda} \sin [2k(R_j - \Delta_j) + \phi_j(k)] \, , \tag{II-3}$$

where the sum is over all the neighboring atoms. In (II-3), R_j is the mean internuclear distance between the central (absorbing) atom and the jth neighbor atom; σ_j^2 is the mean-squared relative displacement in R_j ; θ_j is the angle between the jth bond and the x-ray polarization direction; k is the photoelectron wave number, i.e. $k = [2m_e (\hbar\omega - E_o)]^{1/2}/\hbar$ where m_e is the electron mass and E_o the electron binding energy; $| f_j(k) |$ is the magnitude of the back-scattering amplitude of the jth neighbor and $\phi_j(k) = central_j(k) + back_j(k)$ is the scattering phase shift due to the central and the back-scattering atom. $\Delta_j = 2\sigma_j^2(\frac{1}{R_j} + \frac{1}{\lambda})$ is the correction due to the approximation of ignoring the variance of R_j in the term $1/R_j^2$ and $e^{-2R_j/\lambda}$ in the radial distribution function.[4] This correction term normally is rather small, for example in the case of bulk Cu at room temperature it is ~ 0.007Å.

$e^{-2R_j/\lambda}$ is a phenomenologically added term to describe the damping due to the lifetime of the final state of the photoelectron in terms of a mean free path λ . S_0^2 is a slowly-varying dimensionless function of k which describes the reduction of the EXAFS signal due to multiple excitation effects.

For polycrystalline cases (II-3) is usually written as

$$\chi(k) = \sum_j \frac{N_j}{kR_j^2} \, | f_j(k) | \, S_0^2 \, e^{-2k^2\sigma_j^2} \, e^{-2R_j/\lambda} \sin [2k(R_j - \Delta_j) + \phi_j(k)] \, , \tag{II-3a}$$

where j sums over atomic shells and N_j is the coordination number in the J^{th} atomic shell.

In deriving (II-3) a plane wave assumption for the x-ray induced photoelectron was made.[3] Curved wave effects can be easily included while the formalism of (II-3) is kept the same.[5, 6] When the curved wave effects are considered the amplitude $f_j(k)$ and $\phi_j(k)$ are replaced by $f_j(k,R)$ and $\phi_j(k,R)$, but the R-dependence is small.

The $f_j(k)$ and $\phi_j(k)$ in (II-3) can be either extracted from a reference system or calculated from first principles. With this knowledge the EXAFS data $\chi(k)$ or its Fourier transform can be curve fitted or analyzed by using Fourier filtering technique to get the structure parameters: R_j, the coordination number of neighboring atoms N_j and σ_j^2. [7]

II.2) Principles of the X-ray Glancing-incidence Technique

II.2.1) The medium parameters

In the x-ray frequency range the permeability of a solid $\mu \approx 1$ to a very good approximation. This is true for ferromagnetic material as well. When considering the interaction of an electromagnetic wave with matter, the effect of the magnetic field on the electrons in an atom is always much smaller than the effect of the electric field. That is because the electron speed v in an atom is much smaller than c, so $| \frac{e}{c} \mathbf{v} \times \mathbf{B} | / | e\mathbf{E} | \sim \frac{v}{c} \ll 1$, i.e. the magnetic force on the electron is much smaller than that of the electric field. So throughout this thesis whenever the interaction of x-ray and solids is concerned the materials are treated as if they are always nonmagnetic ($\mu \approx 1$) and the effect of the magnetic field is neglected.

The simplest model of a solid is a fixed assembly of independent neutral atoms. The effect of a monochromatic electromagnetic wave on such a system is described by a complex dielectric constant given as the following [8-10]

$$\varepsilon(\omega) = 1 + \frac{4\pi Ne^2}{m_e} \sum_{j,n} \frac{f_{jn}}{(\omega_{jn}^2 - \omega^2) - i\omega\Gamma_{jn}}, \qquad \text{(II-4)}$$

where m_e and e are the mass and charge of an electron, $\omega = 2\pi\nu$ where ν is the frequency of the incident electromagnetic wave and N is the number of atoms per unit volume. In (II-4) the oscillator strength $f_{jn} = \frac{2m}{\hbar^2} \hbar\omega_{jn} | x_{jn}|^2$, where $x_{jn} = < j | x | n >$ is the transition probability matrix element between the initial state $| n >$ and possible unoccupied states $| j >$ of the atom (the electric field vector is assumed to be along the x axis) , $\hbar\omega_{jn}$ is the energy difference between the two states and Γ_{jn} is introduced phenomenologically to describe the broadening of the states. [11] The sum over j is to be taken over all possible unoccupied states including integration over the continuum of positive energy states. The subscript n stands for the electron groups K,L,M,... i.e. different initial states in the atom. The above formula is for a case of one atomic species present, otherwise another sum over atomic species is needed. Again, in deriving (II-4) the dipole approximation is applied and the effect of the magnetic field is neglected.

It is customary to rewrite formula (II-4) in terms of the atomic-scattering factor $f = f_o + f' + if''$, where f_o equals the atomic number in the coherent [12] forward scattering case [13] and f' and f'' are the real and imaginary anomalous scattering corrections respectively:

$$\varepsilon(\omega) = 1 - \frac{4\pi Ne^2}{m_e\omega^2} (f_o + f' + if'') . \qquad \text{(II-4a)}$$

Since the refraction index $n = \sqrt{\varepsilon(\omega)}$ and the second term in (II-4a) is of the order of 10^{-5} or less, upon neglecting the higher order terms we have

$$n = 1 - \delta - i\beta , \qquad \text{(II-5)}$$

$$\text{with} \quad \delta = \frac{N_o}{2\pi} \frac{e^2}{m_e c^2} \frac{\rho}{M} \lambda^2 (f_o + f'),$$

$$\beta = \frac{N_o}{2\pi} \frac{e^2}{m_e c^2} \frac{\rho}{M} \lambda^2 f''.$$

From (II-4) to (II-5) the substitutions $N = N_o \frac{\rho}{M}$ and $\omega = \frac{2\pi c}{\lambda}$ have been used, where N_o is Avogadro's number, ρ the mass density, M the atomic weight and λ the wavelength of the x-ray. The anomalous scattering corrections f' and f'' used in this work were computed with the Cromer and Liberman relativistic anomalous scattering factor program. [14-16] The method used in making those calculations was essentially the same as that given in formula (II-4).[14]

II.2.2) The Electric field in a stratified system in the glancing-incidence geometry

A theoretical calculation of the reflectivity from a stratified homogeneous system in an x-ray glancing-incidence case was first given by Parratt. [17] In this section the same approximations of Parratt's are used and the calculation is extended to get the electric field distribution everywhere in the stratified system. Hence the x-ray fluorescence yield signal as well as the reflectivity can be calculated.

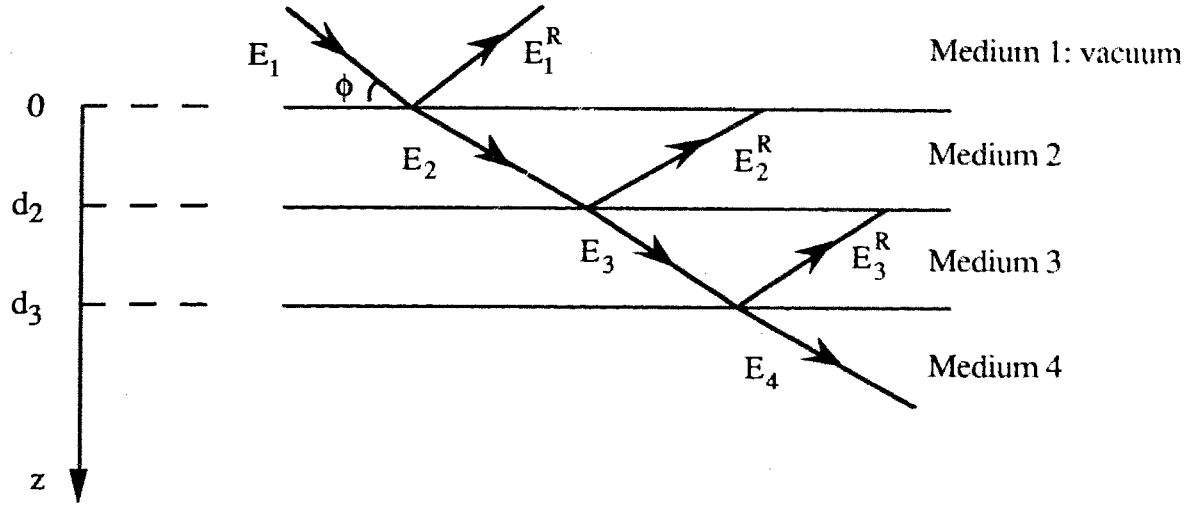

Fig. 2 A schematic view of the electric field distribution in a stratified system. The notations for the field amplitudes are explained in the text, the electric vector is perpendicular to the paper, the arrows indicate the direction of the wave vector and d_m (m = 1,2,...) is the depth of the (m,m+1) interface.

When a monochromatic x-ray is incident onto the interface of vacuum and a stratified system as schematically shown in Fig. 2, the expressions for the amplitudes of the electric field of the incident beam $E_1(z_1)$, of the reflected beam $E_1^R(z_1)$, and of the refracted beam $E_2(z_2)$ at a perpendicular distance z from the surface are

$$\begin{aligned} E_1(z_1) &= E_1(0) \exp i\,[\,\omega t - (k_{1,x} x_1 + k_{1,z} z_1)\,] \\ E_1^R(z_1) &= E_1^R(0) \exp i\,[\,\omega t - (k_{1,x} x_1 - k_{1,z} z_1)\,] \\ E_2(z_2) &= E_2(0) \exp i\,[\,\omega t - (k_{2,x} x_2 + k_{2,z} z_2)\,]\,, \end{aligned} \qquad \text{(II-6)}$$

where $k_1 = \frac{\omega}{c}$ and $k_2 = \sqrt{\varepsilon_2}\,\frac{\omega}{c} = n_2\,\frac{\omega}{c}$ are the wave numbers in vacuum and the first layer respectively, z is taken as positive into the sample, and the (x, z) plane is the plane of incidence, refraction, and reflection of the beam. In the case of glancing-incidence ($\varphi \sim$ a few miliradians) we have

$$k_{2,x}^2 + k_{2,z}^2 = k_2^2 = n_2^2 k_1^2 = n_2^2 (k_{1,x}^2 / cos^2\varphi) \approx k_{1,x}^2 (1 - 2\delta_2 - 2i\beta_2 + \varphi^2) . \quad \text{(II-7)}$$

In the last step above we have neglected the second and higher powers of δ_2 and β_2, and neglected the fourth and higher powers of φ.

From the boundary condition for the tangential components of the wave vectors [18, 19], $k_{2,x} = k_{1,x}$, and with the approximation $k_{1,x} \approx k_1$ for small φ, it follows from (II-7) that

$$k_{2,z} \approx k_1 (\varphi^2 - 2\delta_2 - 2i\beta_2)^{1/2} . \quad \text{(II-8)}$$

For convenience, we introduce

$$f_2 = (\varphi^2 - 2\delta_2 - 2i\beta_2)^{1/2} . \quad \text{(II-9)}$$

Using the same argument of (II-7) to (II-9), we have the following general relation between the wave number of the m^{th} layer and that of vacuum

$$k_{m,z} \approx k_1 f_m , \quad \text{with} \qquad f_m = (\varphi^2 - 2\delta_m - 2i\beta_m)^{1/2} , \quad \text{(II-10)}$$

where ϕ is the x-ray glancing-incident angle at the first interface (see Fig. 2). Then the expression for the refracted beam in the m^{th} layer becomes

$$E_m(z_m) = E_m(0) \exp i [\omega t - k_{m,x} x_m] \bullet \exp [-i k_1 f_m z_m] . \quad \text{(II-11)}$$

The dynamic properties are contained in the boundary conditions on the total fields: normal components of **D** and **B** are continuous; tangential components of **E** and **H** are continuous. For a wave with non-zero ω only two of the above four conditions are independent, so we need only consider the conditions on the tangential components,

$$(\mathbf{E}_{1,total} - \mathbf{E}_{2,total}) \times \mathbf{n} = 0 , \quad \text{(II-12)}$$

$$(\mathbf{H}_{1,total} - \mathbf{H}_{2,total}) \times \mathbf{n} = 0. \quad \text{(II-13)}$$

By noticing that $\mathbf{H} = \sqrt{\varepsilon}\, \mathbf{k} \times \mathbf{E}$, and after making similar approximations concerning small terms in δ, β and φ as we did previously in this section, in the case of the electric vector

perpendicular to the incident plane the continuity of the tangential components of the electric and magnetic fields for the m-1, m boundary may be expressed as

$$a_{m-1}E_{m-1} + a_{m-1}^{-1}E_{m-1}^{R} = a_m^{-1}E_m + a_m E_m^{R} , \tag{II-14}$$

$$(a_{m-1}E_{m-1} - a_{m-1}^{-1}E_{m-1}^{R})f_{m-1} = (a_m^{-1}E_m - a_m E_m^{R})f_m , \tag{II-15}$$

where the amplitude factor a_m for half the perpendicular depth d_m is, from Eq. (II-11),

$$a_m = \exp(-ik_1 f_m \frac{d_m}{2}) = \exp(-i\frac{\pi}{\lambda} f_m d_m) . \tag{II-16}$$

In Eqns. (II-14) and (II-15), the field amplitudes E_{m-1}, E_{m-1}^{R}, and E_m, E_m^{R} refer to the values midway through medium m-1 and m , respectively. The above boundary conditions are derived for the situation that the electric vector is perpendicular to the incident plane, which is always the case in this thesis. As a matter of fact, under the glancing-incidence case these two equations also hold for the electric vector parallel to the incident plane to a good approximation.

To describe the behavior of the incoming beam at the interface m - 1, m, we define the *reflection coefficient* $R_{m-1,m}$ and *transmission coefficient* $T_{m-1,m}$ as the following

$$R_{m-1,m} = \frac{a_{m-1}^{-1}E_{m-1}^{R}}{a_{m-1}E_{m-1}} , \tag{II-17}$$

$$T_{m-1,m} = \frac{a_m^{-1}E_m}{a_{m-1}E_{m-1}} . \tag{II-18}$$

The field amplitudes $a_{m-1}E_{m-1}$, $a_{m-1}^{-1}E_{m-1}^{R}$ and $a_m^{-1}E_m$ are the values *at the interface* of the incident, reflected and refracted beams respectively.

Now we can solve the boundary equations (II-14) and (II-15) for the coefficients defined above. By dividing the difference of (II-14) and (II-15) by their sum and substituting in the definition of $R_{m-1,m}$ we have

$$\frac{(1-f_{m-1})+(1+f_{m-1})R_{m-1,m}}{(1+f_{m-1})+(1-f_{m-1})R_{m-1,m}}=\frac{(1-f_m)a_m^{-4}+(1+f_m)R_{m,m+1}}{(1+f_m)a_m^{-4}+(1-f_{m-1})R_{m,m+1}}, \qquad \text{(II-19)}$$

and then by rearranging terms we have a recursion formula

$$R_{m-1,m}=\frac{a_m^4 R_{m,m+1}+G_{m-1,m}}{a_m^4 R_{m,m+1}G_{m-1,m}+1} \qquad (m=2,3,4,\ldots,l), \qquad \text{(II-20)}$$

where $$G_{m-1,m}=\frac{f_{m-1}-f_m}{f_{m-1}+f_m}. \qquad \text{(II-21)}$$

To get a generic formula for $T_{m-1,m}$, we divide (II-14) by $a_{m-1}E_{n-1}^R$ and use definitions (II-17) and (II-18):

$$\begin{aligned}1+R_{m-1,m}&=T_{m-1,m}+\frac{a_m}{a_{m-1}}\frac{E_m^R}{E_{m-1}}\\&=T_{m-1,m}+a_m^4\left(\frac{a_m^{-1}}{a_m}\frac{E_m^R}{E_m}\right)\left(\frac{a_m^{-1}}{a_{m-1}}\frac{E_m}{E_{m-1}}\right)\\&=T_{m-1,m}+a_m^4 R_{m,m+1}T_{m-1,m},\end{aligned}$$

so $$T_{m-1,m}=\frac{1+R_{m-1,m}}{1+a_m^4 R_{m,m+1}}. \qquad \text{(II-22)}$$

From the recursion equations, (II-20) to (II-22), we see that if R at one interface is known then the R and T at every interface can be calculated accordingly, provided that the

optical constants δ and β of each medium are available. Notice that the thickness of the substrate (the l^{th} medium) is always infinite, so there is no reflected beam in this layer, i.e. $R_{l,l+1} = 0$. So starting at the bottom medium we can use (II-20) and (II-22) to calculate the reflection and transmission coefficient at every interface. Thus the *reflectivity* of the system - the ratio of reflected to incident intensity, $|R_{1,2}|^2 = |E_1^R/E_1|^2$ can be calculated as well (note: $|a_1| = 1$).

Now we can write down the expression for the amplitude of the electric field of the glancing-incident wave in the stratified system in terms of "known" quantities. Using definitions (II-17) and (II-18) and referring to Fig. 2, we have

for refracted beam at boundary m-1, m: $$E_m(d_{m-1}) = E_{m-1}(d_{m-1})T_{m-1,m}\,, \qquad \text{(II-23)}$$

for reflected beam at boundary m-1, m: $$E^R_{m-1}(d_{m-1}) = E_{m-1}(d_{m-1})R_{m-1,m}\,, \qquad \text{(II-24)}$$

and the total field at depth z:

$$E_{m,total}(z) = E_m(d_{m-1})exp[-i\frac{\pi}{\lambda}f_m(z-d_{m-1})] + E^R_m(d_m)exp[-i\frac{\pi}{\lambda}f_m(d_m-z)]. \qquad \text{(II-25)}$$

where m is greater or equal to 2. This leaves d_1 undefined. Although the thickness of the vacuum layer is irrelevant (because there is no absorption in the vacuum), for consistency of the expressions and ease of programming we define $d_1 = 0$. Then the incident and reflected wave amplitude in vacuum may be expressed as $E_1(0)$ and $E_1^R(0)$ respectively. The intensities corresponding to these two quantities are directly measurable.

In Fig. 3 several calculated quantities for the interface of vaccum and bulk Cu are plotted to show the surface sensitivity of the glancing-incidence technique.

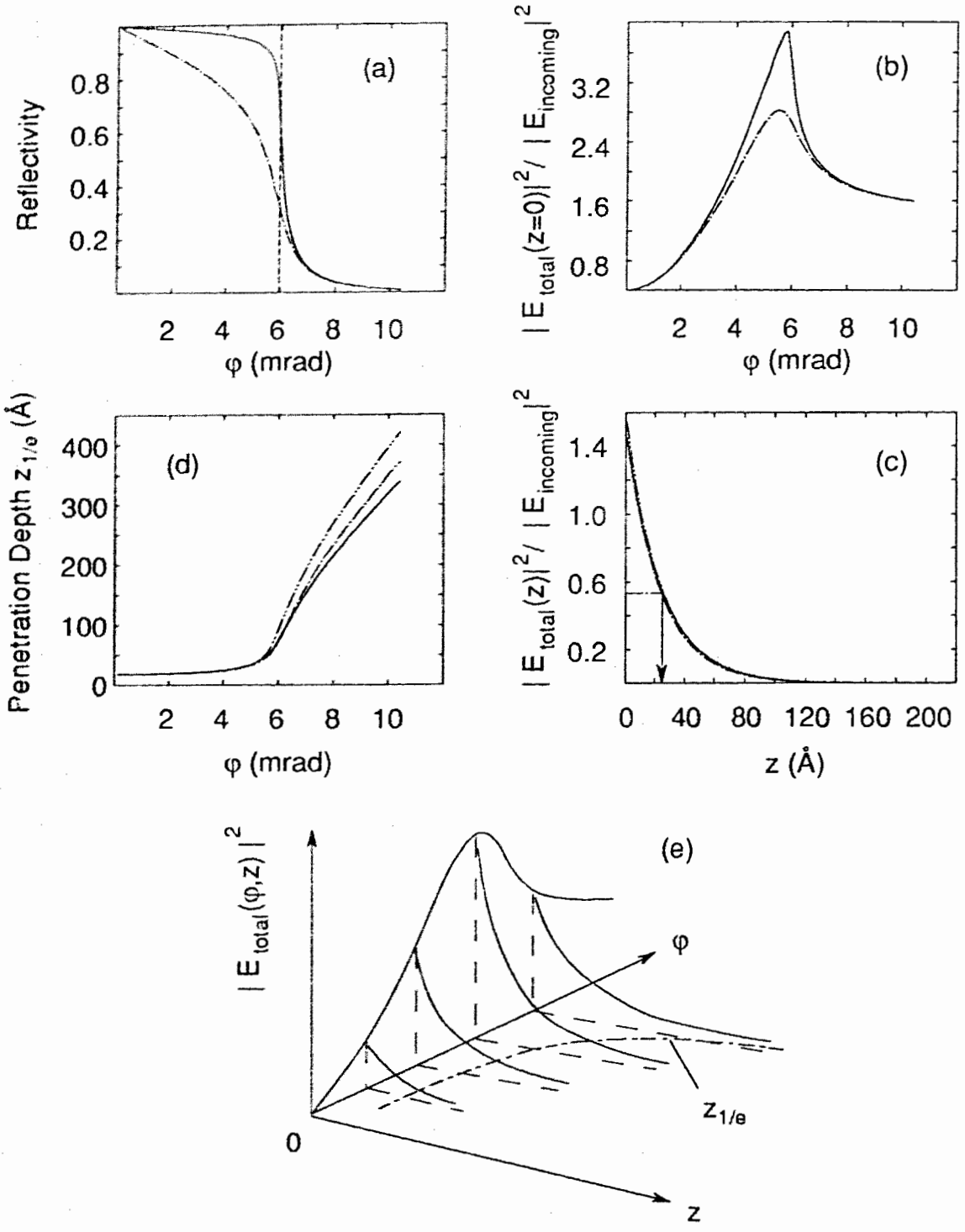

Fig. 3 (a) Reflectivity: $|R_{1,2}|^2 = |E_1^R/E_1|^2$ for 8930 eV(solid) and 9030 eV (dash-dot); (b) normalized electric field intensity at the surface as a function of the incident angle for 8930 eV(solid) and 9030 eV (dash-dot); (c) the normalized electric field intensity distribution along z direction for 9030 eV (solid), 9330 eV (dash-1 dot) and 9730 eV (dash-2 dots); (d) the penetration depth as a function of the incident angle for the same three x-ray energies as in (c); (e) A sketch (not drawn to scale) of the relationships between the quantities plotted in (b), (c) and (d).

Fig. 3(a) shows the reflectivity as a function of incident angle for two photon energies, 8930 eV (solid) and 9030 eV (dash-dot) which are 50 eV below and above the Cu K-edge respectively. When $\varphi < \varphi_c = \sqrt{2\delta}$, which is usually called the critical angle and is indicated by the vertical dash line in the graph, there is total external reflection of the x-ray, i.e. R $\rightarrow$ 1. φ_c varies inversely with the photon energy. The separation between the critical angles of the two energies is too small to be shown on the graph. For the lower energy curve we have R $\approx$ 1 at the low incident angles then a sharp cutoff occurs when $\varphi \rightarrow \varphi_c$. However the position of φ_c on the high photon energy curve is not that distinct, the transition around φ_c is much more gradual. This is a manifestation of the effect of the K-edge absorption. The normalized electric field intensity in the sample at $z = 0$ is shown in Fig. 3(b) as a function of incident angle. Here we see that as $\varphi \rightarrow \varphi_c$ the intensity is ~3 times larger than that of the incident wave.[20] This effect further enhances the power of the glancing-incidence technique. In Fig. 3(c) the field intensity in the sample as a function of the depth into the sample is shown. We can see that the evanescent wave intensity decays exponentially with increasing depth and most of the intensity is confined in the region within 20 ~ 30 Å of the surface.The x-ray incident angle for the case shown is $\frac{2}{3}\varphi_c$ and there are actually three curves plotted for 9030 eV (solid), 9330 eV (dash 1 dot) and 9730 eV (dash 2 dots) respectively. These three energies represent roughly the start (3.6 $Å^{-1}$), the middle (9.6 $Å^{-1}$) and the end (14 $Å^{-1}$) of a typical EXAFS spectrum. We see clearly that the depth profile of the electric field does not spread much over this wide energy range, i.e. the sampling depths are about the same at different energies. The penetration depth $z_{1/e}$ is defined to be the depth at which the intensity is reduced to $1/e$ of the value at $z = 0$ inside the sample. In (c) the depth is indicated by a arrow shared by all the three energies (the difference is less than 1 Å). In Fig. 3(d) the penetration depths $z_{1/e}$ are shown as a function of the incident angle for the three energies as in (c). It can be seen from the graph that at angles less than φ_c the $z_{1/e}$ is approximately independent of the photon energy as seen in

(c). In addition from this graph we can see that there is a rather wide angular range where we can set up to take EXAFS. Fig. 3(e) is a sketch which combines the contents in (b), (c) and (d) into a qualitative three dimensional view to illustrate their inter-relationships. The results shown in this example, although oversimplified (only one interface), represent the prototype of the behavior of the electric field in glancing-incidence cases. The result on a stratified system would be more complex, but the essence remains the same, i.e.

(i) in a glancing-incidence case when $\varphi < \varphi_c$ the field is confined mainly in a layer of 20 ~ 30 Å near the sample surface;

(ii) this thickness is approximately independent of the x-ray photon energy;

(iii) when $\varphi \rightarrow \varphi_c$ there is an intensity enhancement in the surface region which could be 2 to 3 times the incident intensity in vacuum.

Point (i) ensures that x-rays can be a surface probe in the glancing-incidence geometry. Points (i) and (iii) make the glancing-incidence technique ideal for surface x-ray diffraction studies. Point (ii), plus points (i) and (iii), make XAFS a suitable surface probe.

II.3) Glancing-incidence XAFS

In this section we discuss some of the methods of detecting the EXAFS signal under the glancing-incidence situation and the cautions that need to be applied in the interpretation of the relationship between the theoretical $\chi(k)$ and the experimentally measurable $\chi^{expt}(k)$.

The discussions in this section are associated with K-shell absorption for elements like Fe, Ni, Cu. Unless specifically mentioned, we imply that the x-ray photon energy is in the range of about 6.5 - 10 keV.

II.3.1) Glancing-incidence χ^{expt} vs theoretical χ

Fig. 4 is a schematic diagram to illustrate the notations to be used in the following text.

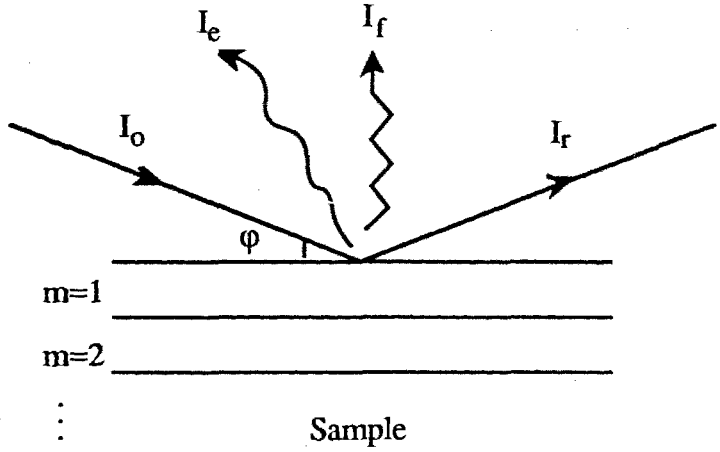

Fig. 4 An illustration of the notations to be used. I_o is the incident x-ray intensity, I_e the intensity of the total-electron-yield, I_f the intensity of the fluorescence x-ray yield and I_r the intensity of the specular reflection. m's indicate different elemental layers of the sample.

EXAFS is the oscillatory modulation in the absorption coefficient $\mu(E)$ and thus processes involving the absorption coefficient will have EXAFS in it. When an x-ray photon is absorbed by a K-shell event, the specular beam intensity I_r will be reduced by one photon, and there can be several final products of the absorption event coming out of the surface which include: i) fluorescence x-ray photons with intensity I_f which are mainly the $K\alpha_{1,2}$ photons [21]; ii) electrons (I_e) which include Auger electrons, photoelectrons and secondary electrons due to the cascades of inelastic scatterings of the first two kinds; iii) ions from electron stimulated desorption [22]; iv) 0 - 30 eV photons from inelastic scattering events of the primary electrons and fluorescent photons with valence electrons. [23] EXAFS has been observed in all these in all these processes. The detection mechanisms which have been successfully applied in glancing-incidence situation are mainly three: fluorescence, total-electron-yield and reflectivity.

II.3.1.1) Fluorescence

A typical fluorescence spectrum for an MBE grown film is shown in Fig. 5 for the convenience of the following discussion.

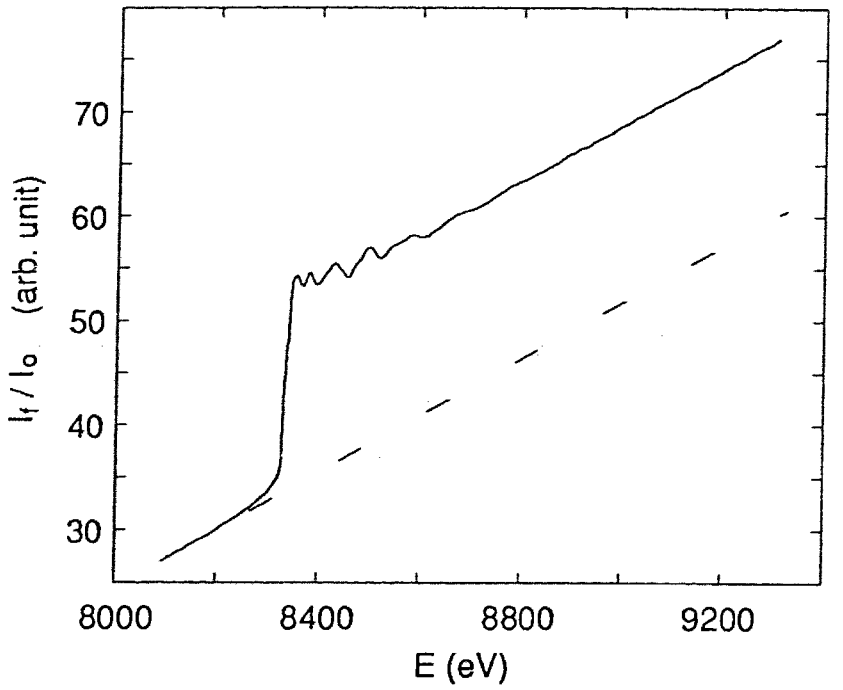

Fig. 5 Fluorescence yield spectrum for a 37 ML Ni overlayer grown on Fe(001) substrate. The pre-edge background is fitted by a straight line which is extrapolated into the post-edge region.

For a stratified sample the fluorescence yield signal measured as a function of the incident x-ray photon energy (with wave length λ) and the glancing-incident angle φ can be expressed as [24]

$$I_f(\lambda, \varphi) \propto \int_0^{\infty} \sum_j \eta_j(z)\, \mu_{\rho,j}(z)\rho(z)\, |\, E_{total}(\lambda, \varphi, z)\, |^2\, dz\,. \qquad \text{(II-26)}$$

The total electrical field amplitude E_{total} is given in (II-25); μ_ρ and ρ are the mass absorption coefficient and mass density respectively; η is the fluorescent yield which is the probability that a core-hole results in a fluorescence event. The fluorescent yield increases with the atomic number with $\eta \approx 0.5$ for $Z \sim 30$ (K-shell vacancies).[24] The summation in (II-26) is over different absorption edges. In equation (II-26) we have neglected the

attenuation of I_f along its escape path from the sample. In the systems of interest, the outgoing path (several tens of Å at most) is far less than the absorption length (a few micrometers) of the K_a fluorescence photons of Cu, Ni and Fe.

For the layered samples, (II-26) can be written as

$$I_f(\lambda, \varphi) = \tau I_o(\mu_{m,K}F_{m,K} + Background), \qquad \text{(II-27)}$$

where m designates the m^{th} layer; I_o is the incident intensity measured by the I_o detector; τ is the ratio of the response functions of detectors for I_o and I_f; $\mu_{i,j} = \rho_i\mu_{\rho,i,j}$ is the j^{th} edge linear absorption coefficient of the i^{th} layer at the incident photon energy, in particular $\mu_{m,K}$ is the K-edge linear absorption coefficient of the sample layer; and

$$Background = \sum_{i\neq m}\sum_{j}\mu_{ij}F_{ij} + \sum_{non\text{-}K}\mu_{m,non\text{-}K}F_{m,K}, \qquad \text{(II-27b)}$$

which includes the contribution of layers other than the sample and the contribution of other absorption edges of the sample layer (e.g. L, M). The remaining term

$$F_{ij} = \frac{\Omega}{4\pi}\eta_{ij}\int_{d_{i-1}}^{d_i} |\, E_{i,total}(\lambda, \varphi, z)\,|^2 / I_o\, dz \qquad \text{(for all } i\text{)}, \qquad \text{(II-28)}$$

with Ω being the solid angle subtended by the I_f detector.

We are interested in the energy spectrum above the K absorption edge. In this energy range the behavior of the *Background* term in (II-27) is not readily available because it is mixed up with the K-edge jump and the fine structures on it. However, if we assume the *Background* in (II-27) is a monotonic function of energy, then the extrapolation of *Background* below the edge can be used for the post-edge region. Because the absorption coefficients in *Background* do not have any structure in the energy range under the current discussion, this assumption means that we are ignoring any possible structure in the F's in

Background. The assumption is actually valid only in the energy range away from the edge and for an x-ray incident angle away from the effective critical angle of the system. We will come back to this point in section II.3.2.2 when we discuss the distortions in the near edge structure.

With the background removed and signal normalized by the incoming intensity we have the absorption coefficient measured from the glancing-incidence experiments

$$\mu_K^{expt}(E) = \frac{I_f(E)}{I_o(E)} - Background(E)\,, \qquad \text{(II-29)}$$

where we have dropped the layer designation m for clarity and used E to denote the incoming x-ray photon energy.* An illustration of the quantity $\mu_K^{expt}(E)$ is shown in Fig. 6. Because the energy of the fluorescent photon is fixed, the only energy dependence of τ is that of the I_o detector. When a partially transmitting ion chamber is used, as was the case in this thesis, this effect is relatively small (5 - 15%) and can be removed using tabulated absorption coefficients.[25] Now from (II-27) and (II-29) we have

$$\mu_K^{expt}(E) = \mu_K(E) F_K(E)\,. \qquad \text{(II-30)}$$

* Note: as far as EXAFS is concerned the background removal in (II-29) is largely cosmetic because later isolation of the EXAFS oscillations involves another, more important, background subtraction; however, writing the data in this form is conceptually helpful when later we discuss the source of distortions in the x-ray absorption near edge structure (XANES).

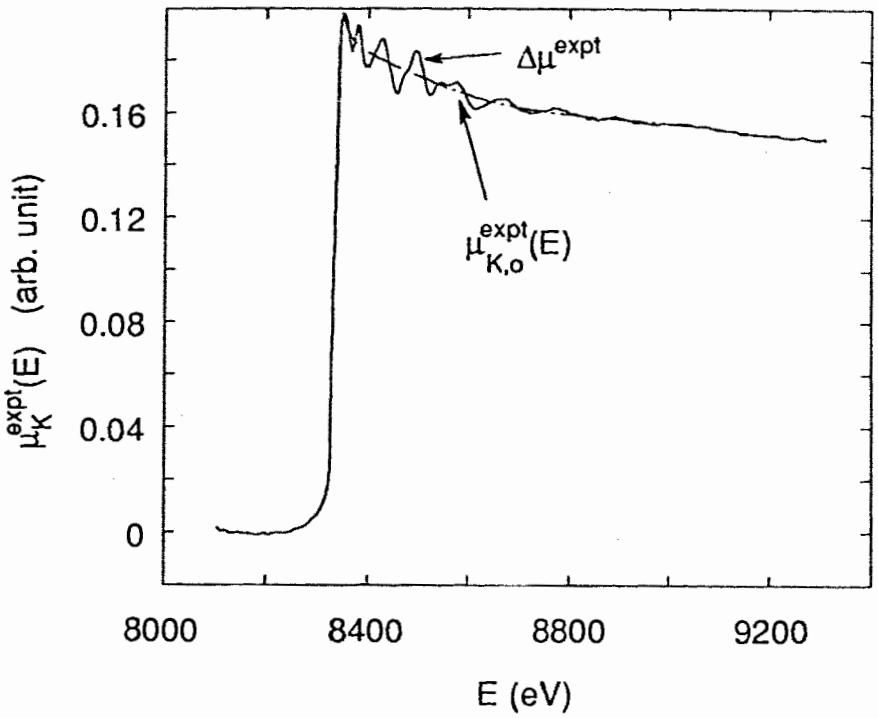

Fig. 6 $\mu_K^{expt}(E)$ of a 37 ML Ni overlayer on Fe(001).

To isolate the fine structure in the spectrum we decouple each term in (II-30) into two parts: a smooth monotonic background which reflects the atomic feature and the oscillatory portion due to the coordination structure in a crystal. On the right, $\mu_K = \mu_{Ko} + \Delta\mu$ and $F_K = F_{Ko} + \Delta F$, where the subscript "o" and the triangle "Δ" stand for the smooth and oscillatory parts respectively. The reason that F also has a oscillatory part can be seen from equations (II-28), (II-25) and (II-10): F is ultimately a function of the optical parameters δ and β of the sample layer, where β is related to μ by the relation $\beta = \mu\lambda / 4\pi$, [26] and δ is related to β through Kramers-Kronig relations. [27] On the left of equation II-30, $\mu_K^{expt} = \mu_{Ko}^{expt} + \Delta\mu^{expt}$, where the μ_{Ko}^{expt} is obtained by fitting the smooth background in the experimental μ_K^{expt} (see Fig. 6). The oscillatory part is no more than about 10% of the total signal, so after normaling to the edge jump height and neglecting the higher order terms in Δ we have

$$\chi^{expt}(E) \equiv \frac{\Delta\mu^{expt}(E)}{\mu_{Ko}^{expt}(E_o)} = \frac{F_{Ko}(E)\Delta\mu(E) + \mu_{Ko}(E)\Delta F(E)}{\mu_{Ko}(E_o)F_{Ko}(E_o)}$$

$$= \frac{\mu_{Ko}(E)F_{Ko}(E)}{\mu_{Ko}(E_o)F_{Ko}(E_o)}\left\{\chi(E) + \frac{\Delta F(E)}{F_o(E)}\right\} \qquad \text{(II-31)}$$

where E_o is the edge energy and the theoretical XAFS function $\chi(E)$ is as defined before in equations (II-2) and (II-3). The value of $\mu_{Ko}^{expt}(E_o)$ is obtained by linearly extrapolating the smooth background of $\mu^{expt}(E)$ (away from the edge region) to the first inflection point. This normally reduces the error in the edge jump estimation due to the peak in $F_{Ko}(E)$ around the edge due to the anomalous dispersion (see II.3.2.2). An analogous procedure could be followed in determining the theoretical edge jump $\mu_{Ko}(E_o)F_{Ko}(E_o)$ in the theoretical simulation. This will then make the theoretical edge jump estimation largely independent of the detailed structure in the vicinity of the first inflection point.

From (II-31) we see that the function χ^{expt} deviates from the theoretical χ in two parts: one is the energy dependent scaling factor outside the curly brackets and the other is the oscillatory term inside the curly brackets. We first take a look at the scaling term and then discuss the oscillatory one.

The factor $\mu_{Ko}(E)/\mu_{Ko}(E_o)$ is a smooth monotonic function of energy which appears also in the experimental data obtained by using standard techniques such as transmission. If a reference compound is to be used to compare with the sample then the factor can be left in the data and its effect will be canceled out in the comparison. If the data of the sample are to be fitted by theoretical parameters, the energy dependence of factor $\mu_{Ko}(E)/\mu_{Ko}(E_o)$ can be divided out by an appropriately tabulated atomic absorption coefficient as a function of energy.[28]

Our model calculations show that the other factor $F_{Ko}(E)/F_{Ko}(E_o)$ in the scaling term in (II-31) is a smooth function of energy in the EXAFS range but it is not always a monotonic function. Its energy dependence is dominantly determined by the x-ray incident

angle φ. When the incident angle is below the critical angle the factor can be described by a linear function to a very good approximation and the slope is positive. The lower is the incident angle, the smaller is the slope of $F_{Ko}(E)/F_{Ko}(E_o)$. The effect of $F_{Ko}(E)/F_{Ko}(E_o)$ seems weakly dependent on the sample layer thickness, for thicker layers the effect is larger. For a 50 Å Cu layer in Au(10ML)/Cu/Ag, at an incident angle about $\frac{2}{3}\varphi_c$ and 748 eV (~14 $Å^{-1}$ which is about the end of a typical data set and where the effect is the worst) above the Cu K edge, the factor $F_{Ko}(E)/F_{Ko}(E_o)$ magnifies $\chi(E)$ by about 13%. If the data is not corrected with the effect of the factor $F_{Ko}(E)/F_{Ko}(E_o)$, the resulting EXAFS Debye-Waller factors would appear to be smaller than the real values, but the determination of bond lengths and the ratio of coordination numbers should remain unaffected. When information such as the density and thickness of each layer can be reliably obtained by other independent measurements, e.g. accurate reflectivity vs angle curves, the function $F_0(E)$ can be calculated using (II-28) and can be divided out of the experimental interference function χ^{expt}.[29] For the sample studied in this work it is difficult to rely on the reflectivity measurements to deduce the sample layer thickness and the density because firstly, the quality of the metal substrate is not flat enough to have high quality reflectivity data and secondly the sample layers involved are too thin to have distinct features to be fitted by a simple model.

As pointed out by Heald, Chen and Tranquada, the oscillatory term, $\frac{\Delta F(E)}{F_o(E)}$, in the curly brackets in (II-31) produces a more direct distortion on the EXAFS interference function χ.[29] Notice that $F = F(\delta, \beta, \varphi)$ and $\delta = \delta_o(E) + \Delta\delta(E)$ and $\beta = \beta_o(E) + \Delta\beta(E)$, where again they are separated into smooth background and oscillatory part. The oscillations ΔF can be expanded in terms of $\Delta\delta$ and $\Delta\beta$,

$$\Delta F = \left.\frac{\partial F}{\partial \beta}\right|_{\delta_o\beta_o} \Delta\beta + \left.\frac{\partial F}{\partial \delta}\right|_{\delta_o\beta_o} \Delta\delta \qquad \text{(II-32)}$$

where
$$\Delta\beta = \frac{\lambda}{4\pi}\Delta\mu = \frac{\lambda}{4\pi}\mu_o(E)\chi(E) = \beta_o(E)\chi(E)$$
$$= \beta_o(E)\, Im \sum_j A_j \exp i\,[\,2kR_j + \phi_j\,], \qquad \text{(II-33)}$$

In the last step *Im* takes the imaginary part of what follows and A is the shorthand for the effective amplitude of χ in equation (II-3). $\Delta\delta$ is related to $\Delta\beta$ through Kramers-Kronig relations,[27] so without loosing generality we can write

$$\Delta\delta = \gamma\beta_o(E)\, Im \sum_j A_j \exp i\,[\,2kR_j + \phi_j + \psi\,] \qquad \text{(II-34)}$$

where γ is the amplitude ratio of $\Delta\delta$ and $\Delta\beta$, and ψ is the difference of the phase between them. It has been shown that $\gamma \approx 1$ and $\psi \approx 3\pi/2$. [29, 30]

Substituting (II-33) and (II-34) into (II-32) gives

$$\chi^{expt} = \frac{\mu_o(E)F_o(E)}{\mu_o(E_o)F_o(E_o)}\, Im\left\{\chi(k)\left[\,1 + \frac{\beta_o}{F_o}\frac{\partial F}{\partial\beta}\bigg|_{\delta_o\beta_o} + \frac{\beta_o}{F_o}\frac{\partial F}{\partial\delta}\bigg|_{\delta_o\beta_o}\gamma e^{i\psi}\,\right]\right\}, \qquad \text{(II-35)}$$

where the K edge designation is dropped for clarity, $k = [\,2m_e(\hbar\omega - E_o)\,]^{1/2}/\hbar$, and $\chi(k)$ is in its complex form, i.e. $\chi(k) = \sum_j A_j exp\, i\,[\,2kR_j + \phi_j\,]$. The correction factor in the square bracket can be broken up into its amplitude (*Amp*) and phase (*Phase*) components: [29]

$$Amp = [\,C_\beta^2 + C_\delta^2 + 2C_\beta C_\delta cos(\psi)\,]^{1/2},$$
$$Phase = tan^{-1}\left\{C_\delta sin(\psi) / [\,C_\beta + C_\delta cos(\psi)\,]\right\}, \qquad \text{(II-36)}$$

where
$$C_\beta = 1 + \frac{\beta_o}{F_o}\frac{\partial F}{\partial\beta}\bigg|_{\delta_o\beta_o}, \qquad C_\delta = \frac{\beta_o}{F_o}\frac{\partial F}{\partial\beta}\bigg|_{\delta_o\beta_o}\gamma\ . \qquad \text{(II-37)}$$

These corrections can be applied to the amplitude A and phase ϕ in $\chi(k)$. Note for unknown structures these corrections can not be accurately evaluated unless information such as the layer thicknesses and densities can be determined by some independent experiments, e.g. quantitatively accurate reflectivity and fluorescence yield measurements as functions of incident angles at some selected energies. In section II.3.2 we will use these equations to estimate the effects of the amplitude and phase corrections needed for the data obtained in glancing-incidence for various systems.

II.3.1.2) Total-electron-yield (TEY)

A typical total-electron-yield spectrum for a MBE grown film is shown in Fig. 7.

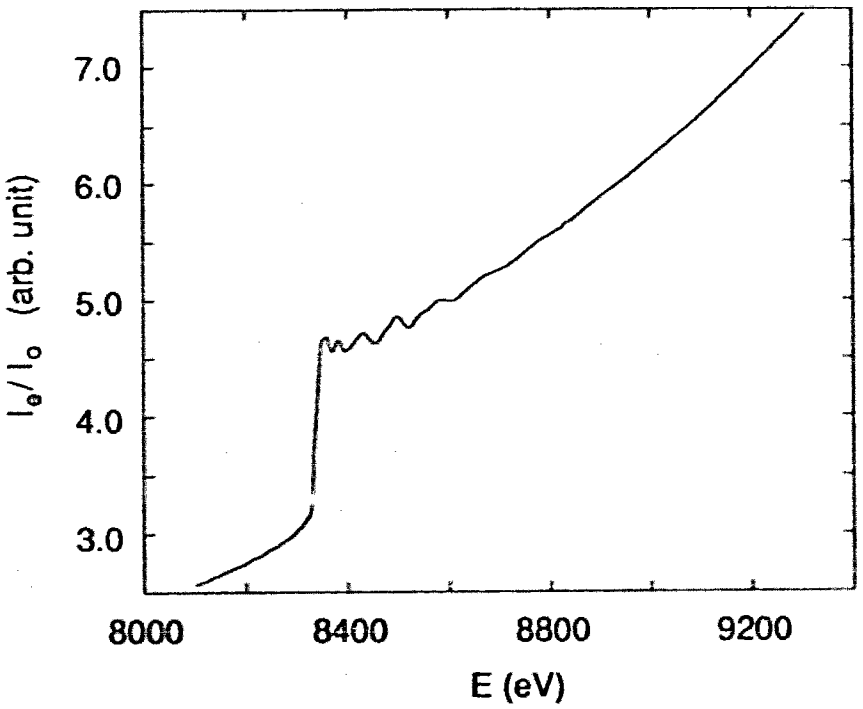

Fig. 7 A typical total-electron-yield spectrum for Ni film grown on Fe(001) by MBE.

For atoms with an atomic number around 30, there is about a 50% chance that a K-shell vacancy is filled through an Auger process. Very much like the case of fluorescence,

the intensity of Auger electron yield is also directly proportional to the absorption coefficient. So if only the Auger electrons (e.g. KLL) are detected, the formulas in II.3.1.1 should remain valid for I_e of the Auger process as well, except the fluorescence yield η should be replaced by the Auger yield coefficient. As a matter of fact, because the inelastic mean free path of the Auger electrons is limited to only several ten Å (e.g. 35 Å for KLL Ni-in-Ni.), [31] the Auger electron detection is intrinsically surface selective no matter what the incident angle is. Auger electrons have been used in surface studies in a UHV environment. [22] The requirement of UHV environment limits the range of the applicability of this detection mode and systems like liquid surfaces and buried interfaces are not accessible.

If, however, all the outcoming electrons are detected as I_e, it has been shown that like in the Auger or fluorescence case, I_e/I_o also gives fine structure analogous to XAFS obtained by transmission. The early studies suggested that although the frequencies of the total-electron-yield (TEY) fine structure are identical to that from the transmission the amplitudes in TEY XAFS show some reductions (–15 to –30%).[32] But later studies have shown much smaller amplitude deviations, about ±5%, from the transmission XAFS.[33, 34] Although there have been many successes in applying TEY XAFS in various situations, there are still some details of the TEY process that have not been quantitatively resolved yet, e.g. the problem of relative contribution of photoelectrons.[33, 35]

All the systematic studies on TEY mentioned above are for large x-ray incident angle cases. Previous to this work the applications of TEY had not been directly checked against a standard method such as the fluorescence yield or the Auger electron yield under the same conditions in a glancing-incidence situation. Considering that the only difference between the glancing-incidence situation and a large angle of incidence is that the distribution of electric field inside the sample is now a non-monotonic function of photon energy and incident angle, which has been accounted for in the integral in equation (II-28), it is then

not unreasonable to expect that in the glancing-incidence case I_e/I_o also produces XAFS just like the way fluorescence does. The formulae in section II.3.1.1 should also hold if I_f is replaced by I_e and the yield efficiency η is understood as that of the secondary electrons. As we shall see in Chapter III this assumption is supported by experimental results. Because the TEY signal is dominated by the secondary electrons which are produced by inelastically scattered Auger electrons, [32] an UHV condition is not necessary for the detection of these secondary electrons. This makes TEY detection rather simple and powerful (see also Chapter III).

II.3.1.2) Reflectivity

A typical reflectivity spectrum of a Ni film grown on a Fe substrate is shown in Fig. 8.

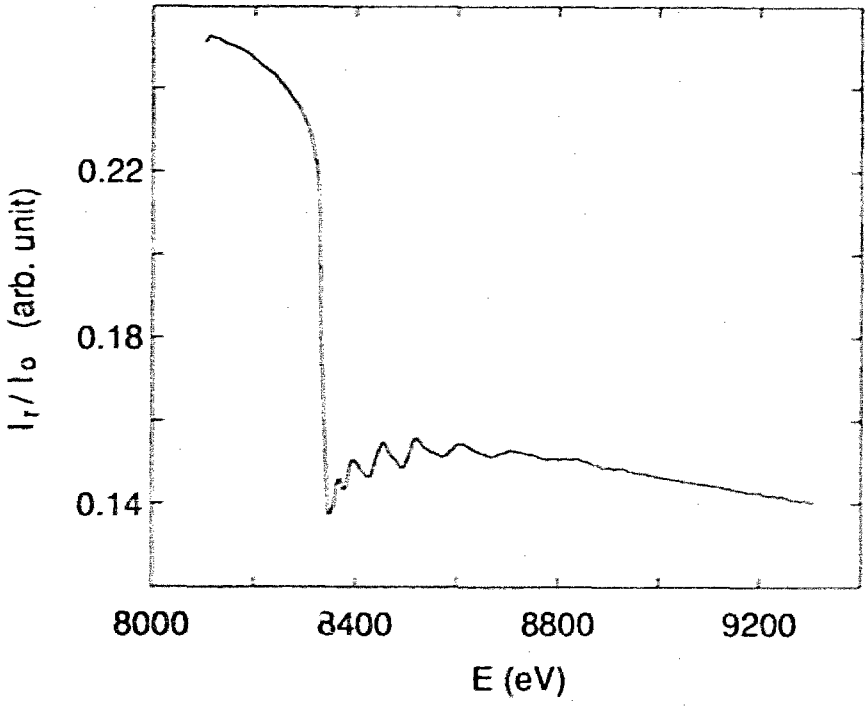

Fig. 8 A typical reflectivity spectrum for a Ni film grown on Fe(001) by MBE.

The first systematic measurement and analysis of reflectivity EXAFS spectra were carried out by Martens and Rabe[30, 36-38] for the K edge of copper films (several hundred Å thick) evaporated on glass substrates. As pointed out by these authors, in general the imaginary part of the refraction index, $\beta(E)$, can be calculated from the reflectivity $|R_{1,2}(E, \varphi)|^2$ which has been measured in the complete angular-energy space, but the number of points that have to be measured (10^6 points with a signal-to-noise ratio $\geq 10^3$) [30] makes this general approach unacceptably time-consuming. They therefore applied an approximate approach to isolate, β^{expt}[30, 37] from the reflectivity measured as a function of x-ray energy and incident angle. However, even with the approximate method one would have to have information such as density and thickness of each layer in the sample and above all, quantitatively accurate reflectivity data from which the raw absorption data β^{expt} can be retrieved. In the ultrathin samples we studied quantities like the densities and thicknesses are not easily obtainable. In addition to these difficulties, the flatness of the crystal metal substrate appears far less ideal than that of float glass, and unlike the basically one interface problem studied by Martens and Rabe, we have a system of at least three interfaces for air, cover layer, sample layer and substrate. These factors further prevent us from hoping to reliably extract the β^{expt} by fitting the detail of the reflectivity curves with the simple model described in II.2.2. So we had to use some methods other than that of Martens and Rabe.

A simple qualitative argument seems to lead to satisfactory results for extracting $\chi(E)$ from the reflectivity as a function of x-ray energy. By energy conservation, the sum of scattered intensity and absorbed intensity should be equal to the incident intensity. When $\varphi \leq \varphi_c$ if we approximate the scattered intensity by the specular beam I_r, because the coherent scattering is dominant in such cases,[39] then we have

$$I_r + I_{absorb} = I_o , \qquad \text{(II-38)}$$

where I_{absorb} is proportional to the absorption coefficient μ. Therefore

$$1 - I_r/I_o \propto \mu . \qquad \text{(II-39)}$$

So approximately the quantity $(1 - I_r/I_o)$ can be treated just like I_f/I_o or I_e/I_o to extract the $\chi(k)$. Although this method of extracting XAFS from reflectivity has been practised by quite a few research groups [40-42], there has been a lack of systematic studies to evaluate the extent of its validity. Nevertheless in the next chapter we will see that in practice the EXAFS data extracted using (II-39) have the same frequency content as the data obtained from the other two methods, but the amplitude obtained is more uncertain than that of the other two methods.

The anomalous dispersion effects are also included in I_r/I_o. This can be seen from the relation $I_r/I_o = |R_{12}|^2$ where the latter is a function of δ and β of the system. In a favorable sample case (large,flat and thicker samples) it was claimed that the effects of anomalous dispersion in the reflectivity EXAFS data could also be corrected in a similar way as that for the fluorescence.[43]

II.3.2) Anomalous Scattering Effect

From the discussion of the previous section we see that the XANES and EXAFS spectra obtained in glancing incidence mode are not exactly the same as those obtained in a conventional mode, e.g. the transmission. In this section we examine how large the deviations are and the situations in which they are minimized. We first deal with EXAFS and then XANES.

II.3.2.1) Distortion in glancing-incidence EXAFS

The amplitude and phase corrections for the interference function $\chi(k)$ are given by equation (II-36). To calculate them we need to use the equations (II-37) and (II-28). This means we must calculate the electrical field everywhere in the sample using the equation

(II-25). When the optical parameters are available for each layer of the sample these corrections can be calculated and therefore the corrected $\chi(k)$ can be obtained from χ^{expt}. Fig. 9 and Fig. 10 shows the calculated results of *Amp* and *Phase* at at the Cu K-edge for (a) Au(10ML)/Cu(8ML)/Ag, (b) Au(10ML)/Cu(50Å)/Ag, and (c) Au(10ML)/Cu(400Å)/Ag. The first two sample layer thicknesses in (a) and (b) (8 ML and 50 Å) are the typical ones studied in this work. Case (c) is chosen to compare our results with similar results in the literature. In the calculation the bulk crystal densities were used. For the 8 ML Cu case replacing the bulk fcc Cu density (8.96 g/cm^3) with the more realistic "bct Cu" (to be discussed in Chapter VI) density 8.21 g/cm^3 would change the *Amp* and *Phase* shown in Fig. 9(a) by only a negligible amount (less than 0.4% in *Amp* and 0.44% rad in *Phase* respectively).

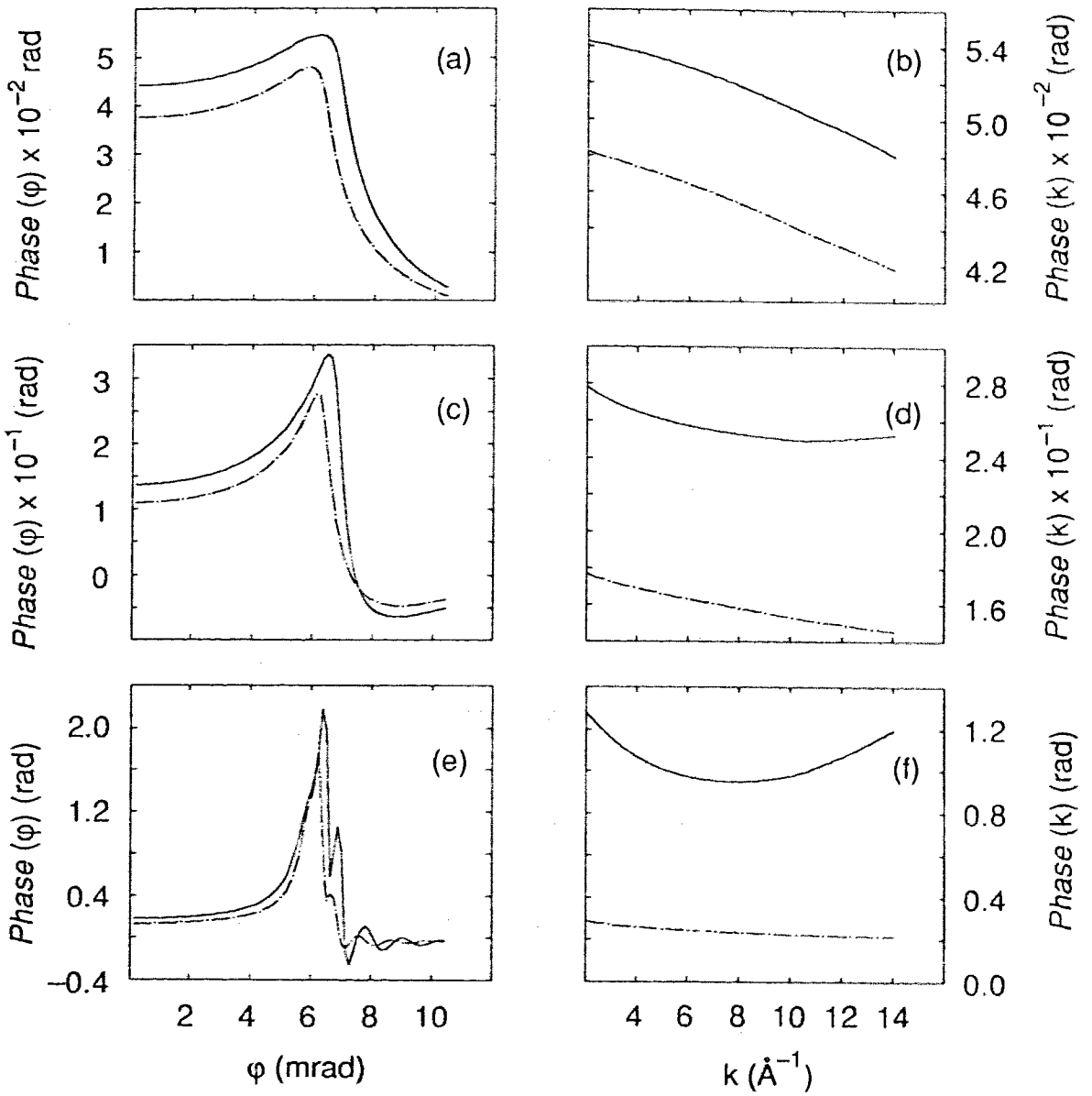

Fig. 9 The phase correction term as a function of the incident angle (left column) and of the x-ray energy (right column). The three rows correspond to the layer thickness 8ML, 50Å and 400Å respectively. In each graph in the left column the solid and dash-dot lines correspond to the wavenumbers 2 Å^{-1} and 14 Å^{-1} respectively; in the right column the solid and dash-dot correspond to the incident angles φ_c and $\frac{2}{3}\varphi_c$ respectively. (The φ_c is that of Cu.)

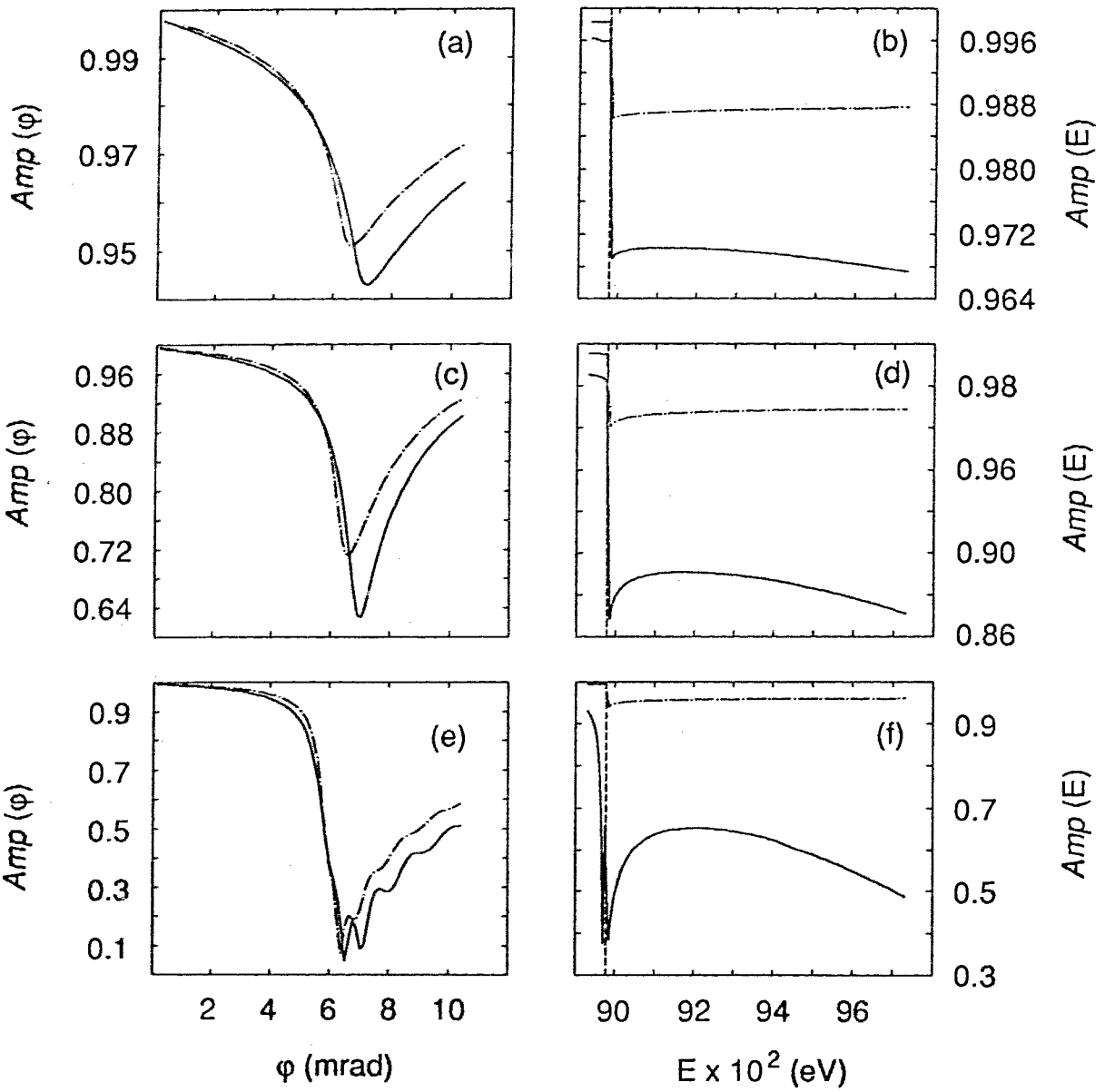

Fig. 10 The amplitude corrections are plotted as functions of incident angle and x-ray energy. The notations used are the same as those in Fig.9.

First we examine the anomalous dispersion effects in the phase of the EXAFS interference function which decides how accurate the bond length determination can be. The left column of Fig. 9 shows the term *Phase* as a function of the incident angle for the Cu layer thicknesses. In this column the two curves in each graph correspond to the starting and ending wavenumbers of a typical glancing-incidence EXAFS spectrum, the curves for other wavenumbers would fall in between these two if plotted. The biggest phase change occurs around the critical angle of Cu in this energy range, i.e. about 6 mrad, and the absolute phase shift increases as the Cu layer thickness increases (notice the different vertical scales). On the right side of Fig. 9 the term *Phase* as a function of photo-electron wavenumber is plotted. In these three graphs the two curves correspond to two typical incident angles, namely, near φ_c and below φ_c. In a glancing-incidence EXAFS interference function $\chi(k)$ the total phase is $(2kR + \phi + Phase)$, so if we approximate the term *Phase* by a straight line $a + bk$ then the error in determining the distance R caused by term *Phase* is of the order of $\Delta R = \frac{b}{2}$. The results of the estimated ΔR are listed in Table 1.

	ΔR (Å)	
Thickness	$\frac{2}{3}\varphi_c$	φ_c
8 ML	–0.0003	–0.0003
50 Å	–0.001	–0.002
400 Å	–0.001	+0.02 –0.03

Table I. The ΔR values are one half of the slopes of the straight lines which are least-squares fitted to the curves in (b), (d) and (f) of Fig. 9. In the case of the 400 Å Cu layer at φ_c the two ΔR values are estimated from the low k and high k part of the curve respectively.

If we consider that the accuracy of standard EXAFS techniques in bond length determination is typically 0.01 Å to 0.02 Å,[35] we see from Table I that as far as the distance determination is concerned the anomalous dispersion effect is negligibly small. However, caution is needed in dealing with the worst case, a thick (several hundred Å) sample layer at the critical angle. In the case shown in Fig. 9(f) the nonlinearity in the *Phase* vs *k* curve may cause difficulties in distinguishing the contribution to the phase of two beating shells from the anomalous dispersion effect. To avoid this sort of problem it is better to have some data at lower incident angles, e.g. $\frac{2}{3}\varphi_c$ in this particular case. In all the samples studied in this thesis the maximum sample layer thickness is around 50 Å, so the distortion in the bond length determination due to the anomalous dispersion is neglected.

Similar calculations of *Amp* and *Phase* as discussed above have also been carried out for the Al/Ni/Fe system (with Ni being the sample layer), the results are similar to that of Au/Cu/Ag and the estimation in Table 1 also holds for the Ni case.

In Fig. 10 the amplitude correction factor *Amp* is plotted as a function of the incident angle (left column) or as a function of the x-ray energy (right column) for the same three Cu layer thicknesses as in Fig. 9. Again, the two curves in the left column graphs correspond to the starting and ending wavenumbers of a typical glancing-incidence EXAFS spectrum, and the two curves in the right column graphs are for the incident angles φ_c and $\frac{2}{3}\varphi_c$. As shown in Fig. 10(a), when the sample layer is only a few monolayers thick, the amplitude correction is of the order of 5% in the worst case. This is within the uncertainty range of optimized EXAFS measurements, i.e. about 10%[35] and therefore no corrections for the original data are necessary in such cases. On the other hand when the sample layer thickness is large, the amplitude correction can be enormous as the φ_c is approached as shown in Fig. 10(c) and (e). As shown in the right column of Fig. 10, in most cases the amplitude corrections are nearly constant in the energy spectrum with the exception of a thick sample (several hundred Å) at the critical angle (see Fig. 10(f)). This

simplifies the factor *Amp* to a single parameter when the amplitude corrections are needed. Also because of this uniformity in energy space above the Cu K-edge the $\chi(k)$ of all the shells are equally affected, so the relative strength between the shells are undistorted by the anomalous dispersion.

To compare the amplitude corrections discussed above to experimental data, we did calculations for the case of a several hundred Å thick Au film evaporated on a float glass substrate. In Fig. 11 the factor *Amp* as a function of the incident angle is plotted for two different Au thicknesses. The experimental data taken from Ref. 29 are shown with the error bars. The x-ray photon energy used for the theoretical curves is 12065 eV which corresponds to a wavenumber 6.2 $Å^{-1}$, i.e. roughly in the middle of the experimental spectra in the k space. The calculated curve is not sensitive to the x-ray energy. In making the figure the angular zero of the experimental data have been shifted by 0.6 mrad which is presumably due to either an experimental calibration error or an inaccuracy in the optical parameters used in the calculation. The overall qualitative agreement between the experimental data and the theoretical predictions are satisfactory, considered the calculation is idealized which ignores practical factors such as surface roughness. Around the critical angle region the amplitude correction seems to be overestimated by the theoretical results.

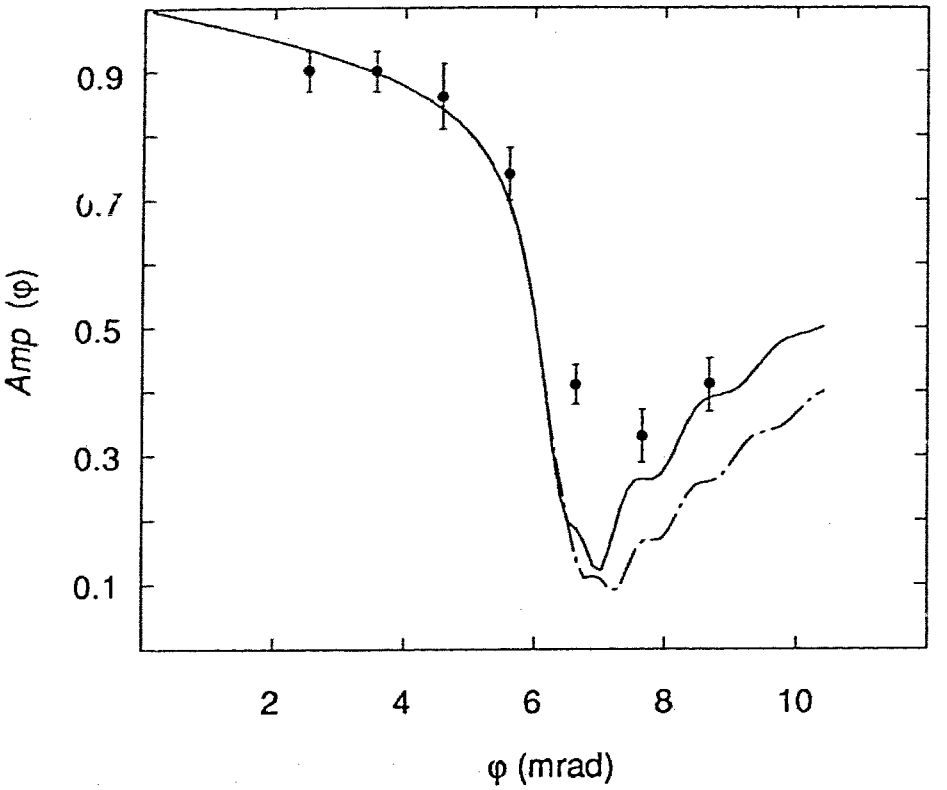

Fig. 11 Comparison of the calculated EXAFS amplitude correction with experimental data of a Au film evaporated on glass. The solid curve is for Au(300Å)/glass and the dash-dot curve is for Au(400Å)/glass. The filled circles are experimental data.

II.3.2.2) Distortion in glancing-incidence XANES

Being part of the fine structure, XANES also suffers from the same distortions discussed in the previous sections for EXAFS. In addition, since XANES is in the vicinity of the edge where the anomalous dispersion effect is the strongest there exists yet another kind of distortion which is the subject of this section.

In section II.3.1.1 when we extracted $\mu^{expt}(E)$ from the raw signal $I_f(E)$ we had assumed that the *Background* in (II-27) (actually the quantity F_{ij} given by formula (II-28)) was a monotonic function of energy. About 20 eV away from the sample absorption edge that certainly is the case, but in the vicinity of the absorption edge due to the anomalous

dispersion F_{ij} actually has a pronounced peak. This is shown by the theoretical calculation presented in Fig. 12 for the system Au(10ML)/Cu(8ML)/Ag. In this case the F_{ij} involve the M-edges for the Au and L-edges for the Ag.

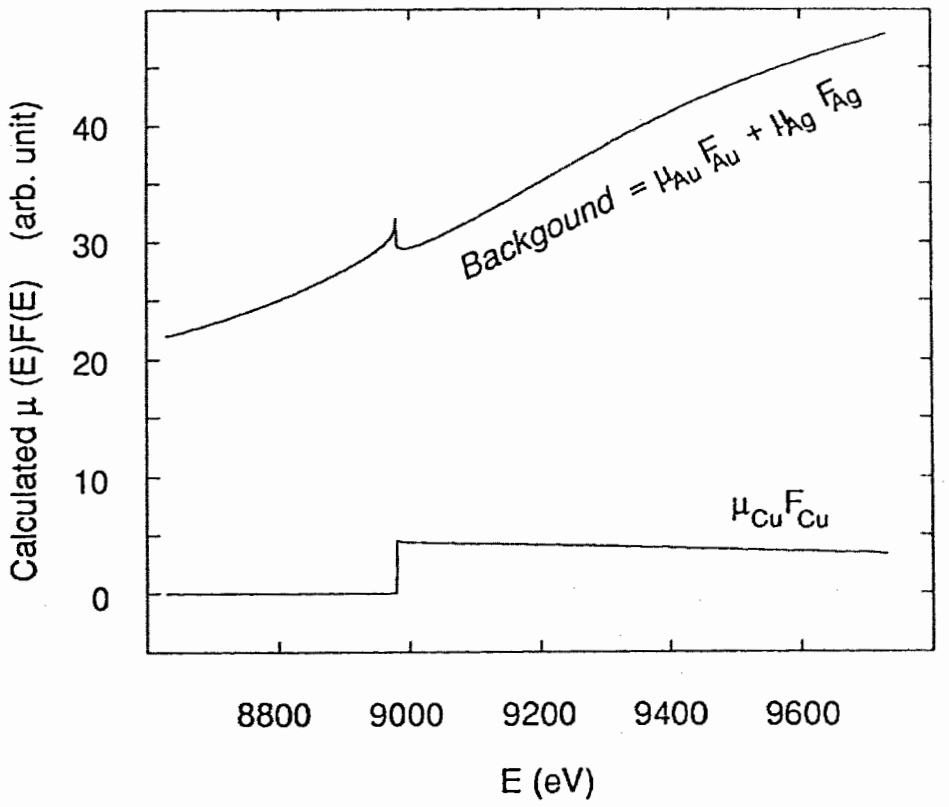

Fig. 12 Calculated $\mu_{Cu}F_{Cu}$, $Background = \mu_{Au}F_{Au} + \mu_{Ag}F_{Ag}$ for Au(10ML)/Cu(8ML)/Ag.

Although only the f' and f" of the sample layer have the resonance behavior in this energy region, due to the boundary condition confinement once the electric field distribution in the sample layer is suddenly changed because of the anomalous dispersion the field distribution in the cover layer and the substrate will also change reactively. Thus the resonance peak appears in all the three layers. As a matter of fact, because the total absorption of Au and Ag is comparable to, or larger than that of the Cu in the case under consideration, the contribution in the total yield signal is mainly from the cover layer and the substrate. Because this pronounced peak at the edge can not be removed by the usual

background removal procedure (e.g. by smoothing or polynomial fitting), if the entire yield signal were detected the XANES would be severely distorted as shown in the upper curve of Fig. 13. However, if only the Cu signal were detected, the distortion would be reduced by more than an order of magnitude as shown in the middle curve of Fig. 13. Comparing with the undistorted case shown in the lower curve the distortion remaining in the "filtered" data (the middle curve) is hardly noticeable. In the worst case ($\varphi \rightarrow \varphi_c$) it is less than 2% of the jump at 5 eV above the Cu K edge and is limited to a range of about 10 eV above the edge. This residual distortion leaves all the detailed near edge structure virtually unaffected.

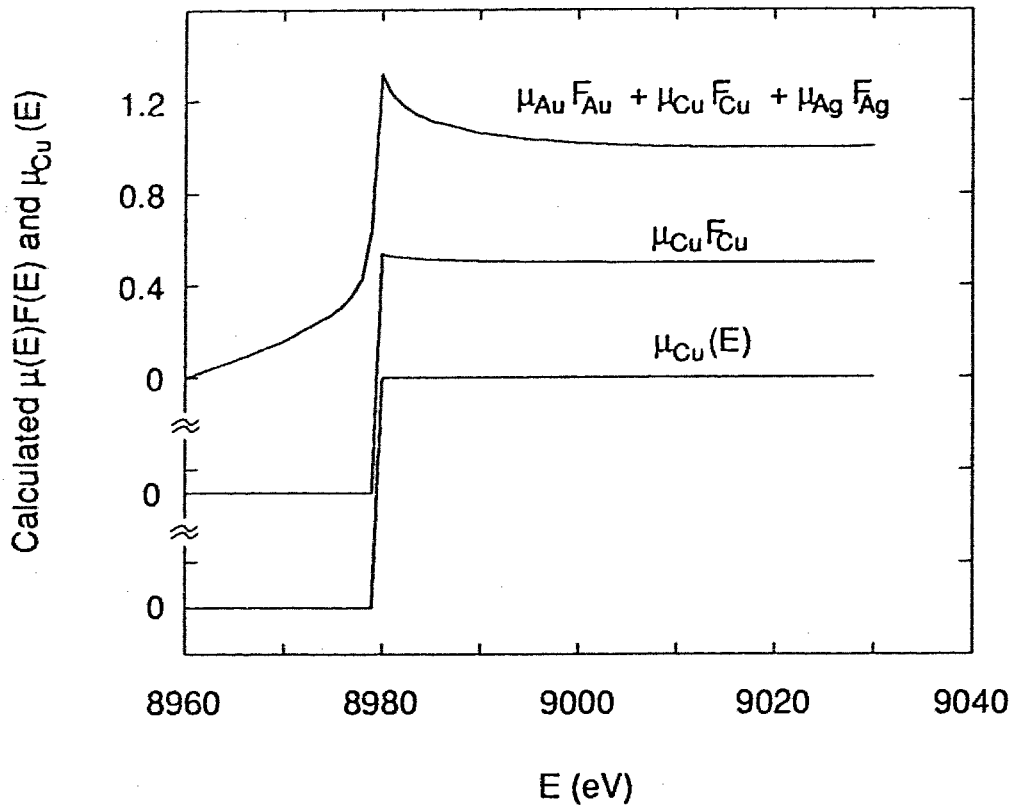

Fig. 13 Comparison of calculated $\mu_{Au}F_{Au} + \mu_{Cu}F_{Cu} + \mu_{Ag}F_{Ag}$ (upper curve) and $\mu_{Cu}F_{Cu}$ (middle curve) for Au(10ML)/Cu(8ML)/Ag. The lower curve is $\mu_{Cu,K}$ of Cu calculated from f'' which in turn is calculated using an *ab intio* formalism of Cromer and Liberman. The curves were normalized to the edge jump in each case and were displaced for clarity.

For fluorescence yield cases the signal selection can be achieved by appropriate filters or by a detector with ability of energy discrimination like a Ge solid state detector. For the system discussed here the fluorescence signal of Cu (Cu K_α) can be easily separated from the low energy fluorescent signal of Au (Au M_α and M_β) and Ag (Ag L_α and L_β) by putting a thin piece of plastic in the fluorescence photon path (see Chapter VI for detail). Notice that this method does not eliminate the distortion but simply relies on the fact that in the case of a thin sample layer the anomalous dispersion distortion by the sample itself is small. For a thick sample the distortion from the sample layer itself would be rather large and can only be corrected by a reliable calculation of the quantity *F* defined by equation (II-28), which has been claimed to be possible by Tourillon and coworkers. [44]

II.3.2.3) Discussion

The correction scheme outlined in II.3.2.1 and discussed in the previous two sections is based on a model of a 2 dimensional isotropic layer. For crystalline layers it may break down in some subtle ways due to the existence of many Bloch waves in the layer. There are also some limitations in applying the correction method quantitatively to the ultrathin crystalline films. For example, in order to calculate the correction terms *Amp* and *Phase*, information for each layer like the density, thickness and roughness are needed. Presumably one would need to study in detail the reflectivity or yield vs angle curves to obtain those optical parameters. For crystal metal substrates even when great care is taken in polishing the surface, the finished quality seems still not good enough to produce readily decipherable reflectivity or yield vs angle curves. This plus the fact that the small thickness of the sample layer makes the effect of the layer of interest insignificant relative to the substrate complicate the process of extracting reliable optical parameters of the sample system. Nevertheless, because the calculated results for the correction are not very sensitive to the optical parameters, they can provide a basic idea of how severe the distortions are in various cases.

From the results of the discussions in the previous two sections we can see that without applying any corrections the reliable structural information we can get from glancing-incidence EXAFS are the bond lengths and the relative amplitudes of different shells. For the thin films studied in this work (maximum sample layer thickness is around 50 Å) the distortion in the bond length determination can be neglected (see Table 1). In a favorable case such as the very thin sample layer like the Cu in Au/Cu(8ML)/Ag(001), even the amplitude correction is also negligible (the correction is less than 5% when $\varphi < \varphi_c$). The XANES from the total-electron-yield and reflectivity are severely distorted by the strong anomalous dispersion effect around the edge. However, if the signal from the sample layer can be separated easily from the others (i.e. the cover layer and the substrate), as is the case in the fluorescence detection, the distortion can be reduced to an acceptable level for thin sample layer cases.

Chapter III Experimental Aspects of Glancing-incidence XAFS

In this chapter we discuss some of the experimental aspects of glancing-incidence XAFS. The main focus is on the instruments and methods developed in this work. A detailed discussion on the technical matters concerned with XAFS experiments on a synchrotron radiation beam line can be found in Ref. 1.

A schematic view of a typical experimental set-up for glancing-incidence XAFS using hard x-rays is shown below in Fig. 1. When a charged particle is accelerated it produces radiation. In particular, when charged particles are accelerated in circular motion with a speed near the speed of light, the radiation emitted is usually termed as *Synchrotron* radiation. There are many useful properties associated with synchrotron radiation[2], primarily they include: i) high intensity; ii) broad spectral range; iii) natural collimation; iv) high polarization and v) pulsed time structure. The properties i)-iv) make synchrotron radiation an ideal light source for the glancing-incidence XAFS technique. As shown in Fig. 1, the white radiation from a synchrotron is first collimated by the entrance slit s_o, then a monochromatic beam is selected by a Bragg monochromator, and after that the x-ray enters the experimental area which is customarily confined in a metal house - the *hutch*. In what follows we will discuss the functions of the instruments in the hutch shown in Fig. 1.

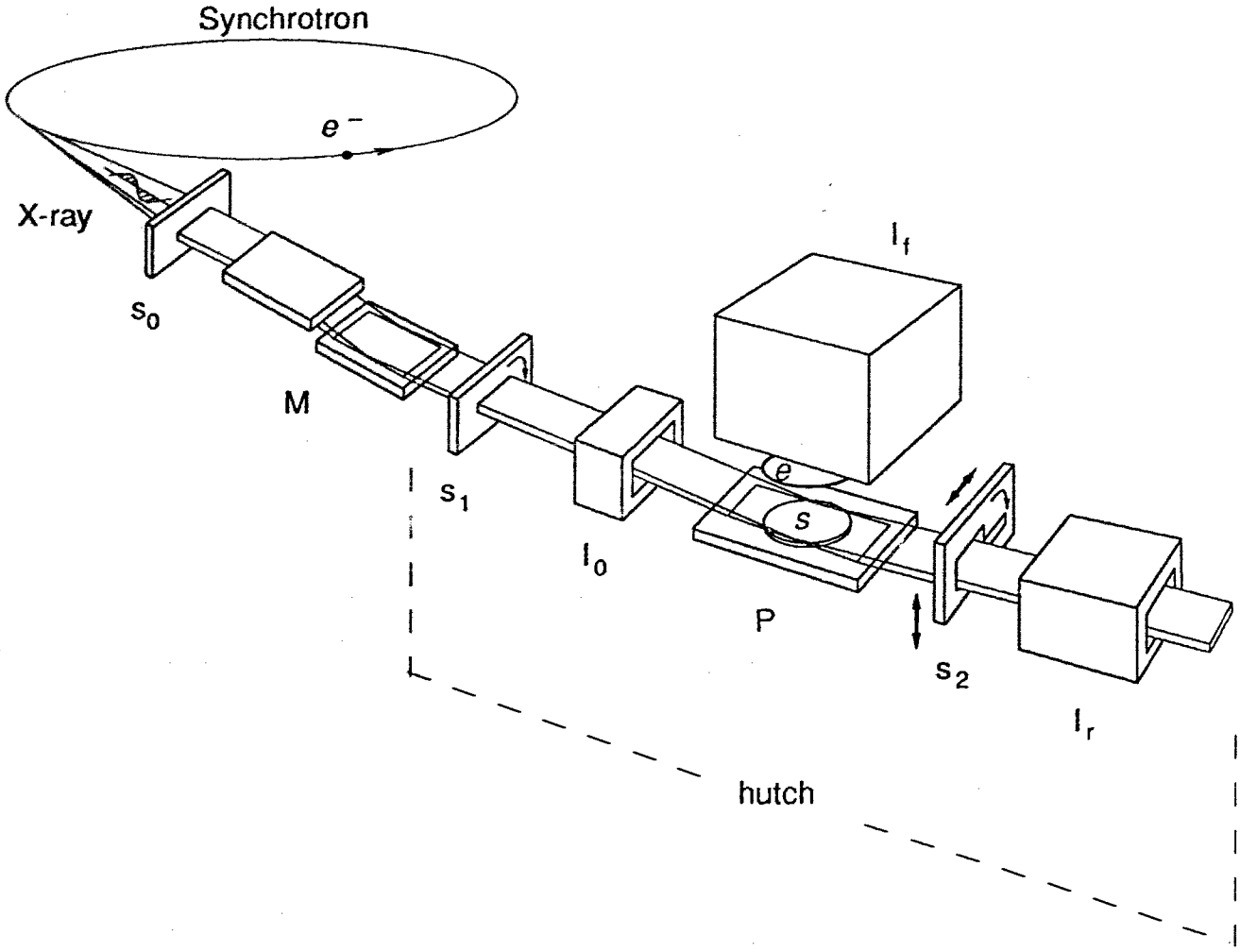

Fig. 1 Schematic view of a typical glancing-incidence XAFS experimental set-up. s_o is the entrance slit of the monochromator (*M*). The exit slit s_1 is a Huber slit mounted on a rotation stage, I_0 and I_r are two ionization chambers for detecting the intensity of the incoming beam and specularly reflected beam respectively. P stands for the sample positioner. On the positioner a rotation stage, *s*, is attatched and the sample is mounted on the stage. *e* and I_f stand for a total-electron-yield detector and a wide-aperture fluorescence detector respectively.

III.1) Sample Positioning

The main difference between handling x-ray optics on a synchrotron radiation beamline from handling usual optical techniques is the safety problem which prevents access to the hutch when the beam is on. To achieve both accuracy and efficiency it then is desirable to motorize every moving part by stepping motors or the equivalent and computerize the remote operation as much as possible.

III.1.1) The Sample Positioner

To apply the glancing-incidence technique, first of all an accurate and efficient angular adjustment apparatus is needed. In this work a versatile sample positioner was designed and constructed [3, 4] primarily for XAFS measurements with synchrotron radiation in the hard x-ray region.

The perspective view of the apparatus is shown in Fig. 2. The platform (*a*), an aluminum plate 30cm long x 10cm wide, can be raised at each end by a micrometer (b, 40 turns/inch), which in turn is driven by a stepping motor (d, 200 steps/turn) [5] through two transmission discs (c, diameter 3.5cm). The upper disc is attached to the micrometer and via 3 vertical poles slides relative to the lower one which is attached to the stepping motor. They are designed to transmit the driving force and minimize backlash. The electronics driving the stepping motors is controlled by a microcomputer (NEC PC 8201A) through its parallel printer port. A BASIC program in the microcomputer allows the apparatus to be adjusted manually using the cursor keys or under program control, interacting with the EXAFS data collection software [6] through its serial port. The platform can be tilted at a grazing angle φ relative to the incident beam in angular steps of 13.5 μrad. There are four springs (not shown in the figure) at each corner of the platform. The springs connect the platform to the positioner stand (g, end dimensions 3.8cm x 10cm x 23cm) and provide the

restoring force to keep the platform in contact with the two micrometer tips. One micrometer tip has a steel cone head which fits in a mating hollow cone in one end of the platform. In the other end of the platform, a hemi-spherical ball is mounted which contacts with the flat micrometer tip. The four rectangular bars (1.3cm x 0.64cm x 7cm) on the positioner stand prevent the platform plane from tipping in the direction perpendicular to the plane determined by the x-ray beam and the center longitudinal line of the positioner.

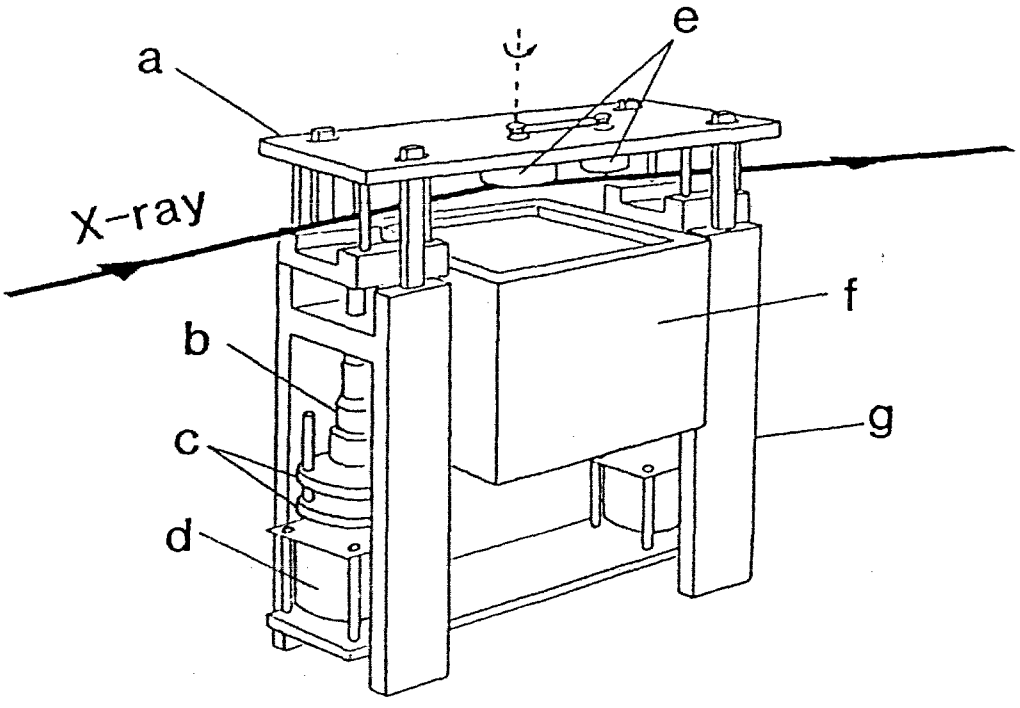

Fig. 2. The perspective view of the apparatus: *a.* platform, *b.* micrometer, *c.* transmission discs, *d.* stepping motor, *e.* rotation stage and its driving motor, *f.* ion chamber for fluorescent x-rays, *g.* the stand.

The apparatus is designed to operate in air in the hutch on a synchrotron radiation beamline, and it can be turned through 90° so that the electric vector of the x-ray beam from the monochromator can be perpendicular or parallel to the solid sample surface. The overall dimensions were chosen so that the apparatus would fit the geometrical constraints imposed by operation on a wiggler side station where access to the beam is limited on one side by a

hutch wall. The positioner is small and light, so it can be put in a briefcase and carried to different synchrotron facilities. It can be set up rather easily: in a matter of hours one can transform an ordinary XAFS beamline into one capable of operating in the glancing-incidence mode.

The design of the positioner is rather versatile. With the rotation stage removed a long x-ray mirror (e.g. a piece of bare or metal coated glass) can be mounted on the platform to be used as a low-pass filter to eliminate higher-order harmonics from the incident beam. Given the ease with which the mirror can be aligned (see section III.1.4) and the over 95% reflectivity for the fundamental frequency, the mirror filter provides a preferable alternative to detuning the two crystals of the x-ray monochromator from parallelism. The detuning method usually wastes 50% or more of the incoming photons and does not eliminate the higher-order harmonics as cleanly as the mirror does.We gave one of these positioners to C.E. Bouldin for the routine rejection of harmonics on beamline X23-A2 at the Brookhaven National Synchrotron Light Source.[7]

With the mirror mounted on the lower surface of the platform the incoming x-ray can be reflected downwards onto an air-liquid interface[8-16], in this manner the surfaces of liquid samples can be studied in glancing-incidence.

Compared with a standard x-ray goniometer our positioner has the following disadvantages: i) the pivot point of the tilting angle φ is not in the sample surface but rather about 5 cm below. Thus when the angle has been changed by a large amount the sample surface center is also moved vertically by a few μm and one has to translate the sample vertically to compensate the move; ii) only one dimensional rotation is available.

III.1.2) The Sample Azimuthal Rotation Stage

Single crystal samples are mounted on the rotation stage shown in Fig. 3, which can be spun at 40 Hz. The spinning of sample can reduce the magnitude of Bragg diffraction peaks in the EXAFS spectra [17]. The wobbling of the stage surface during the spinning is

less than 0.2 mrad. This is achieved by using a rather long rotating shaft to separate the two ball bearings as far as possible. The translational motion of the shaft relative to the ball bearings is prevented by an axially assembled external ring (see Fig. 3).

In experiments in which the sample is not spinning, this freedom of rotation can be used to choose specific crystallographic directions in MBE-grown films without having to realign the tilting angle φ of the sample relative to the X-ray beam (Fig. 1). Choosing proper azimuthal incident angles can minimize the occurrences of the Bragg diffraction from the single-crystal film in the energy region of interest. (See section III.1.4.)

The rotation stage is equipped with 3 set screws to permit alignment of the normal of the sample surface to the rotation axis of the rotation stage. This is normally done by shining a laser beam onto the sample surface at an incident angle of ~ 10°, observing the reflection spot on a scaled paper several meters away while turning the stage and adjusting the screws until the spot is stationary. The total-electron-yield detector (see section III.2.1) is mounted on this stage or a plastic chamber is mounted on the stage to keep samples under an atmosphere of an inert gas.

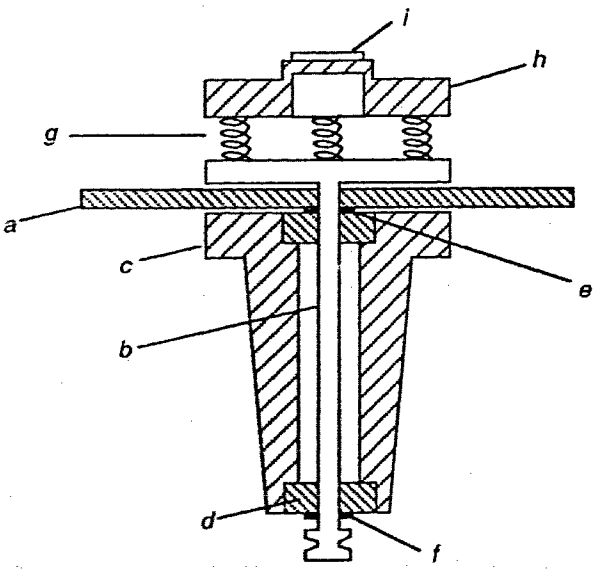

Fig. 3 Sample rotation stage: *a*, platform of the positioner; *b*, rotating shaft with one end connecting to the rotation plate and the other end to a pulley which is driven by a DC motor; *c*, shaft housing which is mounted on the platform; *d*, ball bearings; *e*, several 60 μm thick flat rings; *f*, flat rings and an axially assembled external ring; *g*, springs and adjusting screws (not shown); *h*, sample chamber or total-electron-yield detector housing; *i*, sample.

III.1.3) The s_1 and s_2 Assemblies

When the sample is inserted into the beam, usually the sample surface has a transverse tilt angle α with respect to slit s_1 due to the wedge angle of the substrate and the construction of the positioning stage on which the sample rests. In this case the measured incident angle of the beam φ' is affected by the wedge angle α. As shown in Fig. 4, if we denote the surface normal direction as $\hat{z}$, when the wedge angle α is nonzero the surface normal is along $\hat{z}'$ direction.

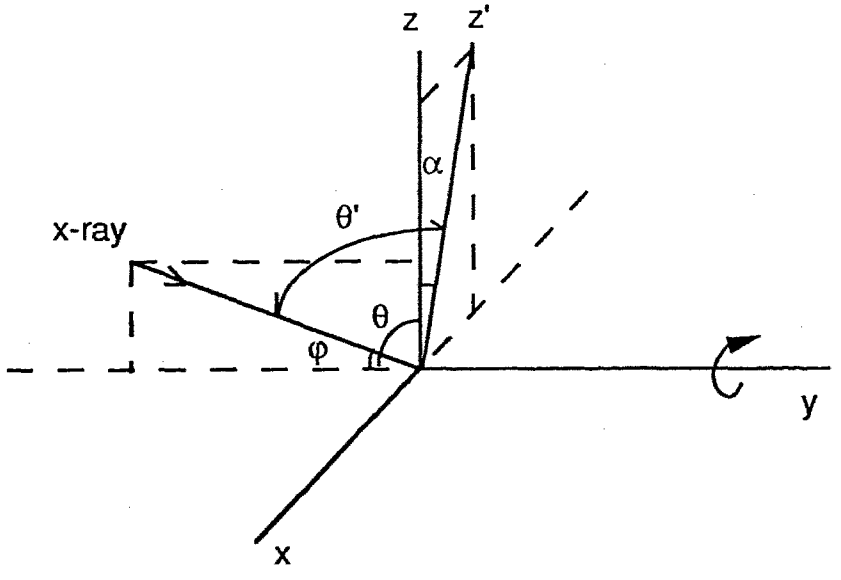

Fig.4 Relationship between the incident angle φ and the wedge angle α.

By definition we have

$$\cos\theta = \cos(\frac{\pi}{2} - \varphi) = \sin\varphi \text{, where } \varphi \text{ is the incident angle when } \alpha = 0.$$

Similarly $\cos\theta' = \sin\varphi'$.

On the other hand we can write $\cos\theta'$ in terms of the quantities in the original coordinate system

$$\cos\theta' = (-\sin\varphi\,\hat{y} + \sin\varphi\,\hat{z})\cdot(\sin\alpha\,\hat{x} + \cos\alpha\,\hat{z}) = \cos\alpha\sin\varphi .$$

So we have

$$\sin\varphi' = \cos\alpha \sin\varphi . \qquad \text{(III-1)}$$

It is relatively easy to adjust the slit s_1 such that the transverse tilt angle α between the sample and s_1 is of the order of 10 mrad (see section III.1.4). Then the deviation of φ' from φ is less than $10^{-4}\varphi$ which is negligible. However, it can cause a higher background and unwanted Bragg peaks in the detected signal due to part of the crystal substrate being exposed to the direct incident beam. To eliminate this problem, we leave the sample as it is but use the slit s_1 and s_2 assembly to define the beam path such that α is reduced to the minimum.

Slit s_1 (a Huber slit) is mounted on a transverse rotation stage driven by a motor micrometer [18] such that the transverse tilt angle of s_1 relative to the x-ray beam can be adjusted in steps of 4 μrad each. Slit s_2 is also mounted on a similar transverse rotation stage which is set on a vertical translation stage driven by a stepping motor. Slit s_2 has half of it being a normal slit and the other half a beam stopper. The base of the slit can be moved transversely relative to the x-ray beam by sliding in a dovetail groove to leave either the slit side or the beam stop side in the beam path. Ideally, if there is no additional divergence of the reflected beam due to the sample surface, one should use the slit half of s_2 which has the same width of s_1. In practice, the metal crystal substrates could be very imperfect in terms of the macroscopic flatness so the divergence of the reflected beam could be very large . To have enough counting rate in the I_r detector it is then necessary to open s_2 up. At the same time we want the lower jaw still being parrallel with s_1. The procedure of doing this is to align the slit half of s_2 with respect to s_1 first, then push s_2 along the dovetail groove to let the beam pass from the beam stop side. The angular disturbance of this manoeuver on the parallelism between s_1 and s_2 depends on the accuracy of the machining of the moving part of s_2 and the dovetail groove. It is less than 0.3 mrad as estimated from the nominal accuracy of the milling machine.

III.1.4) Alignment Procedures

First the two micrometers associated with the vertical opening of the slit s_1 are calibrated against the actual slit vertical opening measured by using the diffraction pattern produced by a He-Ne laser. The precision of this method is about ±5 μm.

To reduce the wedge angle of the sample with respect to slit s_1 we first tilt the sample to an angle φ (see Fig. 1) and position the sample height such that both the direct and reflected beam are detected by a Polaroid picture set in front of the I_r chamber. Rotate the slit s_1 to reduce the wedge angle shown on the picture. Repeating this procedure two or three times we can reduce the angle α to less than 10 mrad. A more accurate way is also possible which involves tilting the sample to a negative φ, sweeping the sample vertically through the x-ray beam and measuring the slope of the direct beam intensity as a function of the sample vertical position. This method is expected to have an accuracy of reducing α to a few tenth of a mrad, but it is relatively time consuming. In practice we found that the alignment by Polaroid pictures plus moving the sample vertically away from the beam by about 20 μm would be good enough to eliminate the effects of the transverse tilting angle.

For experiments concerned with total reflection from the sample surface, especially multilayer samples, the initial alignment (to set $\varphi = 0$) is crucial. The x-ray beam from the monochromator is selected by slit s_1. With the sample absent, slit s_2 is moved to define the optical path for $\varphi = 0$. This is done with the vertical translation stage whose position is controlled by a stepping motor (1200 steps/mm) (Fig. 1). The parallelism of s_2 with s_1 is set by maximizing the signal in I_r as s_2 is raised and, if necessary, rotated. With the sample centered on the bottom of the stage as shown in Fig. 2, its $\varphi = 0$ position is first roughly adjusted by eye. This is facilitated by ZnS fluorescent screens with ruled grids mounted at each end of the platform P and on the face of slit s_2. The sample is then raised out of the beam by computer control. With the beam stop side of slit s_2 put in the beam path, s_2 is lowered until the ion chamber (I_r) receives only a fraction $\varepsilon \sim 0.05$ of the direct beam.

Upon lowering the sample, while maintaining a fixed angle relative to the beam by turning both micrometers in unison, the signal measured in I_r will increase only if $\varphi > 0$. On the other hand, if $\varphi \leq 0$, as the sample is lowered it will start to block the direct beam and the signal monitored by I_r will decrease. Thus $\varphi = 0$ can be determined in an iterative manner by finding the minimum angle producing a reflected beam, i.e., showing an increased signal in I_r as the sample is lowered into the beam.

For very flat samples, such as metal films evaporated on 3 cm diameter optical silica windows, we could achieve a satisfactory alignment in 10 minutes or less. For the MBE-grown samples (~1.5 cm in diameter) the first alignment normally takes about 30 minutes, after that each realignment takes about 10 minutes. This rapid alignment is an useful feature for measurements with synchrotron radiation since time allocated on a beamline for a given experiment is very limited. For very flat samples like the films evaporated on silica windows, the $\varphi = 0$ can be located within ± 0.3 mrad.

III.2) Signal Detection

In our experiments we usually monitored XAFS signals in reflectivity, fluorescence and total-electron-yield simultaneously. The detectors used for monitoring the reflectivity were standard 6" or 12" long ionization chambers provided by SSRL. In the following, the total-electron-yield detector and the fluorescence detector constructed in this work are described, then the questions concerned with the Bragg peak contamination and the optimization of incident angles are addressed.

III.2.1) Total-electron-yield Detector

A total-electron-yield detector used in glancing-incidence EXAFS was designed and constructed in this work.[19] A schematic view of the position of the total-electron-yield detector is shown in Fig. 1. With this set-up, total-electron-yield, fluorescence and reflectivity EXAFS measurements can be made at the same time. In Fig.5 a detailed view of

secondary fluorescence to a minimum. The cap, *a*, has two windows, both covered with 30μm thick Kapton. The roof of the cap has a thickness of 0.64mm which enables 98% of the Ni K_α fluorescent X-ray photons to pass through.

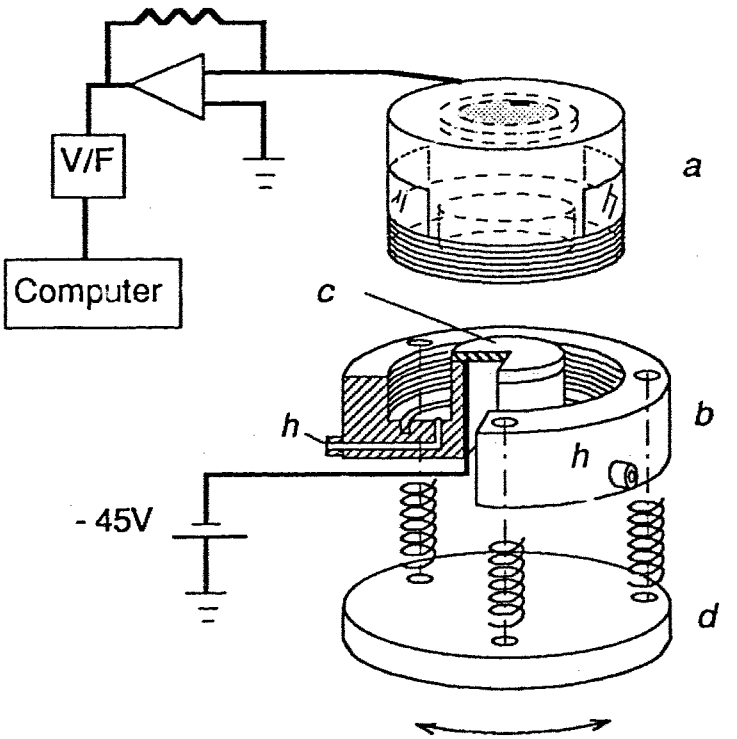

Fig.5. Schematic view of the total-electron-yield detector: *a* is the cap; *b*, the base; *c*, the sample holder; *d*, the rotatable stage and *h* indicates the holes for gas circulation.

As shown in Fig. 5, the cap, height - 2cm, diameter - 3.5cm, is screwed into the base, *b*, and the joint is O-ring sealed. On the base, two 1.2mm diameter holes, *h*, provide the input and output for He gas circulating at atmospheric pressure. The sample holder, *c*, is a Cu disk which is glued on the base and is biased to -45V by a battery. The sample can be secured on this holder by using two side clamps or if the substrate is ferromagnetic by placing a small magnet in the hollow cylinder underneath the Cu disk. The electrical connection between the sample and the Cu disk is obtained through direct contact. The positive electrode is made of aluminized mylar with a thickness of 15μm and with its aluminized side toward the sample. The mylar and the electrical lead are glued between two teflon O-rings which are then glued to the inside top of the cap. The aluminized mylar was stretched taut when it was glued on the teflon O-ring in order to have a ripple-free surface. This circumvented the difficulty of gluing the mylar directly onto the inner surface of the cap without introducing ripples. The area of the mylar is chosen to be approximately equal to that of the sample disk such that the electric field between the electrodes is close to uniform. The electrical connection between the external electrical lead and the aluminized mylar is made with silver epoxy.

With the sample mounted, the detector chamber is then spring loaded onto the rotatable stage, *d*, by three screws separated by 120° (Fig. 5). The screws can be adjusted until the normal to the reflecting surface of the sample is collinear with the rotation axis of the rotation stage as described earlier.

Fig. 6 shows two consecutive glancing-incidence EXAFS spectra taken on a buried Ni film with a thickness of 37 monolayers. The inset of Fig. 6 shows the raw data for one of the spectra. The diameter of the Al/Ni(37ML)/Fe(001) sample was 18 mm diameter. The Al protection layer for this sample had a thickness of 72Å. The incident tilting angle φ was about $2\varphi_c/3$ where the effective critical angle φ_c was defined to be the angle at which the angular reflectivity curve of 8033 eV photons was half of its maximum value. The

azimuthal incident angle was selected to minimize the occurrences of the Bragg diffractions from the single crystal film in the energy region of interest.

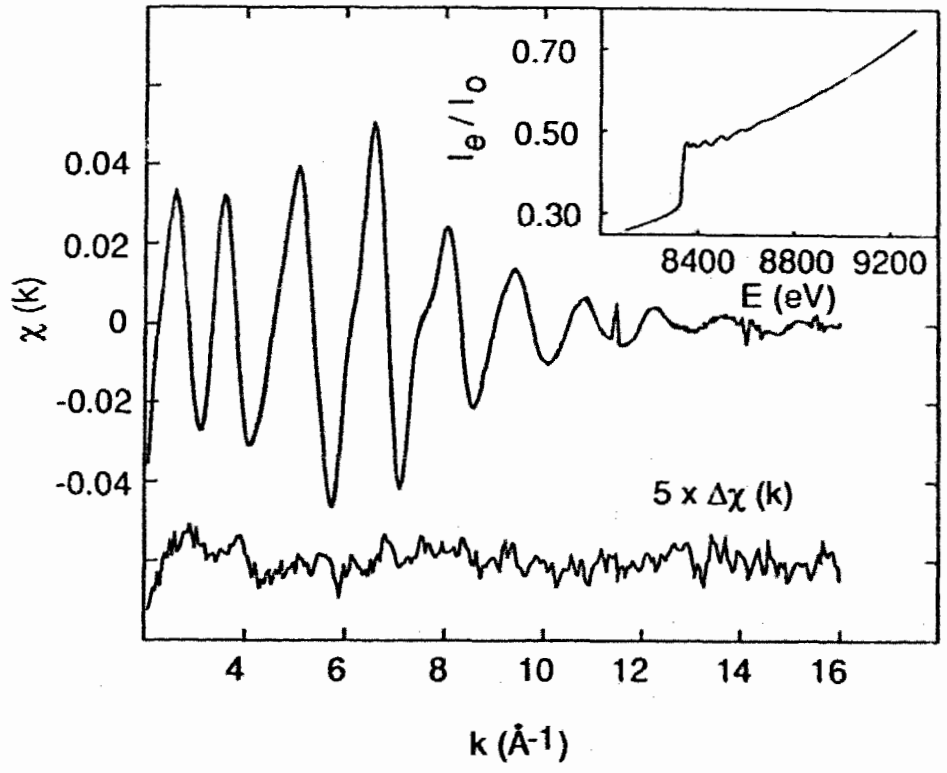

Fig. 6 The EXAFS interference function $\chi(k)$ obtained from the total-electron-yield for Al/Ni(37ML)/Fe(001). The data for two consecutive scans are plotted. The difference of the two scans is enlarged by a factor of 5 and shown below the data on the same horizontal scale. The inset shows the total-electron-yield current normalized to the incoming beam intensity. The spikes around 11.5Å^{-1}, 14Å^{-1} and 15.5Å^{-1} are not Bragg diffraction peaks but are identified as monochromator crystal "glitches".

We have examined the noise level in the total electron yield, fluorescent and reflectivity detection modes by comparing data taken simultaneously. At the bottom of Fig.6 is shown an enlargement of $\Delta\chi(k)$, the difference between two consecutive electron yield interference functions at $2\varphi_c/3$. The root-mean-square difference of the consecutive scans is 7×10^{-4}. For the reflectivity EXAFS, the same parameter was 7 times larger at the same angle. The larger noise level in the reflectivity is partially associated with the small

signal to background ratio which occurs at angles less than the critical angle. This is consistent with the suggestion that the reflectivity EXAFS signal is optimized at larger angles [20]. At $\varphi \approx \varphi_c$ all the three detection modes work reasonably well as shown in Fig. 7(upper panel): the root-mean-square difference of two consecutive scans was 1×10^{-3} for electron yield and a factor of two larger for reflectivity and fluorescence yield EXAFS. It seems that from the statistical viewpoint, the total-electron-yield detection often gives a better result than the other two methods. However, it may not be appropriate at this time to generalize above observation. We have noticed that satisfactory performance of the total-electron-yield detector has been always in the case that the second order harmonics contents in I_0 are well suppressed, e.g. when Si(111) crystal is used in the monochromator. In fact, in our experience whenever Si(220) crystal was used in the monochromator the signal/noise ratio in total-electron-yield was found worse than in fluorescence.

In Fig. 7(lower panel) the places marked by arrows correspond to the monochromator "glitches" in the incoming x-ray beam (I_0).[21, 22], which are the sharp intensity drops or increases in I_0 when the monochromator crystal geometry satisfies Bragg's equation for more than one set of lattice planes simultaneously. It appears that the total-electron-yield detection is more sensitive to the presence of monochromator "glitches" than fluorescent or reflectivity detection, especially when the incident angle is greater than or equal to φ_c. Often the amplitude of the spikes could be reduced to a tolerable level by further detuning the monochromator.

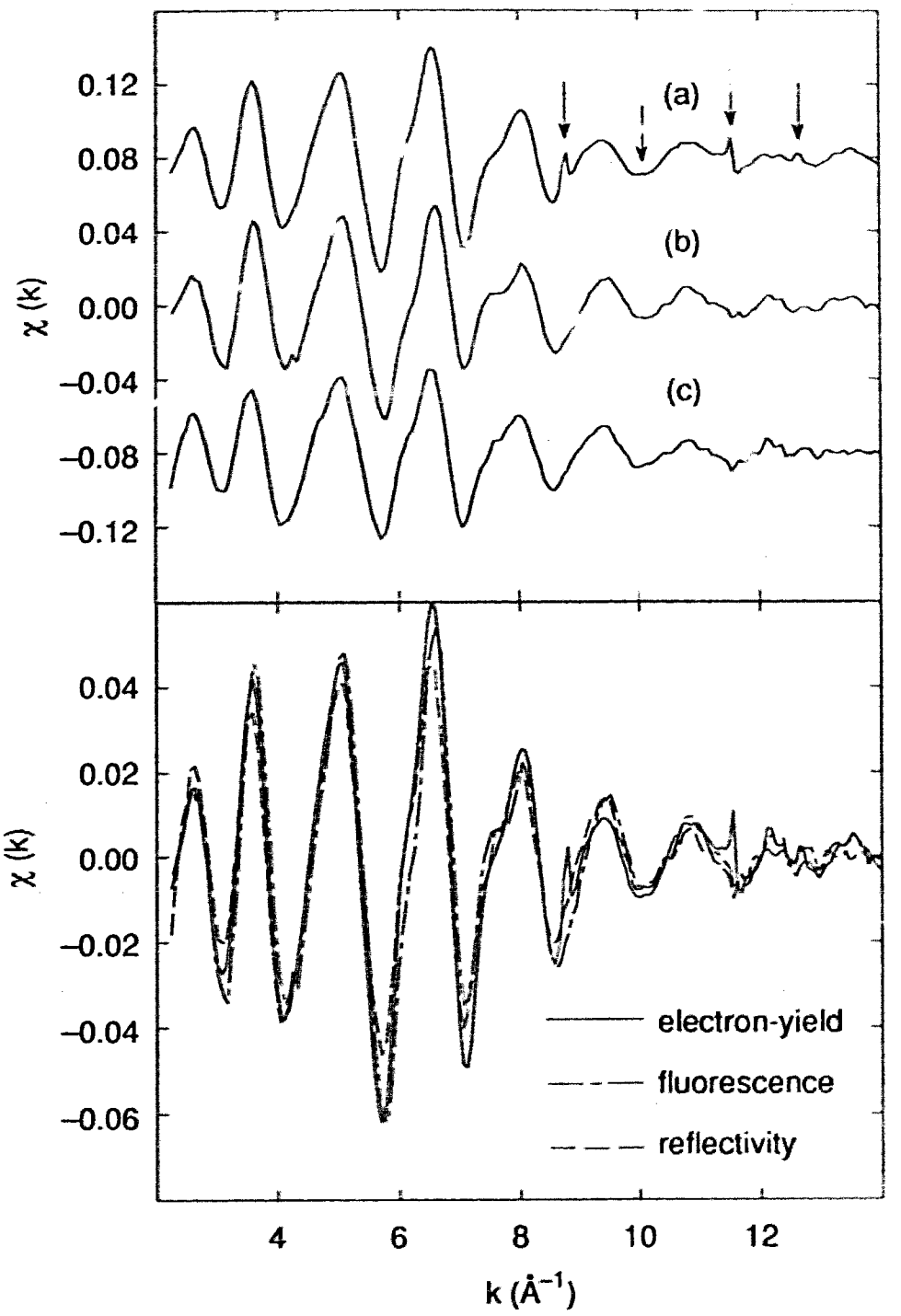

Fig. 7 In the upper panel, the EXAFS interference function $\chi(k)$ at $\varphi \approx \varphi_c$ for Al/Ni(37ML)/Fe(001) for three detection modes: (a) total-electron-yield; (b) fluorescence and (c) reflectivity. The contribution of monochromator "glitches" are indicated by arrows. In the lower panel, the same three $\chi(k)$ as in the upper panel are plotted to the same scale.

III.2.2) Wide-aperture Fluorescence Detector

The fluorescence detector used in our experiments was either a gas ionization chamber or a large area silicon diode (for some of the 37 ML Ni data). The large area silicon diode was extensively described in Ref.23 and Ref.24, here we briefly describe the gas ionization chamber.

The design of the gas ionization chamber was based on that of Stern *et al.* [25], some modifications were made with the idea in mind to increase the detecting sensitivity to cope with the thin sample layer cases. Fig. 8 shows the schematic view of the fluorescence chamber. Like the case for the total-electron-yield detector, the output current signal goes to a preamplifier, with an output voltage of 10 volts per 10 picoamperes, and then after a voltage to frequency converter the signal goes to a computer memory storage.

The working mechanism of the detector is the same as in other ionization chambers. The fluorescence photons enter the chamber from the thin aluminized mylar window and ionize the gas molecules in the chamber through collisions. The ionized electrons and ions move in the opposite direction under influence of the electric field between the meshes, usually the electrons are collected to generate a current pulse in the preamplifier. The bias voltage on the meshes were chosen to be in the plateau region of the I-V curve of the detector.

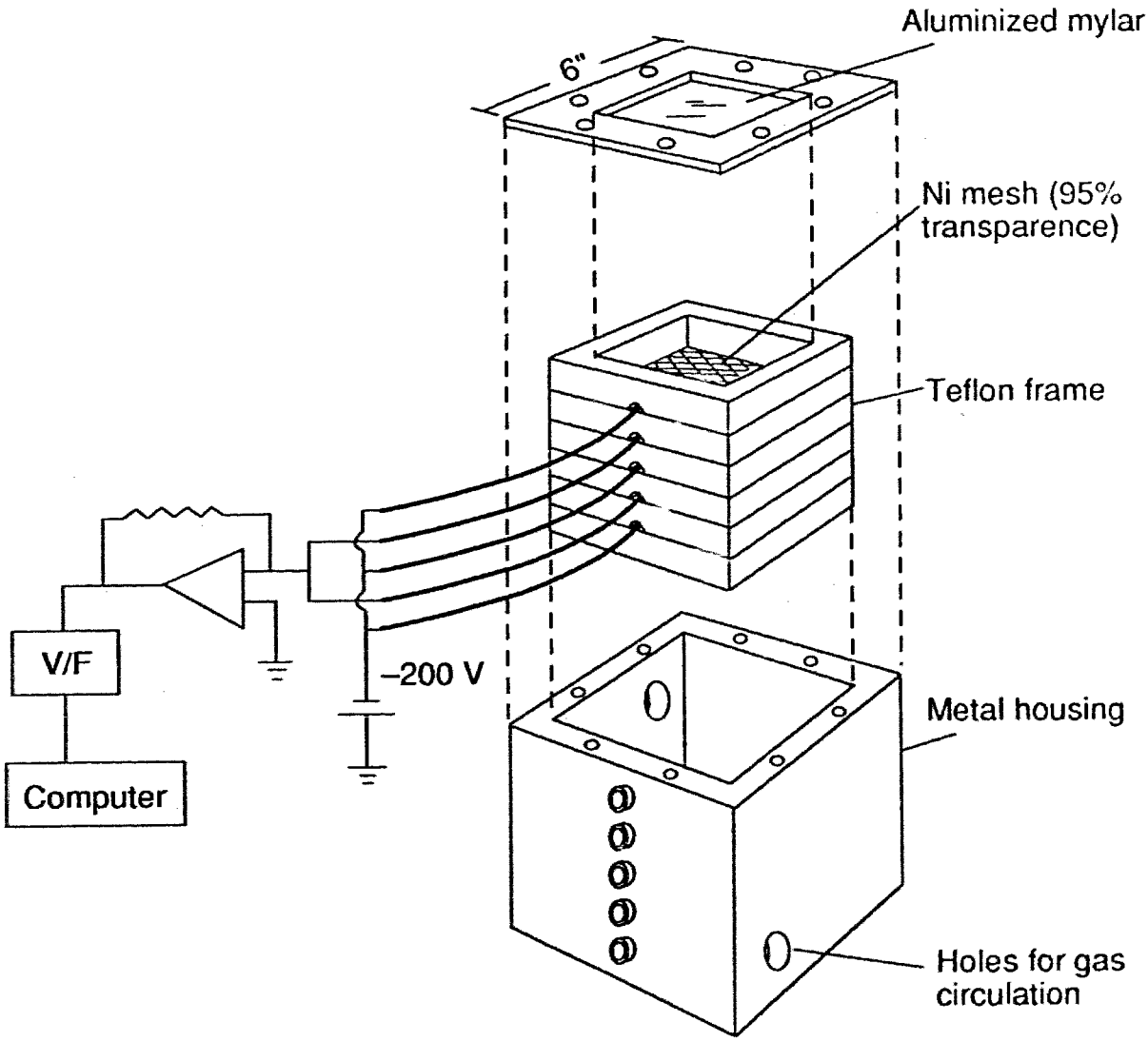

Fig.8 A schematic view of the wide-aperture fluorescence chamber.

In an glancing-incidence experiment, the distance between the sample surface and the aluminized mylar window was kept to about 3 cm, so the solid angle suspended by the detector to the center of the sample was ~ 0.85π. Under the same experimental conditions, the performance of this fluorescence chamber was compared with another gas ionization chamber which used Lytle's design [26]. We found that the signal to noise levels were comparable but the sensitivity of ours was higher than that of Lytle type. The gas used in the chamber was either argon or nitrogen.

III.2.3) Bragg Peak Problem

In our experiments a highly collimated x-ray beam is incident at some glancing angle on a crystal sample and the x-ray photon energy is continuously changed so that the absorption coefficient as a function of energy is monitored. It is easy to visualize that in this process the Bragg's diffraction conditions can be satisfied at some x-ray energies with appropriate sample geometries. If a beam, Bragg reflected coming out off the sample surface, falls into the solid angle subtended by an ionization chamber, we will have a non-EXAFS peak in the signal. Some portions of the spectrum can be ruined by those Bragg peaks as shown in Fig. 9.

There have been several methods proposed with some success to reduce or eliminate the effects of Bragg peaks in XAFS spectra, such as spinning the sample around the surface normal[17], using multi-channel fluorescence detectors to spatially discriminate diffraction peaks[27], using a high energy resolution detector (usually a solid-state detector) to distinguish the fluorescent line and the higher energy diffraction lines,[28] and using total-electron-yield detection.[29] The methods we have applied are: i) spinning the sample, in which case the total-electron-yield detector with the current design can not be

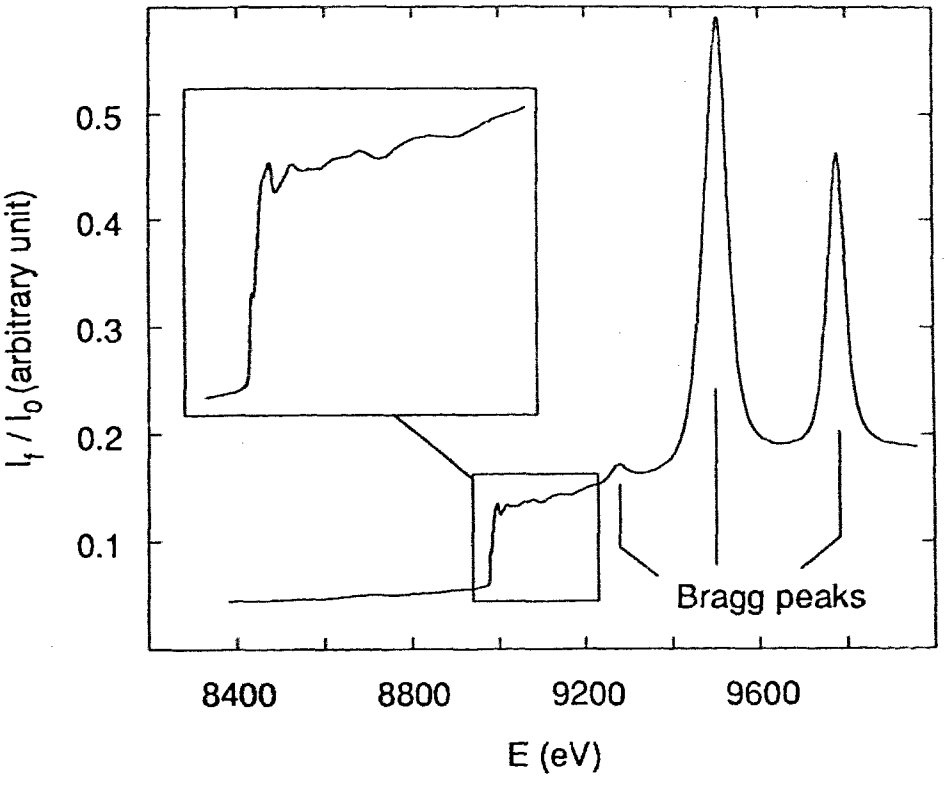

Fig. 9 A fluorescence scan from Au/Cu(8ML)/Ag(001) contaminated by Bragg peaks. The inset shows an enlarged view of the uncontaminated portion of the spectrum.

used; ii) selecting the optimized azimuthal angles with the sample kept stationary and cross-checking the spectra obtained simultaneously in the three detection modes: reflectivity, fluorescence and total-electron-yield. The spinning method averages out the Bragg peaks, but at the same time the sample wobbling introduced by the rotation degrades the data quality. On the other hand, as demonstrated in Fig.6 and Fig.7, it is possible to obtain spectra free from Bragg peaks by keeping the sample stationary and choosing the azimuthal incident angle carefully. The following are several "rules of thumb" on distinguishing Bragg peaks from other spurious features in a spectrum: i) Bragg peaks usually appear only in one channel (most often in the fluorescence chamber) but not in the other two; ii) they change positions in an energy spectrum when the tilting angle and the azimuthal angle of

the sample are changed, usually changing the tilting angle is enough to tell; iii) usually the Bragg peaks are broader than "glitches".

As mentioned before the total-electron-yield detector is largely transparent to the Ni K_α x-ray photons, so the detector is even more transparent for the Bragg diffractions occuring above the K-edge of Ni or Cu. This transparency plus the fact that the diffraction photons have a very short transit length (several ten Å) in the sample virtually eliminate the effects of the Bragg diffractions in the total-electron-yield signal[29]. In Fig. 10 an example is shown for the comparison between the fluorescence and total-electron-yield when Bragg peaks are detected.

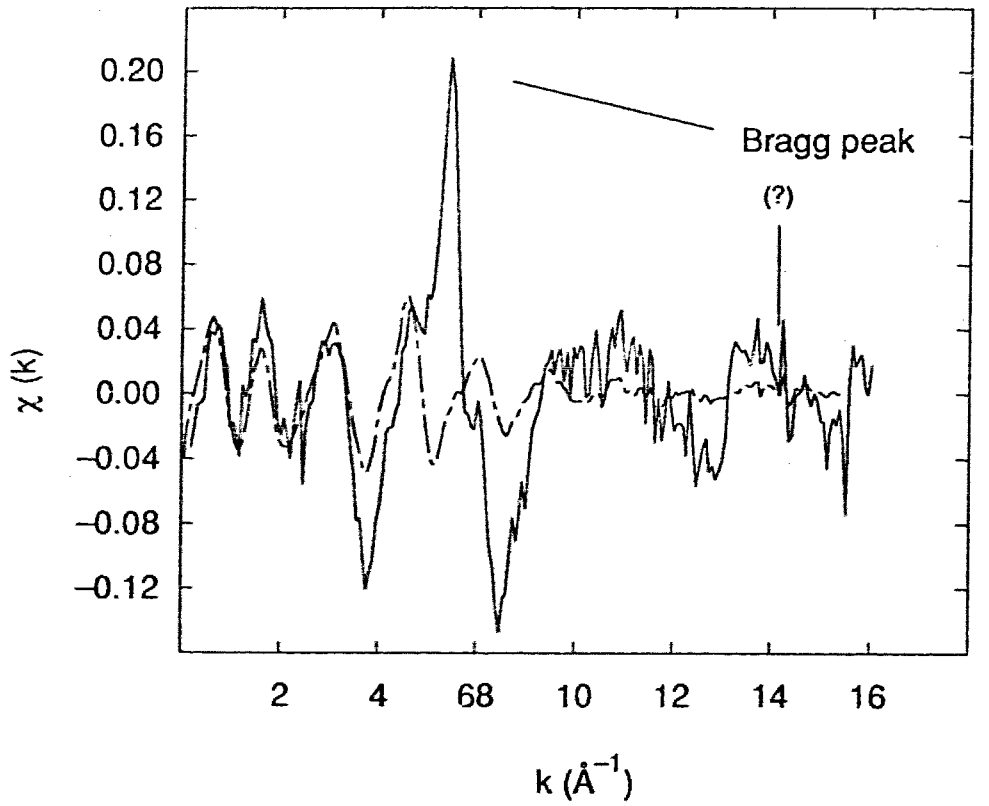

Fig. 10 The EXAFS interference functions detected simultaneously by fluorescence (solid) and total-electron-yield (dash-dot). The fluorescence signal is heavily contaminated by Bragg peaks, while the total-elctron-yield appears to be unaffected.

III 2.4) Comparison of the Three Detection Methods

The following discussion indicates some merits and limitations for each of these detection methods in the context of the systems studied in this thesis. Because the observations are limited in the scope reached so far, the discussion below is by no means thorough and conclusive. A more general discussion about different detection methods can be found in Ref. 30. In Table I. the advantages (+) and disadvantages (–) of each method are assigned.

Table I. Comparison of fluorescence (I_f), total-electron-yield (I_e) and reflectivity (I_r)

	I_f	I_e	I_r
XANES	+	–	–
Signal/Background	++	–	+
Signal/noise	+	++	–
Bragg peak suppression	– –	+	+
Insensitivity to glitches and harmonics in I_o	+	–	(–)

The reason why XANES from fluorescence is better (in the sense of less distortion) than from the other two methods is that it is relatively easy to separate the fluorescence signals from the sample layer and the other layers. However this separation is not possible in the other two methods. The ratio of Signal/Background is defined to be the ratio between the edge jump height (see Chapter V and VI and the pre-edge background signal strength. The higher this ratio is the less likely that the EXAFS interference function $\chi(k)$ will be distorted by some reproducible intensity modulations due to the nonlinearity between different detectors used for monitoring the incoming beam and the signal coming out from

the sample. The fluorescence detection is especially superior in this regard when the fluorescence signals from the sample layer and others are well separated in the energy spectrum, e.g. in the case of Cu in Au/Cu/Ag. Although one can have a large Signal/Background ratio in the reflectivity when φ approaches φ_c, the catch is that the anomalous dispersion distortion is also most severe there. The Bragg diffraction contamination is the most severe drawback of the fluorescence method. [17] In the total-electron-yield the effects of Bragg diffraction are reduced by about 2 orders of magnitude[19, 29] compared to that in the fluorescence case (also see Chapter III for more). In the reflectivity, because of the limited solid angle subtended by the I_r detector, the Bragg diffraction contamination is also far less severe than in fluorescence. The total-electron-yield and reflectivity are both more vulnerable to the monochromator glitches than the fluorescence, and in this respect the total-electron-yield is the worst which may be partially related to some harmonic content of the glitches. The reason why the reflectivity should be sensitive to the glitches is not clear.

In summary, the overall performance of fluorescence detection is better than the other two methods in the kind of experiments described here. However, it is convenient and very useful to monitor all the three detection modes simultaneously in the experiment so that the Bragg diffraction contaminations in the fluorescence signal can be readily identified and appropriate experimental manoeuvres can be taken to eliminate them.

Chapter IV Sample Preparation

In this chapter the sample preparation and related techniques are described.

IV.1) The MBE Facility

The epitaxial films were grown in a Physical Electronics (PHI) Model 400 MBE system. A schematic layout of the system is shown in Fig. 1. The system consists of two interconnected vacuum chambers, one for growth and the other for analysis. The vacuum is maintained by an ion pump connected to the analysis chamber and a cryogenic pump connected to the growth chamber. During the sample growth the base pressure was below $5x10^{-10}$ Torr. Each chamber has an ionization gauge to monitor the vacuum. Two sorption pumps are connected to the analysis chamber for initial pumping of the system from atmosphere pressure before the cryogenic and ion pumps are turned on.

Through a pressure-driven valve the analysis chamber is connected with the small intro-chamber which is for mounting samples. During mounting the sample arm is retracted into the intro-chamber and sealed off from the rest of the system. The intro-chamber is then back-filled with dry nitrogen and opened to the atmosphere. The overpressure of N_2 is maintained to minimize contamination of the sample arm rod and sample manipulator. After the sample is mounted the intro-chamber is sealed and pumped by a turbopump to ~10^{-6} Torr, then the sample can be transfered into the UHV system. The transfer rod of the sample arm is driven by a electrical motor and it has a sample manipulator attached in the end on which the sample is mounted. The sample manipulator can be rotated around two axes, one is along the transfer rod and the other is perpendicular to the first one. The manipulator also contains a filament behind the sample holder for annealing the substrate. Substrate temperatures are measured by a thermocouple pressed on the back of the sample holder and can reach ~650-700°C with the substrate heater.

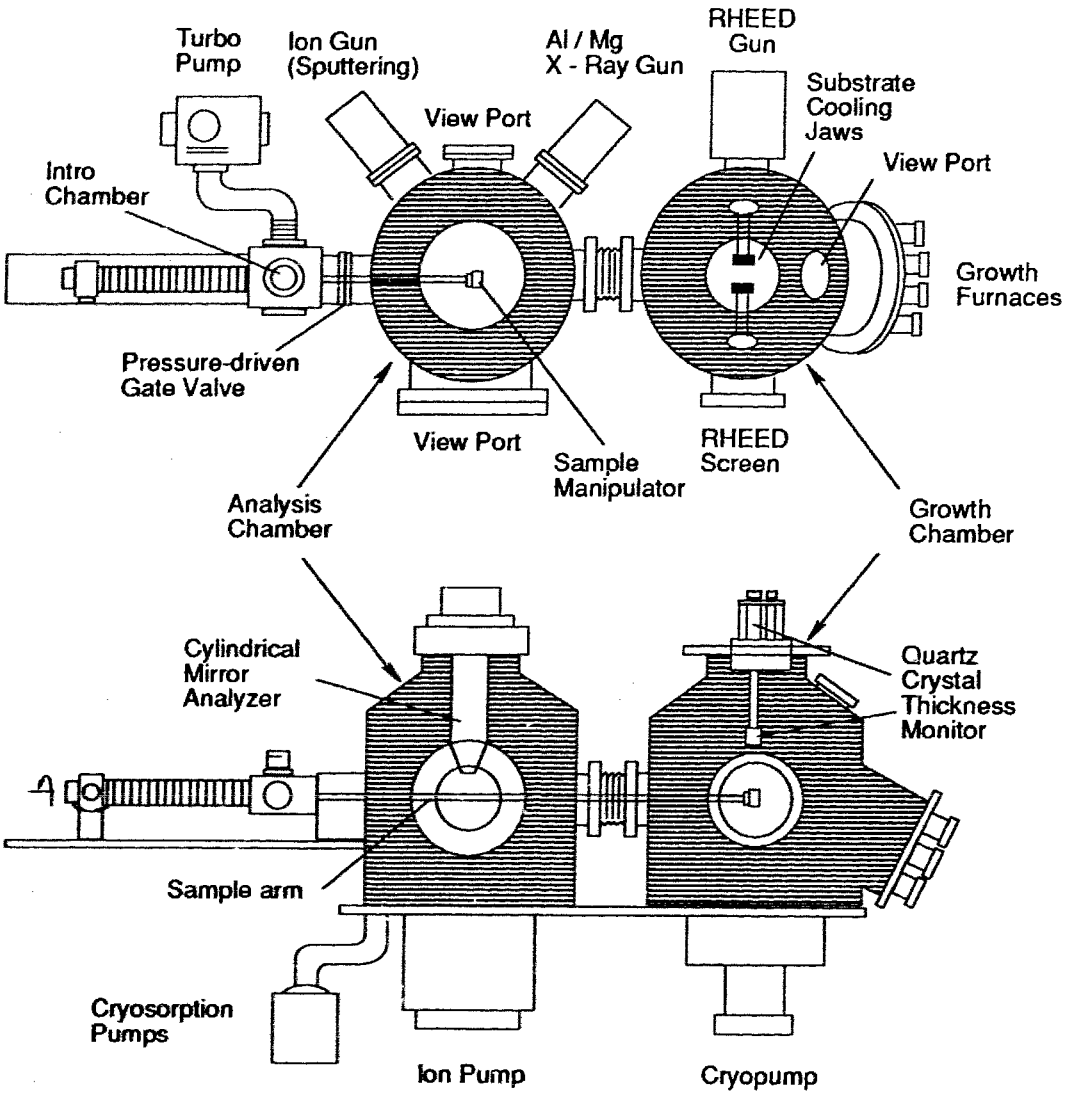

Fig. 1 Schematic layout of the MBE system.

The analysis and growth chambers are equipped with various surface and magnetic study tools. In the following we very briefly describe the ones used in this work. More detailed descriptions of the conventional surface science tools can be found in textbooks[1], more about the particular MBE system can be found in Ref.2 and Ref.3.

The analysis chamber has a PHI model 15-255GAR precision energy analyzer consisting of a PHI model 10-155 double pass cylindrical mirror analyzer (CMA) with a self-contained electron gun for angular resolved Auger Electron Spectroscopy (AES), and an ion sputtering gun for cleaning the substrate.

In AES one directs a high energy (~2 keV in our case) electron beam at a sample and collects the spectrum of backscattered electrons, $N(E)$. $N(E)$ exhibits an elastic peak (electrons that pass undisturbed through the solid) and a long tail produced by electrons that have lost energy to the solid. The electrons in this tail consist of primary electrons which exit the sample after losing energy in a single well-defined inelastic event and secondary electrons which lose energy through multiple inelastic collisions. The signal from the secondary electrons is structureless while the primary electrons reveal their origin in the derivative signal $dN(E)/dE$. The precise energy position of the sharp structure in the derivative spectrum provides the elemental signature of the surface. AES is mainly used for surface elemental analysis by comparing the measured spectra with a set of standard spectra listed in handbooks.[4] For transition metals (for those with number densities of the order of 70 atoms/nm^3) the technique is sensitive to the first 30 Å of the surface due to the limited inelastic mean from path of the primary Auger electrons.[5] By monitoring the reduction of the intensity of a particular AES feature of the substrate element A during the evaporation of another material B on the top, the film thickness of material B can also be estimated. This provides a means for cross-checking the film thickness and detecting if there are severe alloying events happening at the interface.

To use the sputtering gun (PHI model 04-191) the analysis chamber is first filled with argon to a pressure of 5×10^{-5} Torr. In the ionization chamber of the sputtering gun the

argon atoms are ionized by collision with electrons emitted from a filament. The ions are then accelerated to energies in the range of 0.5-5 keV (2 keV most of the time in this work) and collimated into a beam which strikes the substrate to remove the surface contaminants. The beam can be electronically deflected to raster over approximately one square centimeter area of the sample. Typical rates of removal from the target are ~1ML/min. During the sputtering the ion pump of the analysis chamber was turned off. It was turned on after the sputtering when the pressure had been reduced to a low 10^{-9} Torr level.

The growth chamber has a set of 8 evaporation furnaces enclosed in a liquid N_2 cooled shroud, a 3-10 keV electron gun and a conducting SnO_2 coated phosphor screen for Reflection High Energy Electron Diffraction (RHEED), and a temperature controlled quartz thickness monitor along with a pair of liquid N_2 cooled copper jaws for cooling the substrate for low temperature growths.

Two types of evaporation furnaces were used. Fe and Ni were evaporated from pure metal wires wrapped around tungsten heating filaments. Al and Au were evaporated from boron nitride crucibles which were heated by tungsten coils enclosing the crucibles. The furnaces were equipped with electrically controlled pressure-driven shutters which can initiate or terminate the growth in a fraction of a second.

In the RHEED system, a 10 keV electron beam is directed towards the sample surface at small incident angles ranging from 0° to 5°. Electrons scattered through a small angle sample only the top 1-2 atomic layers of the crystal under these conditions. Therefore RHEED patterns are sensitive to the structure changes at the surface. Assuming elastic scattering of the high energy electrons from the surface atoms, RHEED patterns can be qualitatively interpreted in terms of kinematic theory as the diffraction from a 2 dimensional atomic sheet. Fig.2 schematically shows the origin of the pattern.

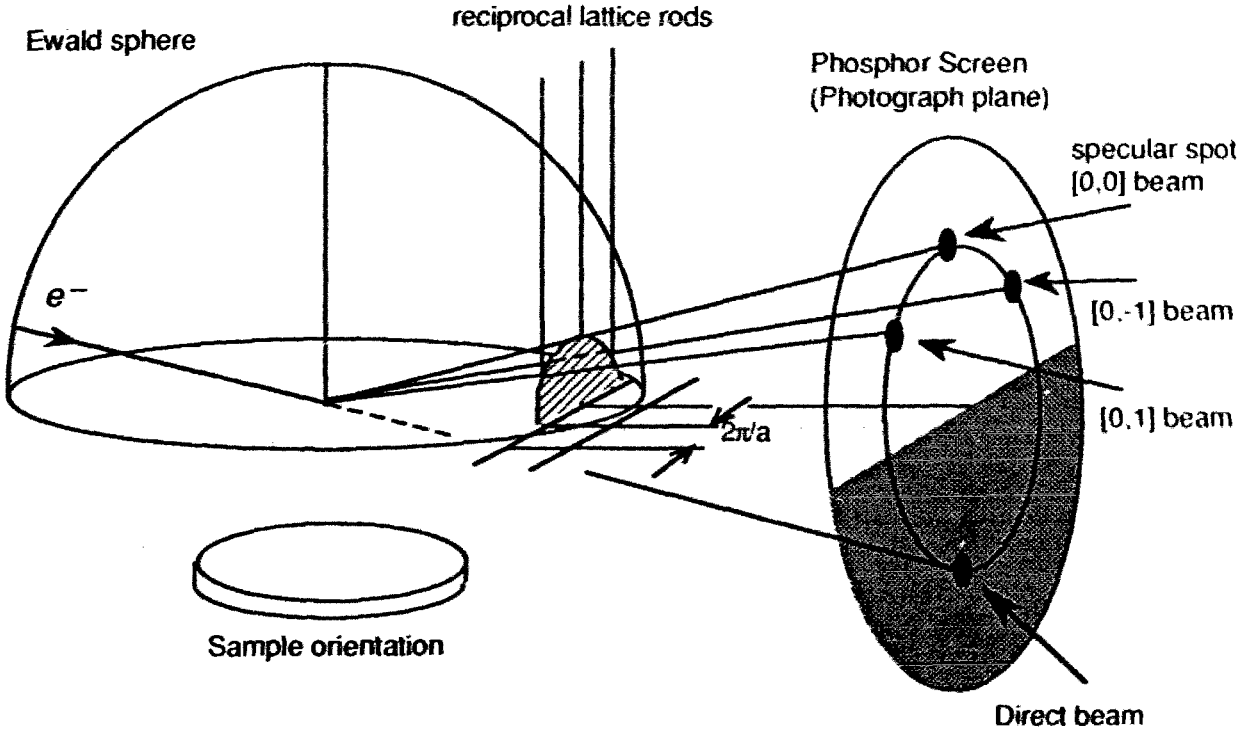

Fig.2 Ewald construction of a 2-D diffraction case.

When the sample surface is nearly perfect, e.g. that of a Fe whisker grown by chemical vapor deposition, the RHEED pattern would be just like that drawn in Fig.2, i.e. on the phosphor screen one really sees "spots" with sizes comparable to the electron beam size.[6] For a nonideal surface such as the Fe and Ag substrates used in this work, due to the finite width of the reciprocal lattice rods the result is a set of long RHEED "streaks" instead of well defined spots.

If the growth is in the fashion of one atomic layer at a time, i.e. the so-called Frank - Van der Merwe growth[1], the intensity of RHEED signal exhibits oscillations whose period exactly corresponds to the growth rate of a single atomic layer. This has been shown in both cases of semiconductor[7] and metal[6, 8]. This phenomenon has been extensively used to monitor whether the growth is in a layer-by-layer fashion and to accurately control the thickness of the film grown. Qualitatively, the oscillations can be understood in terms

of Frank-Van der Merwe growth: reflectivity maxima correspond to scattering from atomically smooth surfaces while reflectivity minima correspond to scattering from maximally disordered surfaces which occur at a half monolayer random coverage.

IV.2) Substrate Preparation

2.1) Cutting and Aligning the Substrate Crystals

The Fe single crystal substrates used in this work were in disk shape cut from single crystal plates grown by means of strain-anneal.[9] Altogether three pieces of the Fe substrate were used in this work, they were the only ones we had with a surface area large enough for performing the glancing-incidence XAFS experiments. The physical descriptions for the three substrates are listed in the following[2]

	Diameter (mm)	Thickness (mm)	Misorientation (deg)	Mosaic (deg)
Fe(001) A	13	0.35	< 0.5	<0.5
Fe(001) B	18	0.25	~2	~1
Fe(001) C	18	0.7	2.7±0.2	~1

The misorientation is between the normal of the physical surface and the normal of (001) planes. The degree of the misorientation was determined by taking Laue photos of the substrates. To do this, the crystal was mounted on a polishing jig using Crystalbond™ and the jig could be mounted on the Laue camera. Substrates with misorientation in the range shown in above list are usually refered as "vicinal" substrates. The substrates with misorientation within 0.25° are usually refered as "singular" Better orientated surfaces could have wider terraces which are crucial for an ideal epitaxial growth. From the thicknesses listed above, we can see that there is not much room for selecting the physical

surface to eliminate the misorientation, unless the sample diameter is reduced. It has been shown that with careful surface polishing preparations, epitaxial Ni films can be grown on the vicinal Fe(001) surfaces, even although the terrace is only in the range of 30 - 120 atoms.[2, 10, 11]

Three different Ag(001) substrates were used to grow the Cu/Ag(001) and Ni/Fe/Ag(001) samples. These substrates were cut from a boule using a spark cutter (AGIE -45LM). The original boule had an elliptical cross section. A 4 mm slice of it was first cut off using a 0.005" diameter Cu wire as the electrode and afterwards a cylindrical Cu cutter was used to cut a 15 mm diameter disk from the elliptical slice. Care was taken to minimize the possible defects in the crystals caused by the sparks. These Ag substrates were oriented so that their physical surfaces were aligned to within 0.2° of the (001) plane, i.e. they were singular substrates. The mosaic spread in these Ag substrates was less than 0.25°.

2.2) Polishing

The Fe substrates were mechanically polished before growing the samples for XAFS studies. This was needed because the same substrates were frequently used to grow samples for ferromagnetic resonance (FMR) studies, in which process the surfaces were usually scratched and the damages caused were too large to be removed by the sputtering and annealing process in UHV. Here we briefly describe the methods used in the polishing.

The surfaces of the substrates were polished on rotating soft tin plates with 6 μm and 1 μm diamond paste applied sequentially (using different plate for different diamond paste). The next step was to polish on soft polishing cloths* mounted on a rotating metal plate . 3 μm and 1 μm diamond paste was applied sequentially, with a new soft pad for each kind

---

* "BUEHLER POLISHING CLOTH" Catalog No. 40-7218, MICROCLOTH^R with adhesive backing for 8" wheel. BUEHLER 41 Waukegan Rd. Lake Bluff, IL 60044 USA]

of paste. A diamond thinner fluid** which served as a lubricant was added onto the tin plate and the soft pad periodically. In the whole process the polishing surface was kept we but not flooded. Before a fresh tin plate or new diamond paste was used, the polishing surface had to be conditioned for ~20 min by the jig. For this operation the sample on the jig was lifted away from the the tin plate. The criterion of a good conditioning was that the scratches on the metal ring of the jig were even in size. Each polishing step was finished when the substrate surface became shinier and all the relatively larger scratches caused in the previous step were removed. The next step used a commercial technique developed for Si wafers. The polishing agent was a colloidal silica slurry from RODEL Products§ , diluted in distilled water by ratio 1:10, and applied to their adhesive backed Politex pads. The average particle size was 50-70 nm. In this step the polishing fluid was kept flooded on the pad and supplied continuously, otherwise the polishing agent would dry up and become hard rather quickly which then could scratch the surface. The effect of this step could only be seen under a microscope: we used one with 400x magnification. The last step was to polish with distilled water for a minute or so to remove the colloidal silica on the surface. Then the substrate was dismounted from the jig and washed in an ultrasonic bath sequentially in acetone, trichloroethylene and methanol.

The polishing of the Ag substrates used in this work was done by our colleagues in the SFU surface science laboratory and a description of the procedure can be found in Ref.3. The Ag polishing was finished with electrolytic polishing.

For Fe substrates, the next step was to mount the substrate on the sample manipulator in the intro-chamber. In a 10^{-6} Torr environment the substrate was then heated up to about 175°C for several hours to outgas. Then the substrate was transfered into the analysis chamber to go through the sputtering and annealing cycles to get a clean surface. The

---

** Manufacturer for the paste and oil: MICRO METALLURGICAL LTD. 41 MAPLE AVE. Thornhill, ON L3T 3S9 phone:416-889-6231]

§ RODEL INC. 451 Belleve Rd. Diamond State Industrial Park Newark, Delaware 19713 USA]

sputter gun settings were 2 kV accelerating potential and 25 mA emission and during the sputtering the sample was moved around several times to ensure that the entire surface was rastered by the ion beam. The cleaning sequence involved the following: sputter 30-40 minutes at room temperature to remove C and O_2; a 20-30 minute combined sputter-anneal at 750°C; a 30 minute anneal at 750 °C; a brief sputter (a few minutes) to remove S that diffuses to the surface at high temperature. Then the sputtering gun and the sample heater were turned off at the same time. The minor damage on the surface in the last brief sputter was annealed out as the sample cooled to room temperature. Two things were checked to decide if it was needed to repeat the cleaning process: i) whether a sharp RHEED pattern was obtained and ii) whether the surface impurity level was too high. In the substrates prepared in this work the final impurity levels (in terms of the ratio of number of atoms at the surface) were not worse than C/O/Fe - 5/1/100 (no S visible).The number was obtained by comparing the relative peak to peak intensity of the different elemental Auger lines and the relative sensitivities of the elements were taken into account.[4]

For Ag substrates the procedure was similar: outgassing in the intro-chamber at 150°C for several hours; sputtering in the analysis chamber at room temperature for 30-40 minutes; annealing at 450°C for 20-30 minutes; a combined sputter and anneal at 450°C for about 30-40 minutes; sputter at 350 °C briefly (a few minutes) then turn off both the sample heater and the sputtering gun. The finished surfaces were free of surface contaminants within the detectable limit of the Auger spectra. More detailed investigations using both Auger and XPS showed that the upper limit of the contaminants on such surfaces is 0.05 at.%.[12]

IV.3) Sample Growth

Good epitaxial growth is anticipated when the lattices of the overlayer and the substrate are well matched. The lattice match could be i) the lattices of the overlayer and the substrate have both similar lattice spacings and the same structure, e.g. in the case of Al-Ag-Au (fcc); ii) only on particular planes such as Al, Ag or Au (001) on Fe (001) as shown in Fig. 3. The quantity used to describe the lattice mismatch between the overlayer and the substrate is usually defined as the percentage difference in lattice spacings of the natural phases, i.e. the so-called *misfit*, $(a_{overlayer} - a_{substrate})/a_{substrate}$. In the examples of lattice matches given above the misfit ranges from 0.2% (Al-Fe) to 0.7% (Ag-Fe).

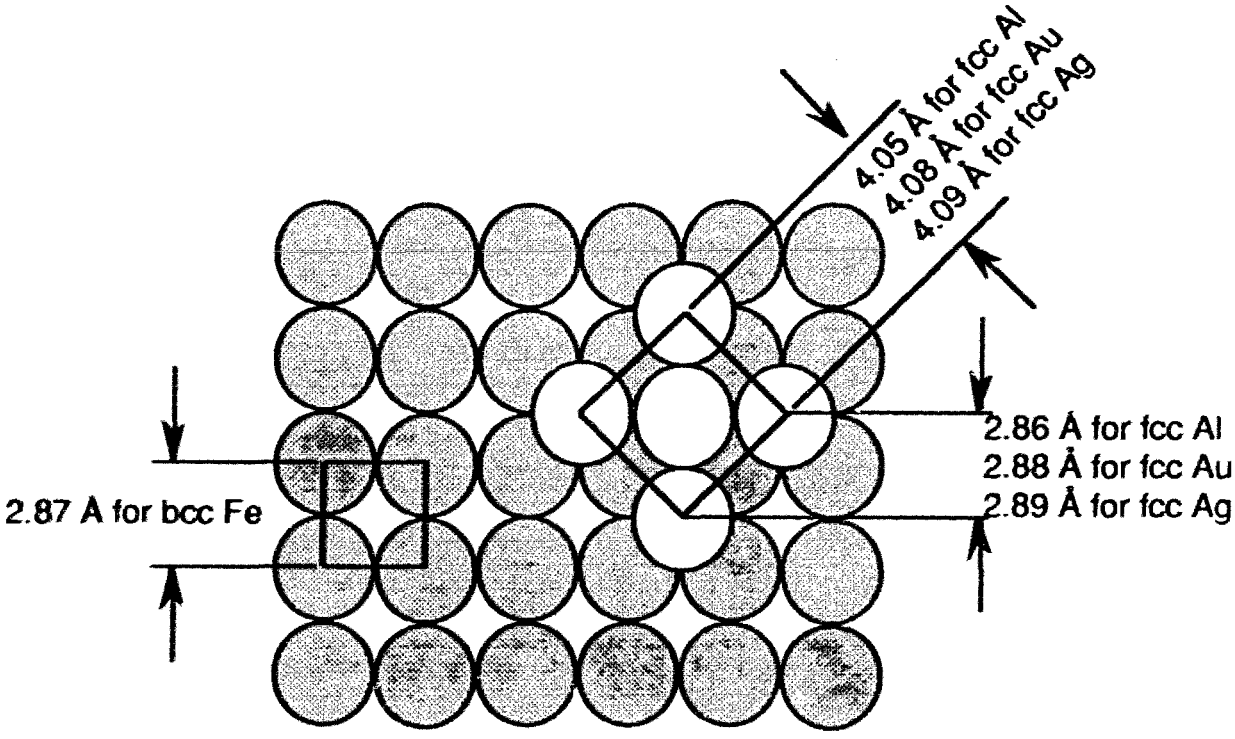

Fig. 3 Epitaxial matching of a (001) fcc overlayer on a (001) bcc structure.

In spite of the fact that the (001) plane of the natural phase of Ni, fcc, has a ~13% lattice misfit compared with the (001) plane of bcc Fe, it has been shown that a psudomorphic growth of Ni on Fe(001) can still be achieved for a film thickness less than 6 ML. This will also be demonstrated in the data presented in the following.

In the remainder of this section we present the data concerned with the sample growth for Ni/Fe(001) and Ni/Fe/Ag systems. The data were taken from the growths for samples used in glancing-incidence XAFS studies. More detailed summaries on the growth of the two systems has been provided in the literature.[11, 12]

3.1) Ni on bulk Fe(001)

The RHEED patterns of the Fe(001) substrates after the preparation in UHV are shown in Fig. 4. In Figs.4(b) and (d) those patterns not along the horizontal direction are termed as Kikuchi patterns. The Kikuchi patterns are formed in RHEED whenever the specimen is a reasonably flat single crystal with good lattice perfection.[13] They are caused by secondary scattering incoherent with the primary wave producing it. The well defined RHEED streaks and the the clear Kikuchi patterns indicate the high quality of the substrate surface.

Fig.5 shows the RHEED patterns of the above substrate with a 3 ML overlayer of Ni grown at room temperature. The oscillations shown in Fig.5(c) were monitored at the specular spot. Again, the sharp RHEED patterns and the Kikuchi lines indicate a good crystalline state of the overlayer. Comparing the RHEED patterns in Fig.5 with those in Fig.4 we can see that they are the same along the two orientations in terms of the features and the reciprocal spacings. This was true in other orientations as well. This fact was used by Heinrich *et al.* to point out first that Ni can grow pseudomorphically on the Fe(001) surface,[14] which was then supported by a quantitative LEED analysis by Wang *et al.*.[15]

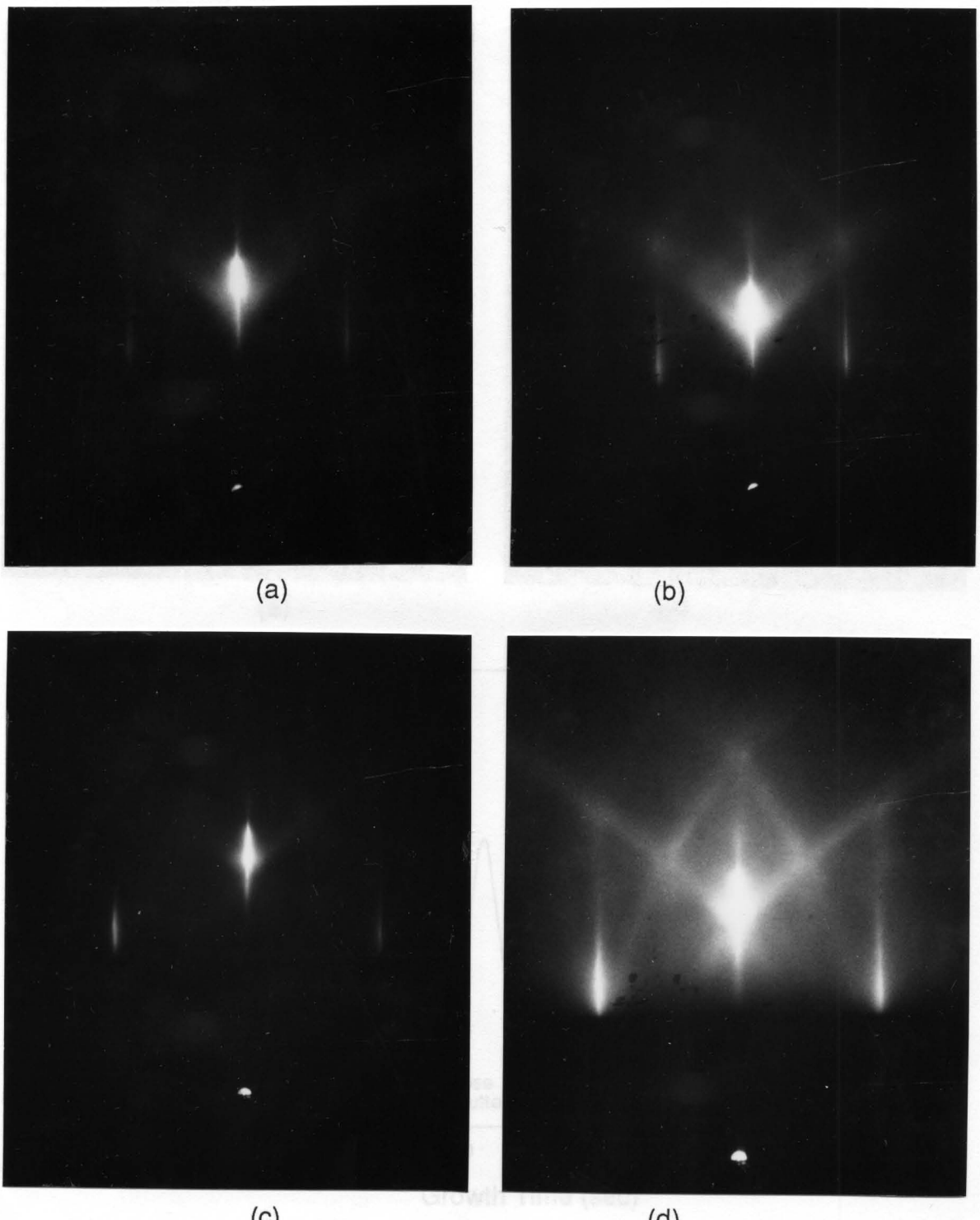

Fig.4. RHEED patterns. Figs. (a) and (c) show [100] and [110] RHEED patterns respectively from substrate Fe(001) A; (b),(d) are at the same orientations as (a), (c) respectively but overexposed to reveal the Kikuchi lines. The small spot on the left is the image of the direct beam.

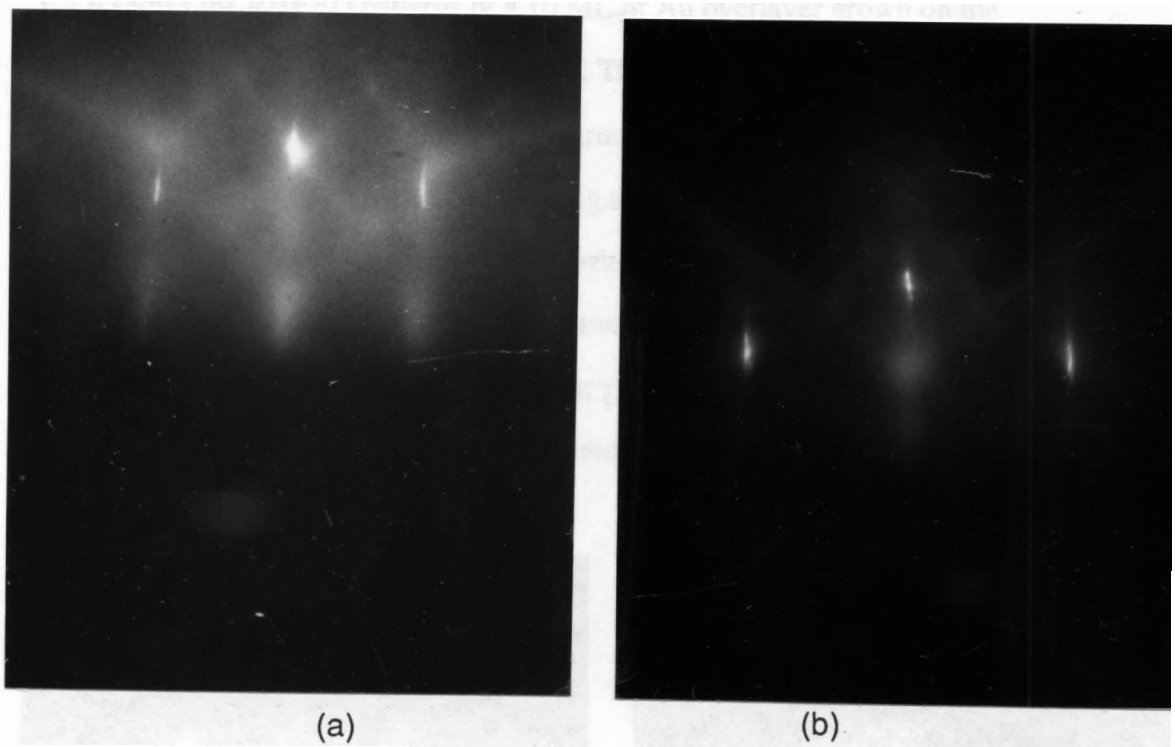

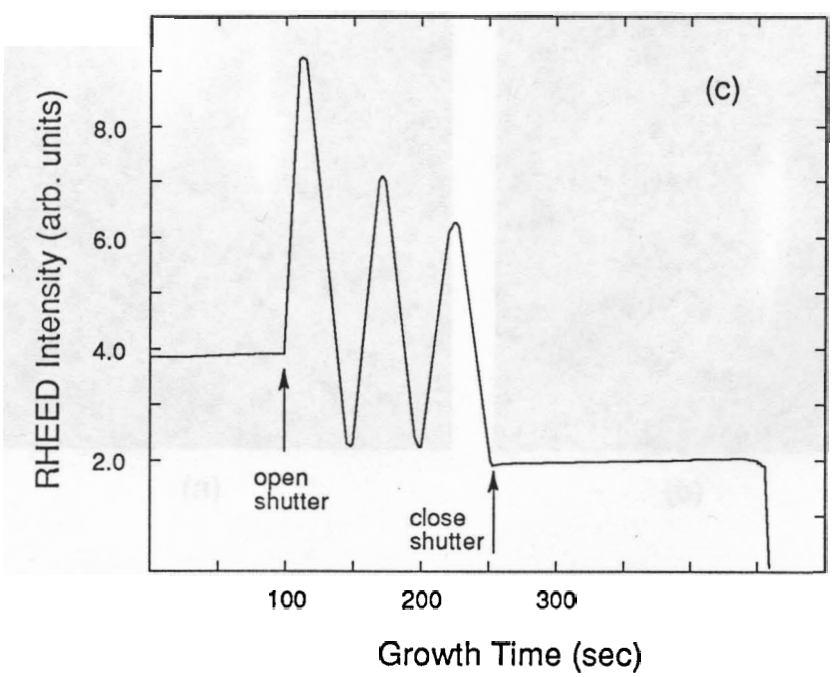

Fig. 5. RHEED patterns and intensity oscillations of 3 ML Ni grown on Fe(001) A at room temperature. (a) and (b) are [100] and [110] azimuths of Fe(001) respectively. (c) shows the intensity oscillations at the specular spot.

Au can be nicely grown on either bcc or phase transformed Ni/Fe(001) samples. Fig.6 shows the RHEED patterns of a 10 ML of Au overlayer grown on the Ni(3ML)/Fe(001) structure shown in Fig.5. This represents a typical case of the layer-by-layer growth of Au on all the Ni/Fe(001) structures discussed in this work . The Au(001) overlayers undergo a complicated reordering during growth that results in a unit cell containing 25 Au atoms.[16] Along [100] azimuth (of Fe(001) substrate) reconstruction is manifested by 4 additional weak streaks between the main RHEED streaks (only two of the weak streaks were resolved in the particular growth shown in Fig.6(b)) and along the [110] azimuth (of Fe(001) substrate) fans are developed that radiate from the main streaks.

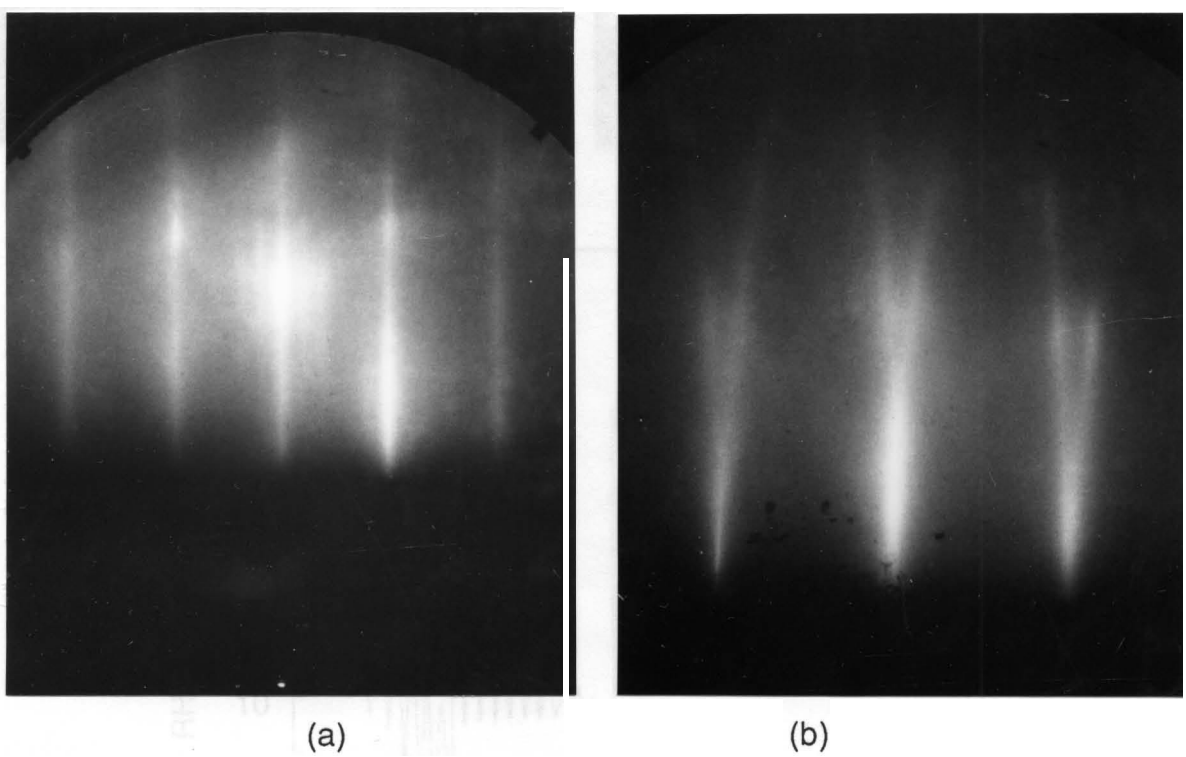

Fig. 6. RHEED patterns for a 10 ML Au overlayer on Ni(3ML)/Fe(001) A along [100] and [110] azimuths are shown in (a) and (b) respectively.

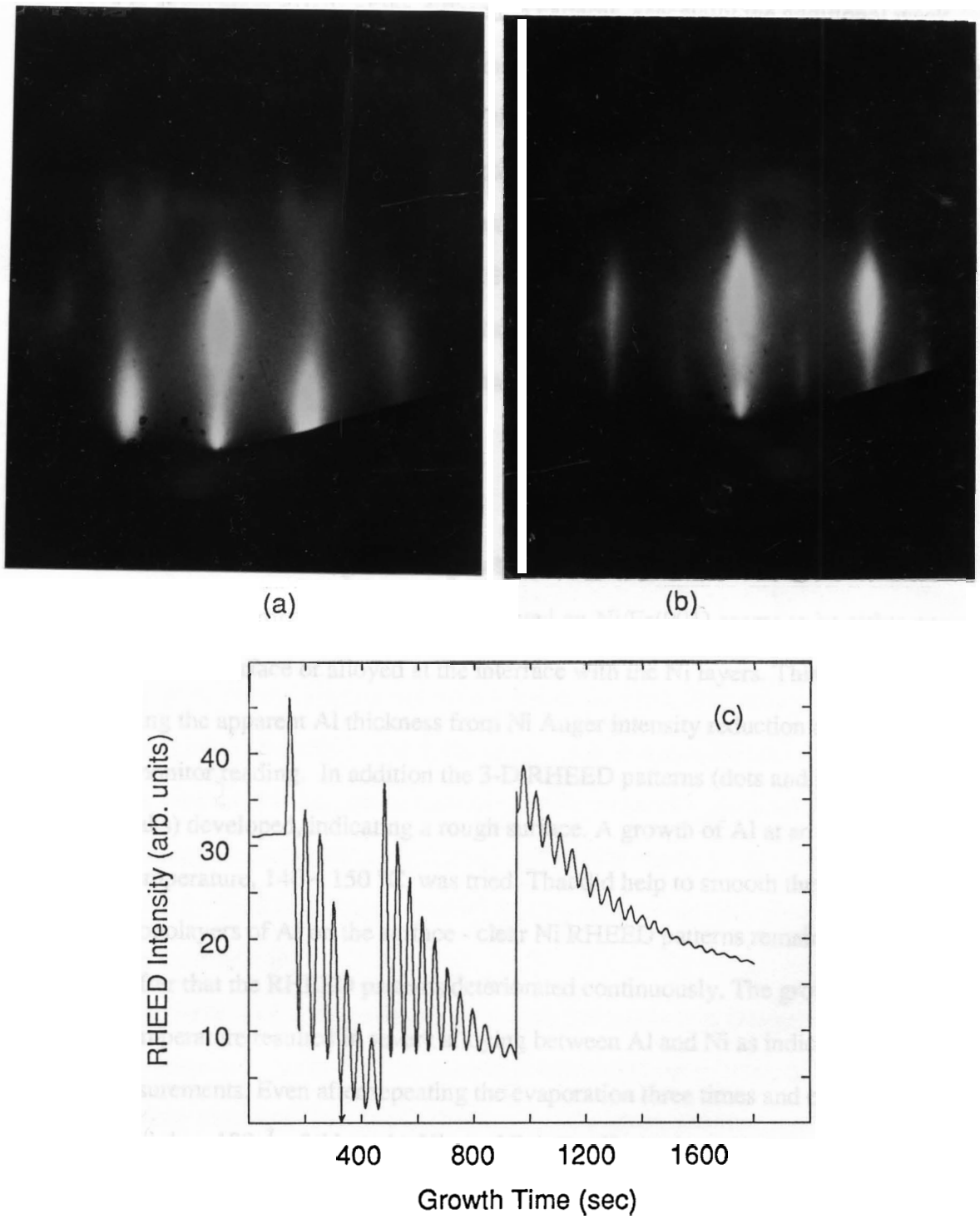

Fig.7 RHEED patterns and intensity oscillations of a 37 ML Ni overlayer grown on Fe(001) C at room temperature. (a) and (b) are along [100] and [110] azimuths of Fe(001) respectively. (c) shows the oscillations, the vertical mark line indicates the time when the reconstruction RHEED streaks first appear.

Fig.7 shows a growth of 37 ML of Ni on substrate Fe(001) C. The photos were over exposed to show more details of the diffraction patterns, especially the additional weak streaks in between the main bcc features along the [110] azimuth of Fe(001) (see Fig.7(b)). These weak streaks were the indications of the first phase transition which appeared right after the growth of 4 ML in this particular case (see the mark line in Fig.7 (c)). The large background intensity changes in Fig. 7(c) are due to the gain increases of the plotter (the data were digitized from the original trace). Notice that along the [100] azimuth, a fan structure, similar to that of Au overlayer discussed in Fig. 6, was also developed. There might be some underlying relationships between the two kinds of reconstructions.

3.2) Al Coverage on Ni/Fe(001)

Unlike the cases of using Au or Ag as the passive cover layer on top of the Ni overlayers, at room temperature the Al evaporated on Ni/Fe(001) seems to be either non-wetting on the Ni surface or alloyed at the interface with the Ni layers. This was determined by comparing the apparent Al thickness from Ni Auger intensity reduction and from the thickness monitor reading. In addition the 3-D RHEED patterns (dots and rings instead of surface steaks) developed, indicating a rough surface. A growth of Al at an elevated substrate temperature, 140 ~ 150 °C, was tried. That did help to smooth the surface in the first few monolayers of Al on the surface - clear Ni RHEED patterns remained up to about 11 Å, but after that the RHEED patterns deteriorated continuously. The growth at this substrate temperature resulted in severe alloying between Al and Ni as indicated by the Auger measurements. Even after repeating the evaporation three times and evaporating a total of more than 100 Å of Al on the Ni, the Ni Auger lines were still strong. At this point there couldn't be any area remaining exposed and thus the Auger result clearly indicated an alloyed situation. At a low substrate temperature of about -140°C (with fluctuations of a few degrees during the growth), the Auger measurements indicated a uniform coverage. At

this substrate temperature, the RHEED patterns quickly turned into a uniformed bright background after about an amount equivalent to 2 ML of Al was evaporated on the surface, i.e. the surface had an amorphous Al layer. When more Al was evaporated, around a thickness of 30 ~ 40 Å, some signs of recrystalization were shown in the RHEED patterns: there were some vague streaks or spots which appeared. When the thickness of Al got bigger the RHEED features became stronger (see Fig. 8). After the evaporation of Al was finished, the sample temperature was slowly brought up to room temperature. During the process the uniformity of the Al coverage was continuously monitored by Auger scans and no increase of the Ni Auger signal was observed. Even so, one sample with the layer composition Al(64Å)/Ni(6ML)/Fe(001) ,was found to have substantial alloying between Al and Ni from the XAFS measurements.[17] The alloying happened presumably in the longer time annealing at room temperatures. Therefore in the other Al covered samples of this work there could be a few monolayers of the Ni overlayers on the top of the Ni film contaminated by alloying with Al. But for the case of thicker Ni overlayers, e.g. 37 ML, the alloying at the interface seems not to be a serious problem. We will show in chapter V that a model ignoring the effect of alloying could result in reasonable fits for the EXAFS data and the results are in agreement with the sample prepared without Al coverage. In addition, as discussed later the magnetic properties of the samples were not substantially different from the ones with Au cover or no cover, which would unlikely be the case if the alloying were substantial.

It might have been unnecessary to go to such a low substrate temperature to have a uniform coverage of Al on Ni/Fe. One growth at a substrate temperature of –28°C indicated the surface may have been covered uniformly. But the lower substrate temperature should have reduced the interdifusion even more. The trade-off is that the resulting Al surface was very rough but that was not a major concern for our purposes.

The evaporation rate of Al was 1.3 -1.7 Å/min which was the same for all the Al growths.

Fig. 8. The RHEED patterns after 71.7 Å Al evaporated on Ni(37ML)/Fe(001) C.

To make sure that the Ni overlayers covered with Al had the same phase as those covered with Au or no coverage, ferromagnetic resonance (FMR) measurements were made on some of the Al/Ni(37 ML)/Fe(001) samples. The FMR measurements were carried out at atmospheric pressure. One of the testing samples (not measured by XAFS) was measured by FMR right after the growth and one week later to confirm that the phase lasts a sufficient time for XAFS measurements to be carried out. Another sample which was used in the XAFS experiments (Al/Ni/Fe Sample #2 in chapter V) had its FMR measured after the XAFS experiments. All of the FMR results confirmed that the Ni overlayers have similar magnetic behavior to the Ni not covered with Al and that the magnetic property is preserved during the XAFS data acquisition. **[11, 18]**

3.3) Ni on Fe on Bulk Ag(001)

Fig. 9 shows the RHEED intensity oscillations monitored during one of the two growths of 10 ML of Au on 9 ML of Ni on 9 ML of Fe on a singular bulk Ag(001) substrate. The well defined oscillations indicate that the growths of all the three elements were in a layer-by-layer fashion. Part of the curves in Fig. 9(a) and (b) are dashes which were digitized from the original trace on a chart paper, because the computer was not turned on in time to record the starting part.

3.4) Cu on Ag(001)

Fig. 10 shows the RHEED intensity oscillations of Au(10ML) on Cu(8ML) on Ag(001). The misfit between fcc Cu and fcc Ag is 11.7%. This growth is somewhat similar to that of Ni on Fe. RHEED patterns of the Cu indicate that the structure of the overlayers is close to bcc for thicknesses less than 10-11 ML. After that the structure transforms into a reconstructed phase but with additional RHEED features different from that of Ni. The XAFS results of this system are presented in chapter VI which shows the structure of the Cu overlayers to have a bct structure with the c axis expanded by about 8%.

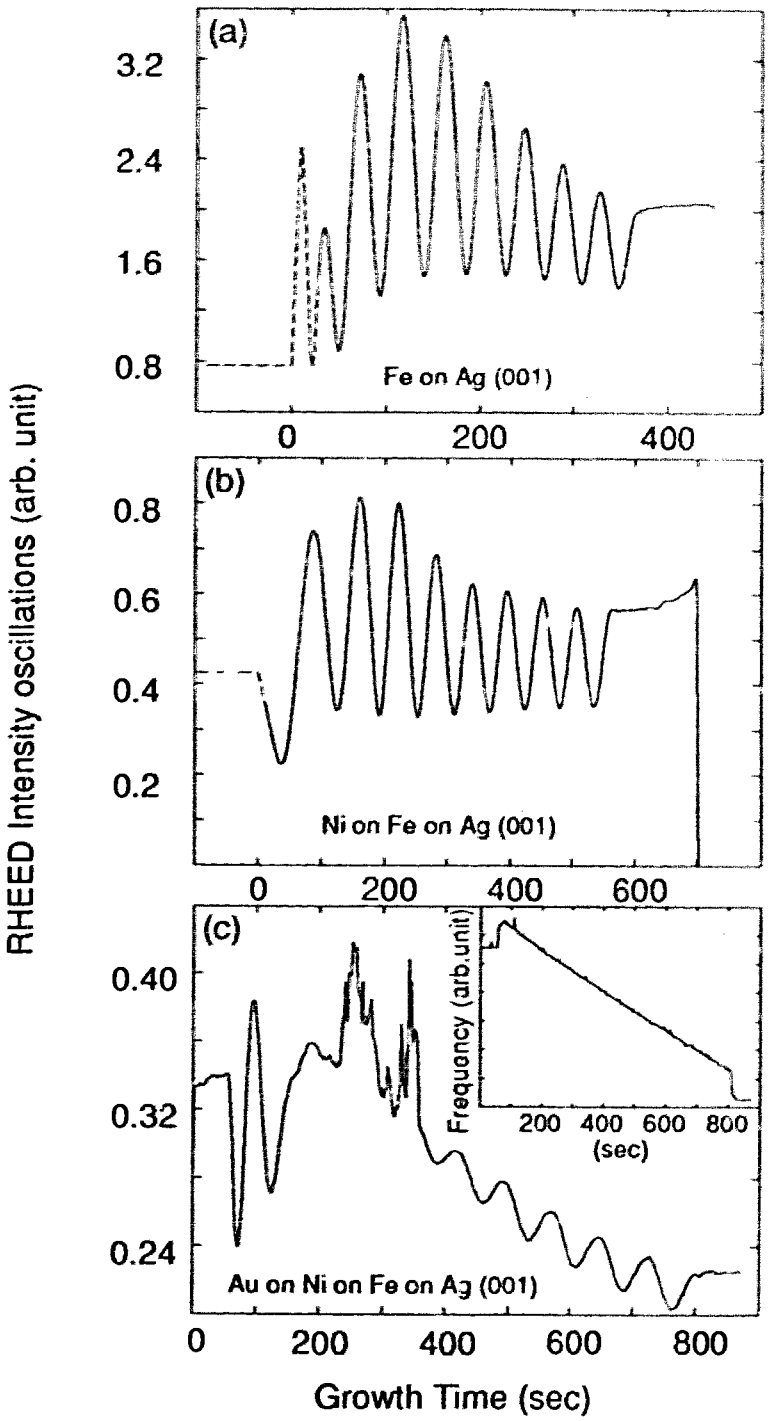

Fig.9 RHEED intensity oscillations in the growth of Au(10ML)/Ni(9ML)/Fe(9ML)/Ag(001): (a) the growth of Fe; (b) the growth of Ni; (c) the growth of Au. The noise structure between 230 sec to 360 sec was due to an electronic error and the number of periods during the time was deduced from the periods of the later oscillations. The inset of (c) shows the signal monitored by the thickness monitor and indicates that in the region concerned the curve is flat as expected.

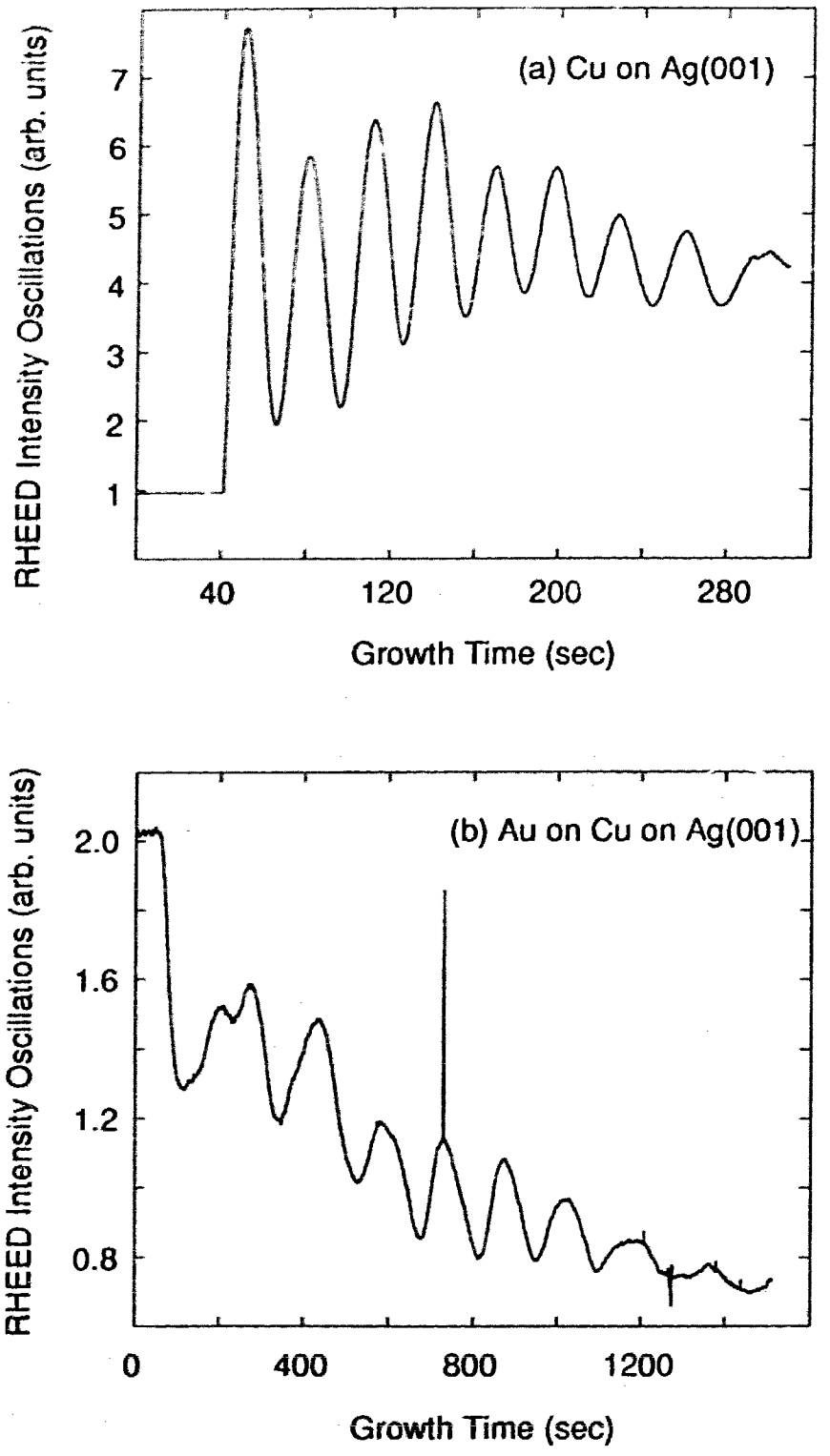

Fig. 10 Specular spot RHEED intensity oscillations of Au(10ML)/Cu(8ML)/Ag(001). (a) Cu on Ag, (b) Au on Cu/Ag.

Chapter V Data analysis and Results on Ni/Fe(001)

V.1) Introduction to Ni/Fe(001) System

Ni grows epitaxially on a Fe(001) surface. The initial structural studies on the Ni overlayers were done by Heinrich *et al.* using RHEED and it was concluded there could be a bcc Ni phase on Fe(001) for thicknesses above 20 ML.[1] Later LEED studies on the same system by Jona and colleagues [2, 3]showed that the pure bcc Ni phase with lattice constants of bcc Fe exits for thicknesses less than 6 ML and above that there is a gradual change to a new surface and bulk structure with a c(2x2) surface pattern. When the Ni thickness reaches about 13 ML, the LEED spectra is stabilized. The stabilized spectra seem to last beyond at least 100 ML of Ni overlayers. The first phase transition around 6 ML of Ni was confirmed by further refined RHEED studies and now it is generally accepted that the structure of Ni overlayers transforms away from pure bcc when the thickness exceeds 3 - 6 ML, with the onset of the transformation varying from growth to growth.[4,5] The structure-transformed Ni overlayers possess large in-plane 4^{th} order anisotropies far surpassing those observed in bulk Fe and Ni.[6]

The attempts to decipher the structure of the transformed Ni overlayers by Jona and coworkers using LEED was not successful.[2] The LEED results indicated that neither bcc nor fcc models nor a simple mixture of the two models could provide a satisfactory interpretation of the spectra. It was also pointed out that the structure is accompanied to some extent by disorder as indicated by the high background of the LEED intensity spectra. RHEED studies[5] on the transformed Ni showed that there are additional diffraction streaks in the RHEED patterns along [110] azimuths but the bcc streaks remain along the [100] and [110] principal azimuths all the way through the growth of the thicker Ni overlayers (e.g. in 37 ML in the case to be discussed below and also see the RHEED patterns shown in Fig. 7 in chapter IV). The additional superlattice streaks are also visible

for azimuths away from the [100] and [110] directions. However, it is not clear from the RHEED patterns alone whether the extra features reflect a mild reconstruction of the bcc Ni lattice or, in fact , represent major structural changes. That is why the structure has been referred to in the literature as bcc Ni with quotation marks.[6, 7] A local structure probe, REELFS, was also used to study the transformed Ni phase with an approximate thickness of 30 ML[7]. Within the experimental error (0.05 Å) the nearest neighbor distance in the Ni overlayers was found to be identical to that of ordinary fcc Ni (which is also very nearly the same as the nearest neighbor distance of bcc Fe). Although not commented on in the paper, the Fourier transform of the Ni overlayers is actually more similar to fcc Ni than to bcc Fe (see Fig.8 in Ref.[7]). But one should be cautious in interpreting the meaning of the Fourier transforms obtained in REELFS, because even on the standard sample (e.g. bcc Fe) the Fourier transform does not look the same as that obtained from EXAFS which comparatively is a more sophisticated technique.

In this chapter we present our glancing-incidence XAFS results for the Ni overlayers on Fe(001). First we study the stabilized structure of the Ni overlayers (37 ML) then we probe the local structure of a 9 ML thickness which is midway between the beginning of the gradual transition at the first 3-6 ML and the stabilized thickness of 13 ML. The description of data analysis is included in the chapter. A summary and discussion follow each section. In the last part of this chapter the efforts trying to probe the pure bcc Ni (<6ML) are described. In this chapter all the data for Ni were taken at the Ni K-edge and all the data for Fe were taken at the Fe K-edge.

V.2) 37 ML Ni/Fe(001)---The Stabilized Phase

We have prepared two types of samples in this stabilized structure, one with Al as the top cover material to prevent oxidation and the other without the cover layer above Ni but with the sample kept in a N_2 environment . The Ni thickness in the first case was 37 ML

and in the second case the thickness was about 50 Å as monitored by the quartz thickness monitor in the MBE machine.

One of the 37 ML samples was investigated outside the MBE chamber by Ferromagnetic Resonance (FMR) after the XAFS measurements. The FMR results confirmed that the Ni in the Al-covered Ni(37ML)/Fe(001) sample has similar magnetic behavior to the Ni of similar thickness (60 Å) but covered with 20 Å of Au. The time lapse between the two FMR measurements was to confirm that the magnetic property is preserved during the EXAFS data acquisition.

The Ni/Fe(001) sample without a cover layer was transferred from the MBE chamber to a Plexiglas chamber while N_2 gas was circulated and then the plastic chamber was sealed to keep the sample in the N_2 environment. The plastic chamber was later mounted on the rotation stage on the sample positioner to carry out the XAFS experiment. Undoubtedly the sample surface is contaminated with some O, C and etc. But careful analysis shows that actually the contaminated layer is less serious than we first thought . The rotation stage used in that experiment had a large wobbling angle, about 1 mrad. That causes a problem in the background subtraction in extracting the EXAFS function $\chi(k)$. If we use only the data taken when the sample was stationary, although it is limited in range due to Bragg peaks, we get agreement between the results on the no coverage sample and that of the Al-covered sample.

The 37 ML Ni experiment was repeated 3 times using a freshly prepared sample each time and different detector and positioner designs. During the process the experimental apparatus and methods were continuously improved (Chapter III).

In what follows we will present the results in a step by step fashion to show the different aspects of the XAFS data for the 37 ML Ni, and the methods of data analysis are described in detail. In our case we have several factors which do not appear in the standard transmission mode and require some extra caution in the data reduction: i) the Bragg peaks from the crystal sample usually limit the energy-space data range which then limits the final

R-space resolution; ii) the anomalous dispersion of x-rays accompanying the glancing-incidence will affect mainly the amplitude of the spectrum; and iii) as we will see that to distinguish different models for this system it is not enough to just get the first shell bond length right, we also have to analyze at least the second shell as well.

2.1) XANES of 37 ML Ni/Fe(001)

XANES refers to the features around the edge of the absorption spectrum $\mu(E)$. As we can see from the relation

$$\mu \propto |\langle f | \varepsilon r | i \rangle|^2 \rho(E) \qquad \text{(V-1)}$$

XANES is related both to the features in the density of states around the edge and the features in the dipole projector, so XANES can be sensitive to the electronic structure as well as to the bonding geometry.[8] For 3-d transition metals there have been detailed theoretical calculations based on the energy band structure approach. For example in the case of the K-edge of fcc Cu metal, the agreement between experimental results and theoretical calculation is very impressive.[9] Among different absorption edges of the transition metals, the K-edge shows a strong systematic dependence on the crystal structure. In the case of L-edges (except L_1) white lines, associated with atomic-like transitions, may outweigh the subtle dependence on the crystal structure.[9] In some cases the characteristic features in XANES which are related to bcc, fcc or hcp may be used as fingerprints for structural identification. But this cannot always be taken for granted, an example would be the 9 ML Ni of Fe(001) to be discussed later which has its XANES quite similar to that of bcc Fe but its EXAFS indicates the structure is definitely something else.

2.1.1) Experimental Estimation of the Anomalous Dispersion Effects in XANES

As discussed in Chapter II, in the glancing-incidence mode if the entire signal is detected then the XANES contains larger distortion compared to the distortion in the EXAFS. To assess the degree of this distortion in our data, the XANES from the total-electron-yield at incident angles ranging below and slightly above the critical angle are plotted in Fig.1. The effective critical angle used here, ϕ_c, was defined to be the angle where the reflectivity for a 8033 eV x-ray beam was reduced to 50% from its maximum value. From Fig.1(a) it can be seen that, although there are some differences between the curves, basically they all have a shoulder right above the inflection point and then two peaks following that. A close look at the first 20 eV of the spectra reveals a systematic change in the lineshape, which is demonstrated in Fig.1(b). At very small incident angles, say the bottom two curves in Fig.1(a), the distortion of the anomalous dispersion is the lightest, presumably it is closer to the undistorted XANES of the 37 ML of Ni if we ignore the possibility that at these angles the signal from the Al/Ni interface is heavily weighted. Similar trends also exist in XANES obtained from fluorescence and reflectivity. Their somewhat worse signal-to-noise ratio thwarts the comparison over as large φ range as shown for the case of total-electron-yield. From Fig.1 we also see that the distortion is not severe enough to obscure the basic structure of the XANES of 37 ML of Ni, i.e., the shoulder above the inflection point followed by two peaks in the energy range selected. This fact facilitates the following qualitative comparison with the XANES of known structures.

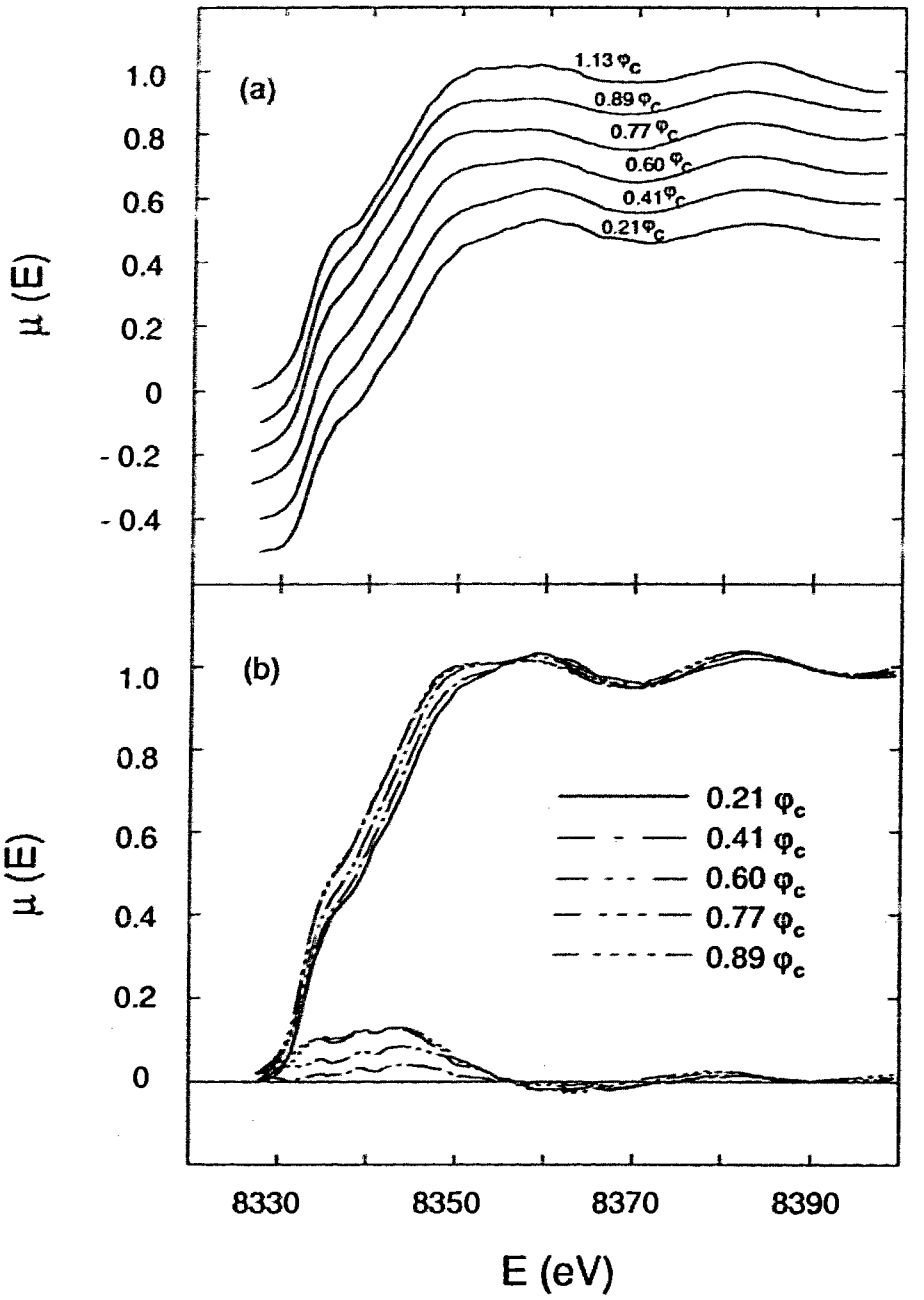

Fig. 1. XANES of the 37 ML Ni film at different x-ray incident angles. (a) The curves are shifted for clarity (the bottom one is slightly smoothed). The trend of distortion of the shape of the first peak can be seen. (b) The curves are plotted on the same scale (the highest angle curve is not shown for clarity). At the bottom the differences between the lowest φ curve and others are shown to indicate the amount of distortion in each case.

2.1.2) Comparison with bcc Fe and fcc Ni

Figure 2 shows the comparison between the XANES of the 37 ML Ni and that of two reference samples, fcc Ni and bcc Fe. The reference data were obtained from metal foils in transmission mode. The origin of the energy scale is defined to be at the inflection point in each curve. Large differences between bcc Fe and the 37 ML Ni can be seen: in the high energy part of the spectra the peak positions are different and between 10 to 30 eV the lineshapes are very different. To some extent the 37 ML Ni resembles fcc Ni in the sense of the peak positions, but on the other hand the difference is also obvious: the double peaks between 10 to 30 eV in fcc are not resolvable in the 37 ML Ni. These comparisons can be seen more clearly in the derivative plots shown in Fig.2(b). The differences between the 37 ML Ni and bcc or fcc are not due to the residual anomalous dispersion effects in the 37 ML Ni data. First of all, the distortion is negligible in the high energy range as shown in Fig.1(b). Secondly, the trend of reducing the distortion as shown in Fig.1(a) goes in the direction to make the undistorted XANES of the 37 ML Ni differ even more from bcc Fe, and thirdly due to the monotonic nature of the distortion above the edge it is impossible to eliminate from the 37 ML XANES the double-peak structure which is present in fcc Ni.

The data shown in Fig. 2 were taken during different experimental runs at Beamline IV-1 at SSRL using different monochromator crystals. The Fe and fcc Ni spectra were taken using Si(220) and the 37 ML Ni spectrum was taken using Si(111). The difference between the 37 ML Ni and fcc Ni cannot be due to the different energy resolution of different crystals, because first the difference is too large and second the same Si(220) monochromator crystal was used in one run to take the fcc Ni reference and a 37 ML Ni data set and the latter is indistinguishable from what was taken by Si(111) monochromator crystals. Based on these observations we can see that the 37 ML Ni does have a XANES

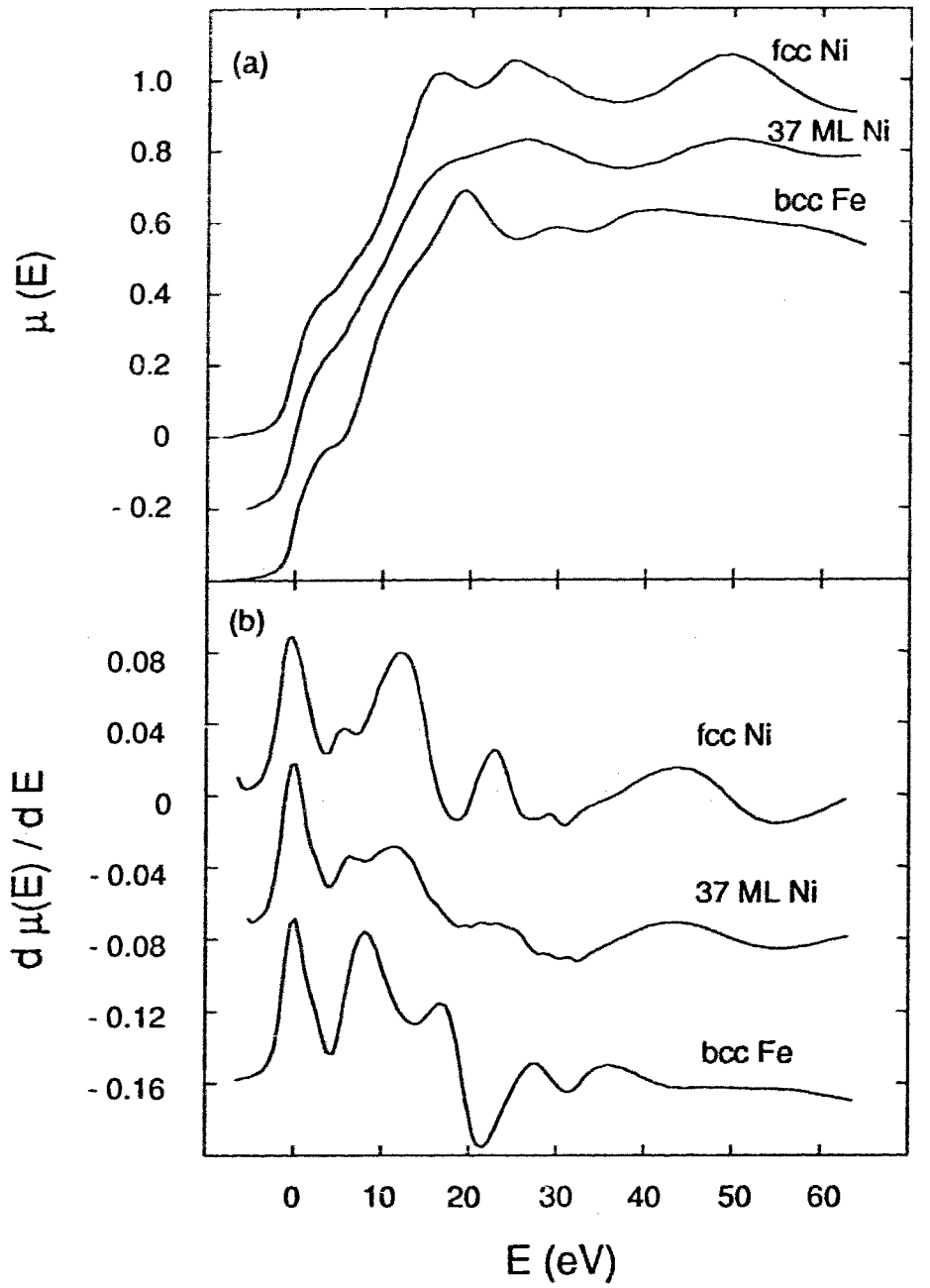

Fig. 2. Comparison of XANES of 37 ML Ni with that of fcc Ni and bcc Fe. The 37 ML Ni data were acquired in the total electron-yield mode at $\varphi = 0.41\varphi_c$.

that is different from either fcc Ni or bcc Fe, but is relatively closer to fcc Ni. In other words, the XANES of the 37 ML Ni identifies that it is a new phase different from normal fcc Ni metal and at the same time it does not look like a bcc structure at all. It remains to be seen in the EXAFS analysis later whether this trend in XANES comparison correlates an atomic structure difference in this new phase of Ni metal compared to its natural phase.

2.2) Qualitative Analysis of the EXAFS of 37 ML Ni/Fe(001)

2.2.1) Comparison of $\chi(k)$

In Fig.3 the EXAFS data of the 37 ML Ni is compared to that of fcc Ni and bcc Fe. Fig.3(a) shows what is usually referred to as raw data and in Fig.3 (b) we have the EXAFS interference function $\chi^{expt}(k)$ which was obtained from (a). The pre-edge background was removed by a linear least-squares fit for the 37 ML Ni (data obtained in fluorescence mode) and by a Victoreen function fit in the other two cases (data obtained in transmission mode). To get $\chi^{expt}(k)$, the background above the absorption edge was removed by the a 7^{th} order polynomial function for the reference data and by 200 passes of a 3-point smooth function[10] for the Ni overlayers, and then the amplitude was normalized by the edge jump. The edge jump height we used here was determined by extrapolation of a linear least-squares fit in a range of about 300 to 600 eV above the edge and the value of the jump height is defined as the value on the straight line at the first inflection point. The anomalous dispersion effect not only changes the amplitude through the multiplicative function $Amp(k)$ (see Chapter II.3.1), it also generates a curvature background above the edge as well (e.g. see Chapter II Fig.10(d)). When the sample layer is thick, such as the case in hand, the background distortion causes difficulties in accurate determination of the jump height hence large errors in absolute coordination determination. This is one of the major limitations of the glancing-incidence EXAFS. With the range of the linear fits to be extrapolated farther towards the high energy end, the effect of the distortion

is reduced. On a transmission data set like the one for fcc Ni, the different linear fitting range yields a variation in the jump height less than 5%.

From Fig.3 we see that the spectrum of the 37 ML Ni has almost every peak aligned with that of fcc Ni except in the vicinity of the edge. In contrast, the difference between the Ni overlayers and bcc Fe is obvious, especially in the range from 4 to 6 $Å^{-1}$.

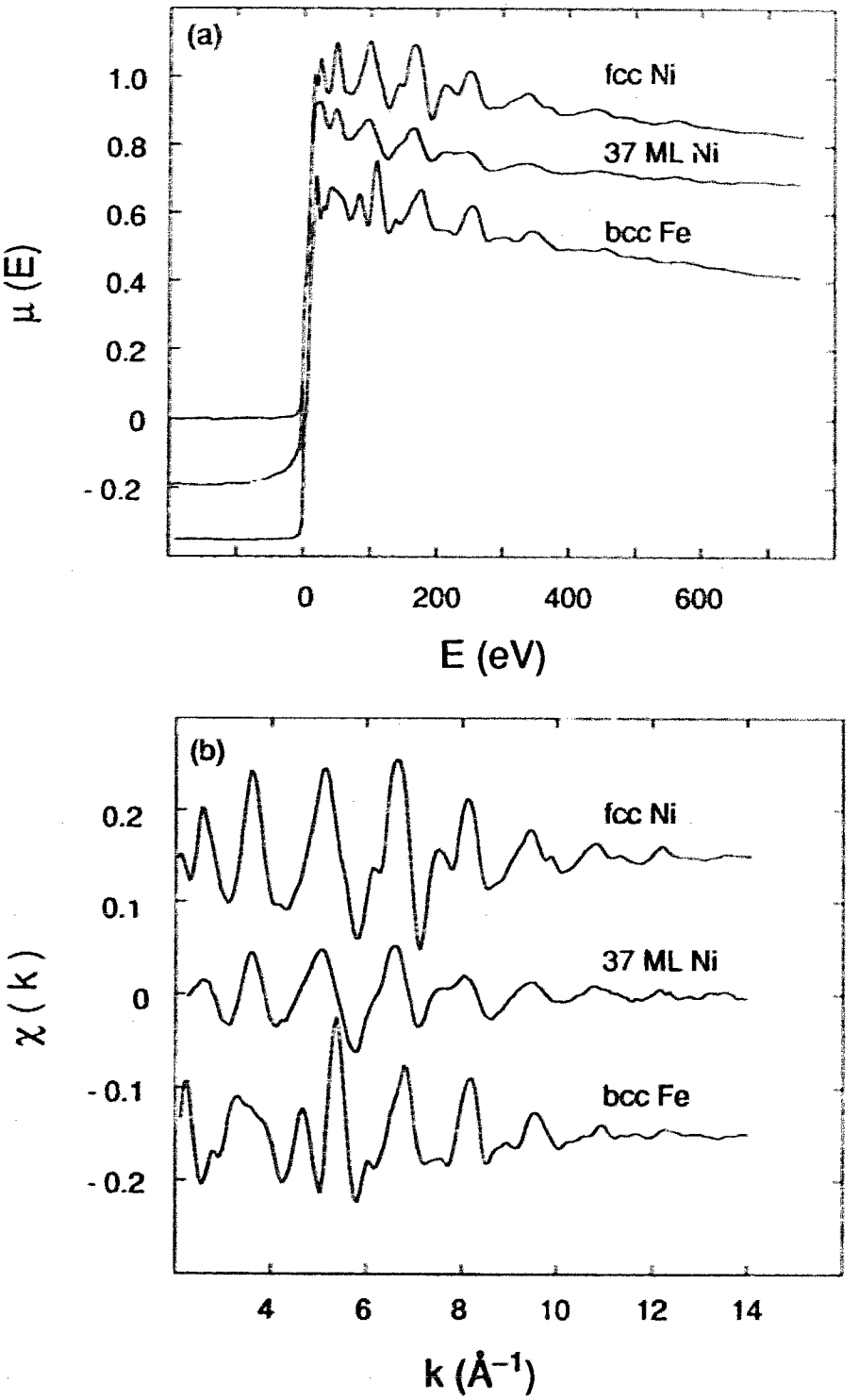

Fig. 3. Comparison of EXAFS data. (a) Comparison of raw data. The origin of energy scale is defined to be at the first inflection point of each curve; the height of the curves are scaled in proportion for the comparison. (b) EXAFS interference functions for the 37 ML Ni sample and the two reference samples, where $k = [\ 2m_e\ (E - E_o\ )]^{1/2}/\hbar$ with E_o being the energy at the first inflection point.

2.2.2) Comparison of the Fourier Transforms

For the sample layer thickness under consideration, as discussed in chapter II.3.1 a significant difference between $\chi^{expt}(k)$ and $\chi(k)$ occurs only in the amplitude. We will see that the final reliable results we get from the data are not concerned with the absolute amplitude, so from this point on we will treat $\chi^{expt}(k)$ as if it were not modulated by the other factors and address the effects whenever they are relevant relevant.

The $\chi(k)$ functions in Fig.3(b) were multiplied by wave number k and then Fourier transformed from energy-space (actually k-space) into the real space ($\tilde{R}$-space) and the results are shown in Fig. 4. The Fourier transform was carried out by using the Fast Fourier Transform algorithm (FFT).[11] The origin of the transform in R-space corresponds to the position of the absorbing atom and the peaks in the magnitude of the Fourier transform are caused by separated atomic shells surrounding the absorbing atom. It is easy to visualize this if we notice that $k\chi(k)$ consists of a sum of sine functions with each term multiplied by an amplitude modulation function (see formulae II-3), so the Fourier transform should simply be a set of δ-functions broadened by the convolution with the transforms of the amplitude functions. Assuming the radial distribution of the shells is Gaussian, it can be shown that the peaks in the magnitude indeed correspond to different coordination shells, but the bond length judged from the peaks is shifted by the electron scattering phase.[12] The peak height is proportional to the coordination number at the shell and the EXAFS Debye-Waller term in (II-3). It is also strongly dependent upon the finite range of the k-space data that is transformed. Although the more distant shells usually have a larger coordination they have a smaller magnitude because of the Debye-Waller reduction factor and the phenomenalogical mean-free-path term (see II-3).

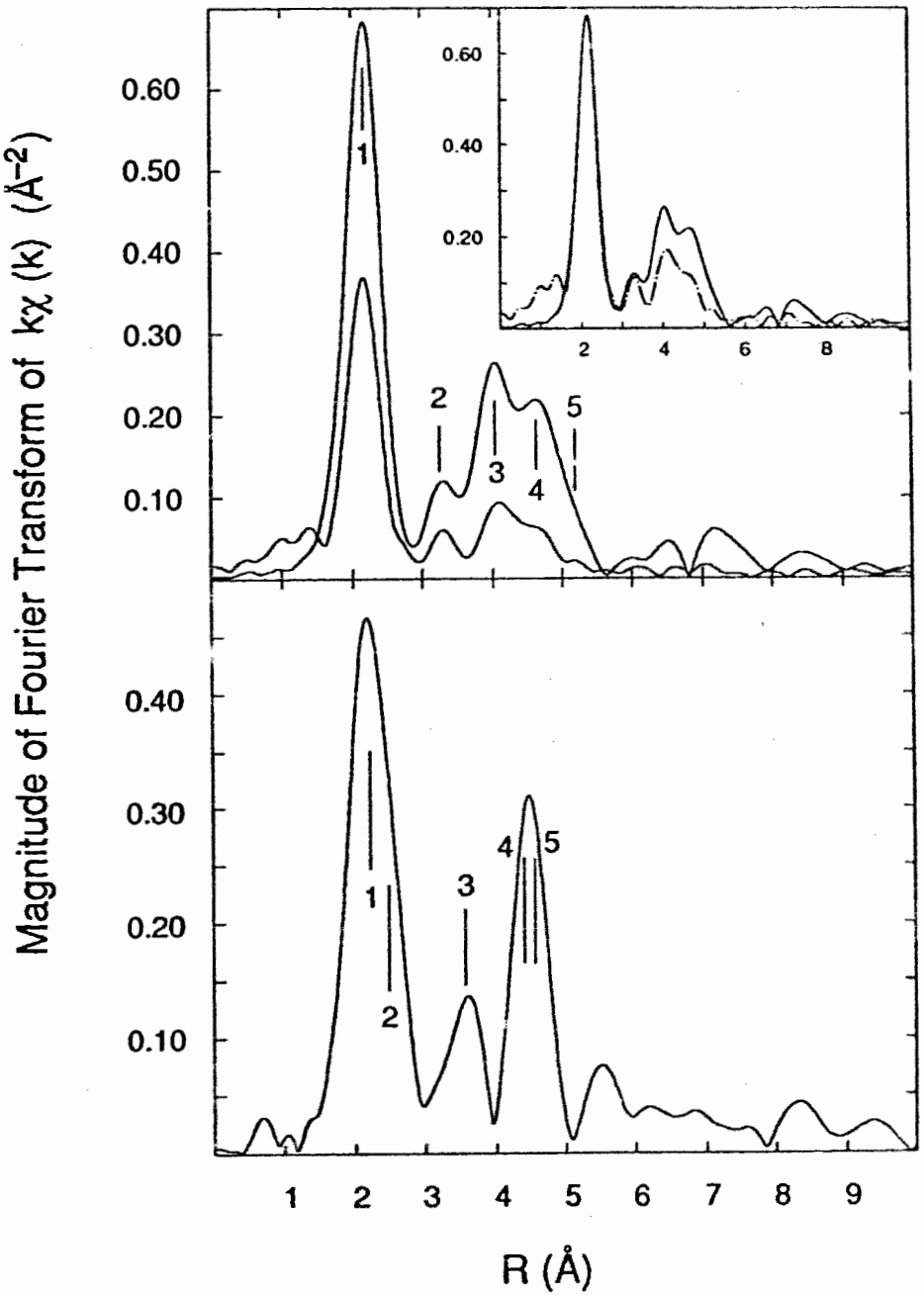

Figure 4. Magnitudes of the Fourier transform of $k\chi(k)$ for 37 ML Ni, fcc Ni and bcc Fe. k-range from 2.87 to 14 $Å^{-1}$ and a 30% Gaussian window were used. The numbers indicate to which coordination shell the features correspond. (a) the higher curve is for fcc Ni and the lower one is for the 37 ML Ni; in the inset the Fourier transform of the 37 ML Ni was scaled by a constant to have the same height as that of fcc Ni at the first peak. (b) the curve for bcc Fe.

As can be expected from previous comparison in k space, the similarity (dissimilarity) between the 37 ML Ni and fcc Ni (bcc Fe) is obvious in Fig.4. This is even more clearly shown in the inset of Fig.4(a) where the first peak has been scaled to have the same height. In Fig.4 the short vertical lines and the numbers indicate approximately the positions of the neighboring atomic shells. It is apparent that if we assume in the R range from 1.5 to 3.5 Å the Ni overlayers also have two shells like fcc Ni then the bond lengths and ratio of the coordination of the first two shells in the 37 ML Ni would be almost identical to that of fcc Ni. However, above 3.5 Å we can see a large relative drop in the magnitude of the transform of the Ni overlayers compared to fcc Ni. In the Fourier transform of the bcc structure the peak in the range from 4 to 5 Å is very characteristic. In this range the transform of the bcc Fe is determined by the fourth and fifth nearest neighbors. The fifth nearest neighbor is on the body-center diagonal site; focused multiple scattering causes the contribution to the $\chi(k)$ to be extraordinarily high. From the curve for the 37 ML Ni we do not see the indication of the existence of such an unusually strong peak in the higher R range. On the contrary, the peak number and relative magnitude in the high R range are very similar to that of fcc Ni, in spite of the large drop in magnitude compared to the fcc curve.

The apparent overall difference in heights between the peaks of the 37 ML Ni and that of fcc Ni can be partially accounted for by the reduction caused by the anomalous dispersion effect. A model calculation for the angular and energy dependence of the amplitude reduction factor was carried out. The result shows that when $\varphi \rightarrow \varphi_c$ the amplitude will drop by about 40%. With this part of the magnitude included, the first peak of the Ni overlayers would be about the same height as that of bcc Fe, which is still much smaller than that of fcc Ni. So we see that although the shell positions and relative magnitudes of the transform of the 37 ML Ni are rather similar to that of fcc Ni, there seems to be a lot of empty nearest neighbor sites in the Ni overlayers. The significance of

this observation will be addressed again in later discussions about the modeling of the overall structure of the overlayers.

2.2.3) Beating Analysis

From the degree of the similarity between the two curves in Fig.4(a) it is very tempting to conclude directly that the 37 ML Ni has only two shells below 3.5 Å as in the case of fcc Ni. But we know for bcc Fe the first peak consists of two shells. However, because the first and second nearest neighbor shells are quite close together (ΔR = 0.385 Å) only a slight asymmetry occurs to manifest the existence of the second shell. Therefore it would be better to have something more than just an educated guess for the shell assignments for the Ni overlayers. One way to test if there is another shell in the first peak of the 37 ML Ni is to use the beating analysis.[13-15] This exercise might look a bit redundant in the 37 ML Ni case, but in the other cases to be discussed later in this chapter and next chapter this technique will play a more important role. For consistency, we first briefly describe the beating analysis technique then apply it to the 37 ML Ni data.

When two shells have the same atomic species, the EXAFS of the two shells can be written as

$$\chi(k) = \frac{1}{k}\tilde{A}(k)\sin\left[\,2k\tilde{R} + \tilde{\phi}(k)\,\right] \qquad \text{(V-2)}$$

where $\tilde{A}(k) = A_1(k)\left[\,1 + C(k)^2 + 2C(k)\cos(k\Delta R)\,\right]^{1/2}$

$$\tilde{\phi}(k) = \phi_1(k) + \tan^{-1}\left[-\frac{1-C(k)}{1+C(k)}\tan(k\Delta R)\right]$$

$A_1(k)$ and $\phi_1(k)$ are the effective backscattering amplitude and the central plus backscattering phase shift of shell 1, $\tilde{R} = \frac{(R_1 + R_2)}{2}$ is the mean bond length of the two shells, C(k) is the ratio of backscattering amplitude of shell 2 over shell 1,

and $\Delta R = R_2 - R_1$. Due to the interference of the two shells, minima appear in the total backscattering amplitude $\tilde{A}(k)$ and kinks occur in $\tilde{\phi}(k)$ with values of k at the beating nodes

$$k_{(2n+1)} \approx \frac{(2n+1)\pi}{2\Delta R}, \quad n = 0,1,2,... \tag{V-3}$$

One can use $\tilde{A}(k)$ or $\tilde{\phi}(k)$ to measure the values of $k_{(2n+1)}$ and thus deduce ΔR. In practice the kink position is located by taking the derivative of the phase with respect to k. The obvious advantage of this method over other analysis techniques is that knowledge of the backscattering amplitude and phase is not needed.

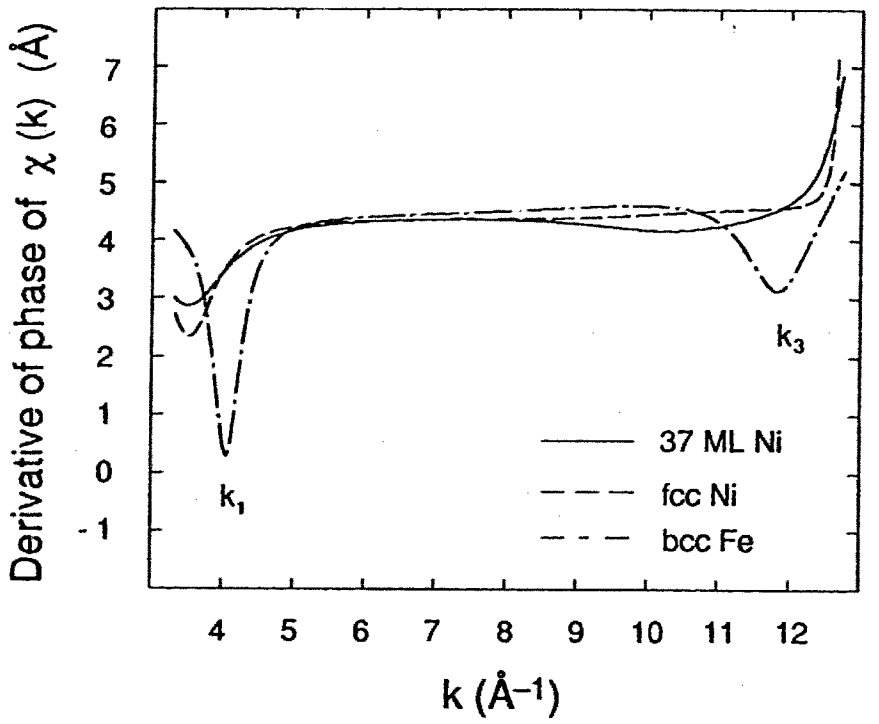

Figure 5 Derivatives of the EXAFS phase extracted from Fourier transform of $k\chi(k)$. A 10% Gaussian window was used with a k-space transform range:3.26 to 12.77Å^{-1}. The R-space filter range was 1.37 to 2.96Å. The first and the third beat nodes on the bcc Fe curve are indicated by k_1 and k_3.

Figure 5 shows a comparison of the phase derivatives.The three curves are processed in the same way. On the curve representing bcc Fe we can see clearly two beat nodes, one at about 4 $Å^{-1}$ and the other one at about 12 $Å^{-1}$. They are the first and the third order nodes respectively. The curvature around 3 $Å^{-1}$ of fcc Ni and the 37 ML Ni is not a beat node. This feature appears differently (e.g. disappears or changes into a peak) depending on the detail of the transform procedures such as window range and k weighting order, while real beat nodes are insensitive to different transforms. Actually if it were a node, we should be able to see the next order around 9 $Å^{-1}$ which is not the case. Plus, we know in the R-range considered there is only one shell for fcc Ni. The steep slope on the fcc Ni curve at the high k end is also a transform artifact.

The fact that there is no beat node on the 37 ML Ni curve tells us that the 37 ML Ni has a single shell in the first peak of the transform and the structure cannot be a purely bcc one. The structure could be a mix of fcc and bcc domains. However, one can add the $\chi(k)$ of bcc Fe and fcc Ni to simulate the data of a two phase system and apply the beating analysis to see the minimum percentage necessary to have a visible dip in the phase derivative. In this way it can be shown that a 20% bcc content would definitely make a distinguishable dip in the phase derivative. Later in the curve-fitting analysis this lower bound of residual bcc phase will be pushed much lower.

2.3) Quantitative analysis of the EXAFS of 37 ML Ni/Fe(001)

In this work we need to use both of the major kinds of EXAFS analysis techniques, i) the log-ratio and phase difference methods; ii) multiparameter-nonlinear-least-squares curve-fitting. Both of the analysis techniques have been extensively reviewed in the literature.[12, 16-18] In the following we just sketch the basic ideas of the methods and then present the results of the analysis.

2.3.1) Phase-difference and Log-ratio Method

This method is based on Fourier filtering. First the EXAFS $\chi(k)$ is Fourier transformed into R-space, then a part of the transformed data corresponding to a particular shell can be filtered and transformed back into k-space and hence the decomposed EXAFS amplitude and phase functions can be obtained. Then these amplitude and phase functions can be compared to the amplitude and phase of the reference which can be from either a reference material of known structure or results of *ab initio* calculations.

For a particular shell the EXAFS interference function can be written as

$$\chi(k) = A(k) \sin \Phi(k), \qquad \text{(V-4)}$$

where $\Phi(k) = 2kR + \phi(k)$ is the phase function of the shell. With a model compound (known structure, phase $\Phi_m(k)$ and amplitude $A_m(k)$) of the same element as that in the unknown structure, the difference in the phase functions is simply

$$\Phi(k') - \Phi_m(k) = 2k'R - 2kR_m + \phi(k') - \phi_m(k) \,. \qquad \text{(V-5)}$$

The difference in (V-5) is roughly a linear function of k. The k' and k designate that the reference and the unknown may have different Fermi levels hence the k scale origins could be different. The EXAFS assumption - the phase transferability - states that the EXAFS phase $\phi(k)$ is basically an atomic feature, not sensitive to the structure when the photoelectron energy is well above the Fermi level. Based on this assumption, once the origin of the k' is adjusted so that the atomic feature cancels out, i.e. $\phi(k) - \phi_m(k) = 0$, then from the slope of the linear curve $\Phi(k) - \Phi_m(k)$ vs k we can extract the bond length R.

For the amplitude function, we have

$$A(k) = \frac{N}{kR^2} \mid f(k) \mid S_o^2 \, e^{-2k^2\sigma^2} \, e^{-2R/\lambda}. \qquad \text{(V-6)}$$

Similar to the phase transferability, in cases that the atoms in the unknown structure and in the reference have very similar atomic environments the backscattering amplitude $\mid f(k) \mid$ in $A(k)$ should also be transferable. In practise, the validity of this assumption of amplitude transferability is much more restricted than the assumption of phase transferability.[19] Denoting the reference system by the subscript m, the logarithm of the amplitude ratio gives

$$\ln\left(\frac{A(k)}{A_m(k)}\right) = \ln\left(\frac{N\,R_m^2 S_o^2}{N_m\,R^2 S_{om}^2}\right) + 2k^2\,(\sigma_m^2 - \sigma^2) + 2\left(\frac{R_m}{\lambda_m} - \frac{R}{\lambda}\right). \qquad \text{(V-7)}$$

If it is further assumed that $\lambda \approx \lambda_m$, $S_o^2 \approx S_{om}^2$ and $(R_m - R) \ll \lambda$, the third term can be neglected and a plot of the log-ratio $\ln\,(A(k) / A_m(k))$ *vs* k^2 gives rise to a linear curve with an intercept of $\ln\left(\frac{N\,R_m^2}{N_m\,R^2}\right)$ and a slope of $2(\sigma_m^2 - \sigma^2)$. From known values the parameters N and σ^2 can be deduced.

2.3.2) Curve-fitting Methods

As can be seen from the above discussion the phase-difference and log-ratio methods are applicable only to cases where the shells are well separated in R-space and can be isolated by Fourier filtering. In cases where the system has closely coordinated two or more shells or where the R-space resolution is limited by the finite data interval in k-space, we would have to deal with at least two shells together. The common method in this situation is to use a parameterized function to fit the data and extract the structural parameters from the best fit.

The parameterized function used to fit the data in this work is the following

$$\chi(k) = \sum_j \frac{N_j}{k_j R_j^2} \mid f_j(k_j) \mid S_0^2 e^{-2k_j^2\sigma_j^2} e^{-2R_j/\lambda} \sin [2k_j R_j + \phi_j(k_j)] , \quad \text{(V-8)}$$

where the terms have the same meanings as in equation (II-3a) except k_j is related to k via the parameter ΔE_j (concerning the origin of the k_j scale) defined below

$$k_j = \sqrt{k^2 - \Delta E_j/\gamma} \ , \quad \text{(V-9)}$$

with $\gamma \equiv \frac{\hbar^2}{2m_e} \approx 3.81$ eV Å^2. k is the magnitude of the wave number of the photoelectron and is the k-scale of the measured EXAFS function, i.e. $k = [\ 2m_e\ (\hbar\omega - E_{inflection}\ )]^{1/2}/\hbar$. It is not modified in the curve-fitting. The effective backscattering amplitude $\mid f_j(k_j) \mid S_0^2 e^{-2k_j^2\sigma_j^2} e^{-2R_j/\lambda}$ and phase $\phi_j(k_j)$ in (V-8) used in later fittings for Ni overlayers are calculated using an *ab initio* single-scattering XAFS theory (FEFF code).[20]

In this work the fitting was always done in R-space. The quality of the fit was evaluated by minimizing a residual sum of squares χ^2 defined as the following [21, 22]

$$\chi^2 = \frac{n_{free}}{(n_{free} - n)} \frac{1}{N} \sum_{i=1}^{N} (Data_i - Fit_i)^2, \quad \text{(V-10)}$$

where $n_{free} = 1 + \Delta k\, \Delta R/\pi$ and n is the number of fit parameters. The uncertainty in a specific fitting parameter was determined by finding the deviation of the parameter from its best-fit value which doubles the residual sum of squares χ^2, meanwhile allowing all other $(n - 1)$ variables to float. The error bar defined in this way could be too conservative,[22] possibly by as much as a factor of 2.[21] The error bar so defined describes only the precision of the fit, the systematic errors need to be considered separately. In the form (V-8) the bond length R_j contains a small systematic deviation of $2\sigma_j^2(\frac{1}{R_j} + \frac{1}{\lambda})$ from the true

value (see section II.1). The correction in the current case is ~0.005 Å and it has been added in the values presented hereafter.

2.3.3) Results

One drawback of using the backscattering amplitudes and phases calculated from FEFF is that the code is not yet written in a way to handle two shells together. Our approach to this limitation was to use the amplitude and phase calculated for the first shell at 2.492 Å to fit the second shell at 3.524 Å. The difference in the phase due to the different curvature of the photoelectron at different distances was compensated by a E_o shift for the second shell relative to the first shell. To find this parameter and to have a starting point of other fitting parameters as close to that of the 37 ML Ni as possible, we first performed a fit on the data of fcc Ni for which we know the structure and which, from previous qualitative analysis, we know is very similar to the 37 ML Ni. The fit was done in two steps: first the nearest neighbor shell was fitted by a single shell fit process, then with all the parameters concerned with the first shell fixed the R-space range containing the first two shells was fitted by a two shell model. The results of the fit are listed in Table I.

Table I. Results of fitting the reference fcc Ni data. Fixed parameters: R_2/R_1 =1.414; N_2/N_1 = 0.5. Transform: k^1 weighted data, Hamming window, 2.106 to 14.059 Å^{-1} for k-space interval. Fit: 1.095 - 3.517 Å for R-space interval, χ^2_{min} = 6.90 x (10^{-5} Å^{-4}). $\Delta\sigma^2_{2-1} = \sigma^2_2 - \sigma^2_1$. $\Delta E_{2-1} = \Delta E_2 - \Delta E_1$.

ΔE_1 (eV)	R_1 (Å)	σ^2_1 (10^{-3} Å^2)	N_1	ΔE_{2-1} (eV)	$\Delta\sigma^2_{2-1}$ (10^{-3} Å^2)
–7.666	2.483	5.827	11.34	2.663	1.853
±1.4	±0.008	±1.1	±1.4	±2.5	$\pm^{3.8}_{2.5}$

In the above fit if R_1 had been fixed at the known crystallographic value and ΔE_1 was then allowed to float, the resulting χ^2 would be about twice as large as that in Table I, indicating a nonsatisfactory fit. Therefore the difference between the R_1 value shown in Table I and 2.492 Å from x-ray crystallography[23] provides a calibration of the systematic deviation between FEFF calculation and our data, i.e. we have R_1 being systematically smaller than the true value by 0.009 Å or 0.36%. Similarly, the difference between the value of N_1 and 12 (fcc nearest coordination), 5.5%, is also due to an as yet undetermined systematic error in the FEFF code.[24]

The rather large error bars in Table I are reflections of parameter correlations. There are strong correlations in the pairs, ΔE_1 with R_1, and σ^2_1 with N_1. To make sure that we were not misled by the strong correlations, the ΔE_1 and σ^2_1 were also determined by using two other methods as described in the following to check for consistency of the results.

It can be proved mathematically that when the amplitude and phase are removed from a single shell data before the Fourier transform and if there is no E_o shift between the phase and the data, then the peak of the imaginary park of the transform will coincide with the peak of the magnitude, otherwise the two peaks do not line up at the same R value.[16, 25-27].This technique was applied and the results are shown in Fig. 6 which confirms that the ΔE_1 found in the fitting is reasonable. Another way of finding the E_0 shift is to adjust E_0 of either the data or the reference such that the extrapolation of the linear part of the phase difference in (V-5) passes through zero at $k = 0$.[16] The origin of this E_o problem is partially due to the difference in the definition of the zero level of the energy scale and partially due to the discrepancy between the theoretical phase and that extracted experimentally.[20]

As for σ_1^2, a log-ratio analysis on the first shell of fcc Ni was carried out using the effective amplitude from FEFF as the reference, the resulting σ_1^2 was 5.86×10^{-3} Å^2 which is in good agreement with that in Table I. In Fig. 7 the large deviations from a linear behavior in both the low k and high k ends are mainly due to transform artefacts. The linear fitting range is in between the two vertical dash lines in the figure.

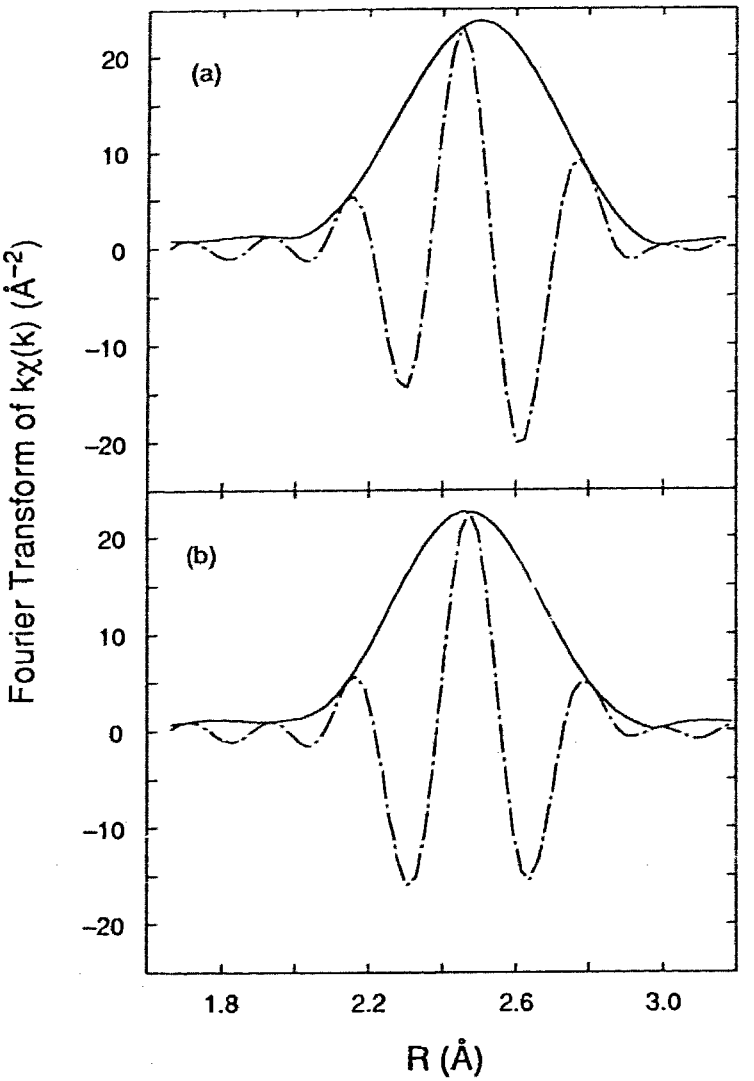

Fig. 6. The magnitude (solid line) and the imaginary part (dash-dot) of the Fourier transform of fcc Ni. In (a) the effective amplitude and phase have been removed, but E_0 has not been shifted. Clearly the magnitude and the imaginary part peak are at different distances. In (b) the effective amplitude and phase have been removed and E_0 has been shifted by 7.57 eV relative to the reference phase. The two peaks coincide. The optimized E_0 shift determined by this method is 7.25 ± 0.5 eV which eliminates the slight asymmetry of the imaginary part.

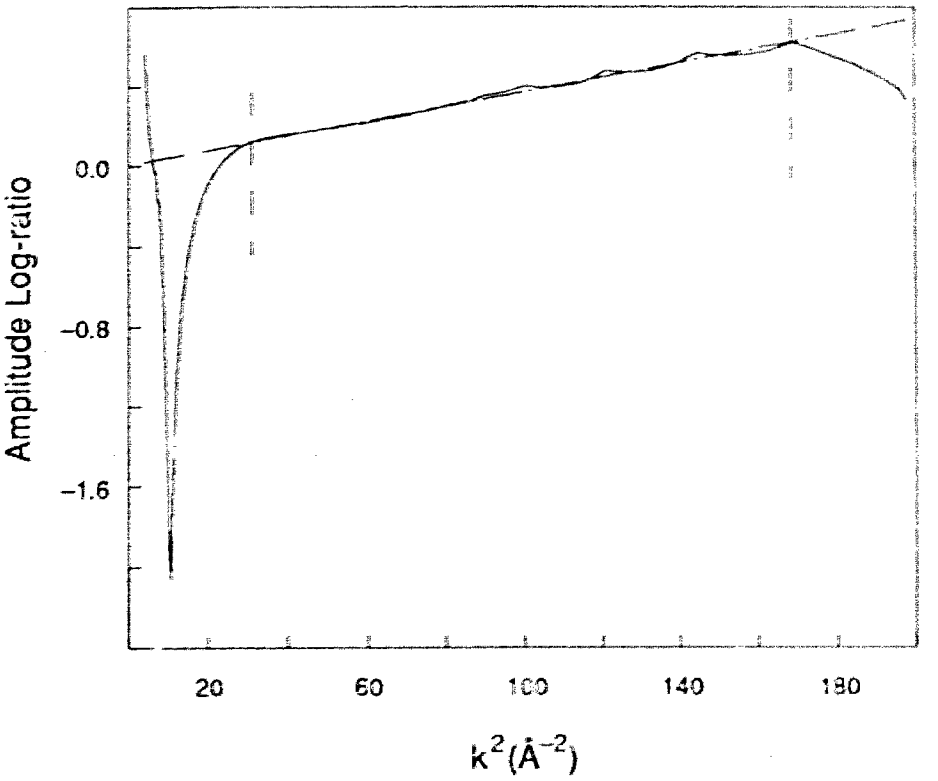

Fig.7 A linear fit to the log-ratio of the first shell amplitude extracted from data of fcc Ni and the effective amplitude from FEFF. The fitting range is indicated by the two vertical dash lines.

We do not have a direct way to assess the reliability of the result for $\Delta\sigma^2_{2,1}$, but its value can be compared indirectly with the result deduced from theoretical calculations. Sevillano *et al.* [28] did *ab initio* calculations of the EXAFS Debye-Waller coefficients with force-constant models for several crystals and the results were in reasonable agreement with the experimental results (at room temperature the deviation was less than 10% in the compared cases).Calculations were done for Fe but not for Ni. At room temperature, the results of EXAFS Debye-Waller factors calculated by Einstein's model differ only by approximately 10% from the ones calculated rigorously.[27, 28] Considering the closeness of the Debye temperatures of bcc Fe (~420 K) and fcc Ni (~400 K),[29] if we deduce the Debye-Waller

coefficient for Ni by first calculating it from Einstein's model and then correct the result by the difference between Einstein's model and the rigorous calculation for Fe, we end up with $\sigma_1^2 = 5.59\text{x}10^{-3}$ Å^2 and $\sigma_2^2 = 7.51\text{x}10^{-3}$ Å^2 or $\Delta\sigma_{2-1}^2 = 1.92\text{x}10^{-3}$ Å^2. We can see that both σ_1^2 and $\Delta\sigma_{2-1}^2$ deduced in this manner are in reasonable agreement with the results found in Table I. The σ_1^2 in Table I includes the contribution from the energy dependence of the absorption background, which is expressed by the multiplicative factor $\mu(E)/\mu(E_0)$ of section II.3.1. If this factor is included using the McMaster tables[30] then the Debye-Waller factor obtained from both the fitting and the log-ratio method will decrease slightly by $0.55\text{x}10^{-3}$ Å^2.

One needs to be cautious about the multiple-scattering effects in EXAFS when analyzing the data beyond the first atomic shell.[19] In large distances the multiple-scattering effects could be dominant in the *R*-space data. However, as demonstrated in a careful study on copper,[31] for a fcc structure the dominant effects of the multiple-scattering contribution appear in the range past the second shell distance. This is also indicated by the fact we could fit the two shells in fcc Ni successfully without considering the multiple scattering effect by the nearest neighbor triangular path[19] and the reasonableness of the parameters extracted from the fitting.

For the 37 ML Ni, we know from our previous beating analysis that it is reasonable to assign two atomic shells to the range $0 < R < 3.5$ Å. With a two shell model the data for the 37 ML Ni were curve fitted and the results are summarized in Table II. Fig. 8 shows the data and fit for one of the samples in *R*-space.

Table II. Results of fitting the 37 ML Ni data. Fixed parameters: ΔE_1 = –5.17 eV and –7.67 eV for the Al-covered sample and the non-covered sample respectively, σ_1^2 = 5.01x10^{-3} Å^2, $\Delta E_{2\text{-}1}$ = 2.663 eV, $\Delta\sigma_{2\text{-}1}^2$ = 1.853 x 10^{-3} Å^2. Transform: k^1 weighted data, Hamming window; the k space truncation intervals were 2.688-12.413Å^{-1}, 2.849-10.033 Å^{-1} and 2.845-14.031Å^{-1} for samples 1, 2 and 3 respectively. Fit: 1.695 - 3.503 Å for R-space interval.

	R_1 (Å)	N_1	R_2/R_1	N_2/N_1	χ^2(10^{-4} Å^{-4})
Sample-1: (no cover)	2.488 ±0.007	7.76 $\pm0.78^{2}_{0}$	1.402 ±0.028	0.423 $\pm0.3^{44}_{31}$	2.50
Sample-2: (Al cover)	2.475 ±0.006	6.12 $\pm0.4^{62}_{94}$	1.409 ±0.018	0.487 $\pm0.2^{73}_{60}$	0.867
Sample-3: (Al cover)	2.486 ±0.005	5.56 $\pm0.4^{49}_{26}$	1.414 ±0.017	0.468 $\pm0.2^{68}_{59}$	0.637

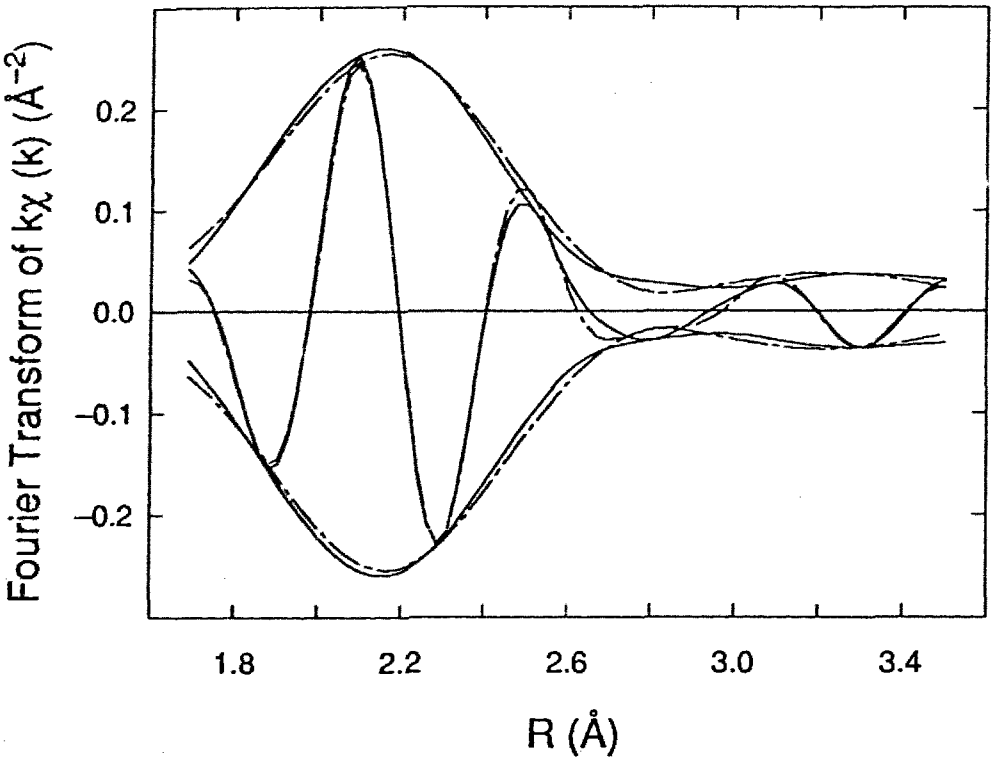

Fig. 8. Two shell fit of 37 ML Ni: the magnitude and the imaginary part of the transform of sample-3 (solid) and the fit (dash-dot).

In the fits $\Delta\sigma^2_{2-1}$ and ΔE_{2-1} were fixed at the values obtained for fcc Ni in Table II. Judged from the similarity between fcc and the 37 ML Ni as discussed in the qualitative analysis, the $\Delta\sigma^2_{2-1}$ in both systems should be reasonably close. Due to the intermixing of the second shell with the higher shells, the attempts to fit the data while letting both N_2 and $\Delta\sigma^2_{2-1}$ float did not yield physically meaningful results. It is likely that the relative disorder between the nearest and the second nearest neighbor shell in the 37 ML Ni sample is larger than that in a polycrystalline sample, so the assumption about $\Delta\sigma^2_{2-1}$ may result in an apparent N_2/N_1 value smaller than the true value.

In Table II the fixed σ^2_1 value was determined from a log-ratio fit for the filtered first shell of sample-3. A similar process for data of sample-1 resulted in basically the same value: the difference was only by 0.7% which has no effect on the results shown in

Table II. The k interval of data for sample-2 was too short for a reliable application of the log-ratio method. Notice that the σ_1^2 value determined for the 37 ML Ni is smaller than that extracted from fcc Ni metal. At first look this appears strange because that seems to suggest the thermal and structural disorder of the first shell in the 37 ML Ni appears to be smaller than that in the Ni metal. We attribute this anomalous effect to the uncorrected $F_0(E)/F_0(E_0)$ factor included in the data as discussed in chapter II. From the size of the effect of $F_0(E)/F_0(E_0)$ estimated from model calculations in section II.3, it can be estimated that if this factor could be excluded from the data the Debye-Waller factor of the 37 ML Ni would be not very different from that of the Ni metal.

The fixed ΔE_1 values used in the fits in Table II were obtained by adding the ΔE_1 of Table I to the E_0 shift found from a phase difference comparison between the phases extracted from the 37 ML Ni data and the fcc Ni data. The criterion used to determine the E_0 difference between the extracted phases was to fit the most linear part of the phase difference and adjust E_0 of either of the phases to cause the extrapolation of the fitting line to pass through the origin.[12] The "rule of thumb" of the correlation between ΔE_1 and R_1 is that every 3 eV change in E_0 corresponds to about 0.01 Å change in R_1. So if the ΔE_1 difference between the samples is ignored there would be a systematic difference of about 0.01 Å in values of R_1 between Al-covered and uncovered samples. This was confirmed by testing of the fits with E_1 fixed at the value of fcc Ni. However, the χ^2 in the testing fits for Al-covered data were nearly 3 times larger than those shown in Table II indicating that the model was less satisfactory.

All the data used in the fits in Table II were taken in the fluorescence mode. The data for sample 1 were obtained while the sample was rotating at 40 Hz around the vertical axis of the surface, which averaged out the Bragg diffraction peaks.[32] The background for the k-space data of sample 1 was removed by a k^1 weighted 9th order polynomial fit, whereas for the other two samples a k^1 weighted 7th order polynomial was used. The data for the other two samples were taken without rotating the sample. The data were cross-checked

with that taken simultaneously with reflectivity and total-electron yield to make sure that they were not contaminated by Bragg diffraction peaks. The no-coverlayer sample was measured in the first run of this system and the x-ray incident angle in that run was not accurately determined, but it can be estimated to be above the critical angle. The reason for the uncertainty was that in our early experiments, the reflectivity data were not properly normalized. The data for the samples 2 and 3 had the incident angles in the vicinity of, but below, the critical angle.

As mentioned before, the error bars shown in Table I and II represent only the precision of the fits, we still have to consider the systematic errors before we reach the conclusion on the structural parameters. For nearest neighbor distance R_1 the systematic errors have the following origins. First, there is an error in the phase calculated from FEFF, which as we have calibrated in the case of fitting of fcc Ni produces an error on R_1 of –0.009 Å. Second, as discussed in chapter II in this range of sample thickness the anomalous dispersion effect causes a small systematic error with a size about –0.002 Å. The third error comes from the uncertainty of the ΔE_1 used in the fits. For example in the case shown in Fig. 6 the optimized ΔE_1 determined by aligning the peaks of the imaginary and magnitude of the Fourier transform is about 0.5 eV below the value used in the fit. This would transform into an error of about 0.002 Å if the ΔE_1 in the fit was fixed 0.5 eV lower. If we now correct the first kind of error by adding 0.009 Å to R_1 and include the second and the third kinds of error into the uncertainty and take average of the R_1 values in Table II weighted by the corresponding $1/\chi^2$, we have our best estimation of the nearest neighbor bond length in the 37 ML Ni as $\underline{R_1 = 2.491 \pm 0.01 \text{ Å}}$. Similarly, $\underline{R_2/R_1 = 1.411 \pm 0.019}$.

For the nearest neighbor coordination number of the 37 ML Ni we have a large spread, this is because a small angle difference in the vicinity of the critical angle could cause a rather large change in the amplitude distortion by the anomalous dispersion effect (see chapter II.3). When the reflectivity curves can be quantitatively described by the

formalism discussed in chapter II, this distortion can be accurately corrected by the calculated results as shown by Heald *et al* in a series of experiments conducted on layered samples with glass as the substrate.[33] Because the amplitude distortion caused by the anomalous dispersion basically scales the overall amplitude by a constant, the effect will be cancelled out in the variable N_2/N_1. As we can see from Table II the agreements of this quantity among the runs are much better than that of N_1. Averaging the results in Table II weighted by the corresponding $1/\chi^2$ we have $\underline{N_2/N_1 = 0.469 \pm 0.2}\ {}^{8}_{7}$

Although it is difficult for us to obtain the nearest neighbor coordination number quantitatively without accurately handling the anomalous dispersion effects in the current case, we can still estimate the upper bound of N_1 as the following. When the weighted average of N_1 in Table II is corrected by the estimated 40% (the upper bound) reduction due to the anomalous dispersion effects and 5.5% systematic reduction due to the FEFF code as calibrated in Table I, we have the N_1 for the 37 ML Ni being ≤ 8.8. This coordination number is significantly smaller than that of a regular fcc structure ($N_1 = 12$), but it is relatively close to that of bcc Fe ($N_1 = 8$).

To estimate the lower bound of the presence of a residual bcc phase in the 37 ML Ni, a 3-shell fitting was conducted. Besides the two shells proposed in Table II, another shell was added to the fit. First it was assumed that the third shell had the same distance as the second shell of bcc Fe. Other parameters were fixed at the same values as the first shell in Table II except the third shell coordination number N' was permitted to float. This fit ended up with a small (8.5% of the N_1 in Table II) and negative N 'which is not physical. Upon permitting the distance of this shell to float, the fit for this shell yielded the same distance as the second shell in Table II but again gave a small negative value. The parameters for the other two shells remained virtually unchanged during these fits.

As indicated by the reasonableness of the structural parameters obtained in the above analysis, we found no evidence of substantial alloying at the Al/Ni interface of the 37 ML Ni samples. On the other hand, Heald and Barrera have shown that for a polycrystalline

sample there is a spontaneous alloying region about 60 Å in thickness formed at the Al/Ni interface at room temperature.[34] We attribute the difference between our results and that in Ref. 34 as being due to the difference in the samples. It is generally accepted that diffusion and transport along grain boundaries can dominate many thin film reaction processes.[35] The 37 ML Ni films used in our experiments are single crystals (as indicated by the RHEED patterns), therefore the density of grain boundaries of the 37 ML Ni should be much less than that of a polycrystalline Ni film case. Also, of course, a polycrystalline sample has more than one crystallographic surface exposed with the possibility of a surface free energy favours the formation of an alloy. In addition, we deposited Al onto the 37 ML Ni under a low substrate temperature (see Chapter IV) which should limit the mobility of the Al atoms on the Ni surface, hence further reducing the possibility of the reaction between the two elements. We also noticed that the integrity of the stabilized Ni phase (>13ML) may be another factor that reduces the alloying at the Al/Ni interface: for a 6 ML Ni covered with Al we observed substantial alloying,[36] it is likely that the intermediate phase at such thickness might have a higher density of grain boundaries.

2.4) Conclusions and Discussion on 37 ML Ni/Fe(001)

The main results on the 37 ML Ni are summarized in the following:

1) The structural parameters obtained from EXAFS are

$$R_1 = 2.491 \pm 0.01 \text{ Å},$$

$$R_2 = 3.515 \pm 0.06 \text{ Å},$$

$$N_2/N_1 = 0.469 \pm 0.2\frac{8}{7};$$

2) The nearest neighbor coordination number is less than or equal to 8.8, which represents a rather large reduction from 12 in a fcc structure. This is also accompanied by a significant reduction in the relative contributions (determined by the relative coordination

number and the Debye-Waller coefficients) of the 3rd and 4th shells compared to fcc Ni metal.

3) From beating and curve-fitting we can see that the structure of the Ni overlayers is not a mixture of bcc and fcc phases;

4) XANES of the Ni overlayers indicates that the Ni overlayers have a different structure from either a bcc or fcc structure.

If we now compare the above structural parameters obtained for the 37 ML Ni with those of fcc Ni metal (R_1 = 2.492 Å, R_2 = 3.524 Å and N_2/N_1 = 0.5) we can see that the local structure of the 37 ML Ni is almost identical to that of fcc Ni within the uncertainties of the EXAFS results* . These results contradict the early qualitative assessment on the structure that it was believed to be mainly a bcc structure with minor defects.[1, 7] In view of our EXAFS results, the weak additional spots which appeared in the RHEED pattern (see chapter IV Fig. 7) after the first 3-6 ML growth actually represent a drastic phase transition. After the film thickness reaches into the stabilized phase range (> 13 ML [2, 3]) the local structure turns into one that is characteristic of fcc structure. The growth is still in a layer-by-layer fashion as shown by the RHEED intensity oscillations but it definitely does not retain a pseudomorphic structure of the substrate surface anymore.

The relative reduction in the contribution to the EXAFS of shells beyond the next nearest neighbor was also observed in a RHEELS study on the same system in UHV environment and without the covering layer on top of the Ni overlayers.[7] Although in the case of RHEELS the *R*-space resolution was much lower than the EXAFS results presented here and the only quantitative result was the nearest neighbor distance (identical to that in fcc within 0.05 Å). Nevertheless, the qualitative agreement between the results of the two techniques is quite obvious when comparing the Fourier transforms in Fig. 4 and that in Fig. 8 of Ref. [7].

---

* The results previously published(Ref.36) were for one sample whereas the results summarized above are the weighted average for 3 samples. The main difference in the published work is that N_2/N_1 = 0.50.

There are no matching planes between fcc and bcc lattices and we know the growth is layer-by-layer. Therefore there must be defects in the Ni overlayers. This is consistent with the RHEED observation that the area density of the Ni overlayers is reduced 7-20% after the first sign of the phase transition occurs.[5] The deviation of the structure of the 37 ML Ni from that of fcc Ni may be related to these defects. This indicates that even at a rather large thickness there are still some strains induced by the Fe substrate existing in the Ni overlayers which prevents them from completely relaxing to the natural fcc structure. RHEED patterns observed during the growth were very reproducible and showed that this supposed defect structure still possessed a square symmetry in the sample surface. This in-plane square symmetry was also indicated clearly by the magnetic properties of the film.[4, 7]

If we use islands of (110) of fcc Ni as building blocks and consider the low area atomic density characterized by the estimated nearest neighbor coordination ≤ 8.8, we have a structure in the 37 ML Ni overlayers which is somewhat similar to bcc Fe(001) layers in the macroscopic sense: similar nearest neighbor coordination number and similar interlayer distance (with that in fcc Ni(110) being 13% smaller). This might be the reason why one could interpret the magnetic measurements with a bcc Ni model in mind.

EXAFS, as a local probe, partially revealed the nature of this metastable phase of Ni overlayers. It is however unable to detect the characteristics related to the long range order. In the final solution to the structure, the nearest and next-nearest neighbor information provided here could serve as the constraints on the modeling.

V.3) 9 ML Ni/Fe(001)---An Intermediate Phase

In this section we study the structure after the phase transition in the Ni overlayers on Fe(001) started. The system used is Au(10 ML)/Ni(9ML)/Fe(9ML)/Ag(001). The

thicknesses of the Ni and Fe overlayers are in the range usually referred to as *ultrathin*, i.e. the thickness is thinner than the magnetic exchange length (e.g. ~ 33 Å for Fe).[5] To a good approximation, Fe(001) films grown on Ag(001) can be regarded as having the normal bcc Fe lattice as discussed in chapter IV. The growth of Ni on ultrathin Fe(001) on bulk Ag(001) is similar to the growth of Ni on bulk Fe(001). Both types of Ni films exhibit identical RHEED patterns with the same critical thickness for the transition from a pure bcc Ni (thickness less than 3~6 ML) into the new phase.[6] The 10 ML Au grown on the top of the Ni film protects the sample from oxidation when it is taken out of the UHV environment. All of the growths were in a layer-by-layer fashion as monitored by RHEED intensity oscillations (see chapter IV).

Due to the fact that the sample layer is very thin, according to the calculation in chapter II the distortion in EXAFS by the anomalous dispersion effect will be negligibly small. Thus besides obtaining the bond lengths we are also able to obtain the coordination numbers in the conventional fashion.

The main reason Ag was used as the substrate of the system was to reduce the magnetic signals from the substrate material in studying the magnetic properties so that the magnetic properties of the Ni overlayers could be measured better. This turns out to be also beneficial for applying glancing-incidence XAFS in the fluorescence detection mode. The reason lies in the energy differences among the fluorescent yield from different elements involved. When the incident x-ray is around the Ni K-edge (8.333 keV), the excited core levels in the substrate and the covering layer are Ag L-edges and Au M-edges. Therefore the fluorescent photons yielded from the substrate and the covering layer have energies generally less than 3 keV which is much smaller than the energy of the fluorescence yield of Ni (~7.5 keV) and these low energy fluorescent photons can be easily filtered out from the total signal. A thin piece of plastic between the sample and the detector is sufficient for the filtering. The consequences of this signal discrimination are twofold. Firstly, the filtered signal has a much lower background intensity. Secondly, for the thin sample case

(<10 ML) the distortion in XANES due to the anomalous dispersion is practically eliminated (see chapter II.2.3). In our experiments the plastic cap of the electron detector (see chapter III.2.1), which is between the sample and the fluorescence detector (see chapter III Fig. 1), plays the role as the signal filter. The experimental evidence of these statements will be presented in the next chapter where the validity of these points will be fully substantiated by experimental results on the Au(10ML)/Cu(8ML)/Ag(001) system.

What we are mostly interested in is still a Ni/Fe(001) problem, so the analysis methods in this section will be in a parallel fashion to those used for the 37 ML Ni case.

3.1) XANES of 9 ML Ni/Fe(001)

Fig. 9(a) shows that the K-edge XANES of fcc Ni metal and 9 ML Ni, and the K-edge XANES of bcc Fe metal and 9 ML Fe. The curves have been displaced vertically for clarity and the first inflection point of each curve has been defined to be the energy zero. 5 passes of a 3-point smooth function[10] were used to smooth the curve for the 9 ML Fe, the other curves were smoothed by 2 passes of the same function. Unlike the case of the stabilized phase (37 ML), the XANES of the 9 ML Ni is strikingly different from that of fcc Ni which is the natural phase of Ni metal. It can be seen that the 9 ML Ni XANES is quite similar to that of the 9 ML Fe layers underneath, and the latter is identical to that of bcc Fe metal as far as the major features are concerned. A more detailed comparison is shown in Fig. 9(b) by the derivatives of the XANES. In the range from 5 to 30 eV above the absorption threshold the 9 ML Ni follows the same trend as that in 9 ML Fe and bcc Fe, and in particular, they all have a dip just above 20 eV whereas the fcc Ni has a peak. However, in the higher energy range (>40 eV), i.e. when we are getting into the EXAFS range, the 9 ML Ni tends to be more similar to that of the fcc Ni.

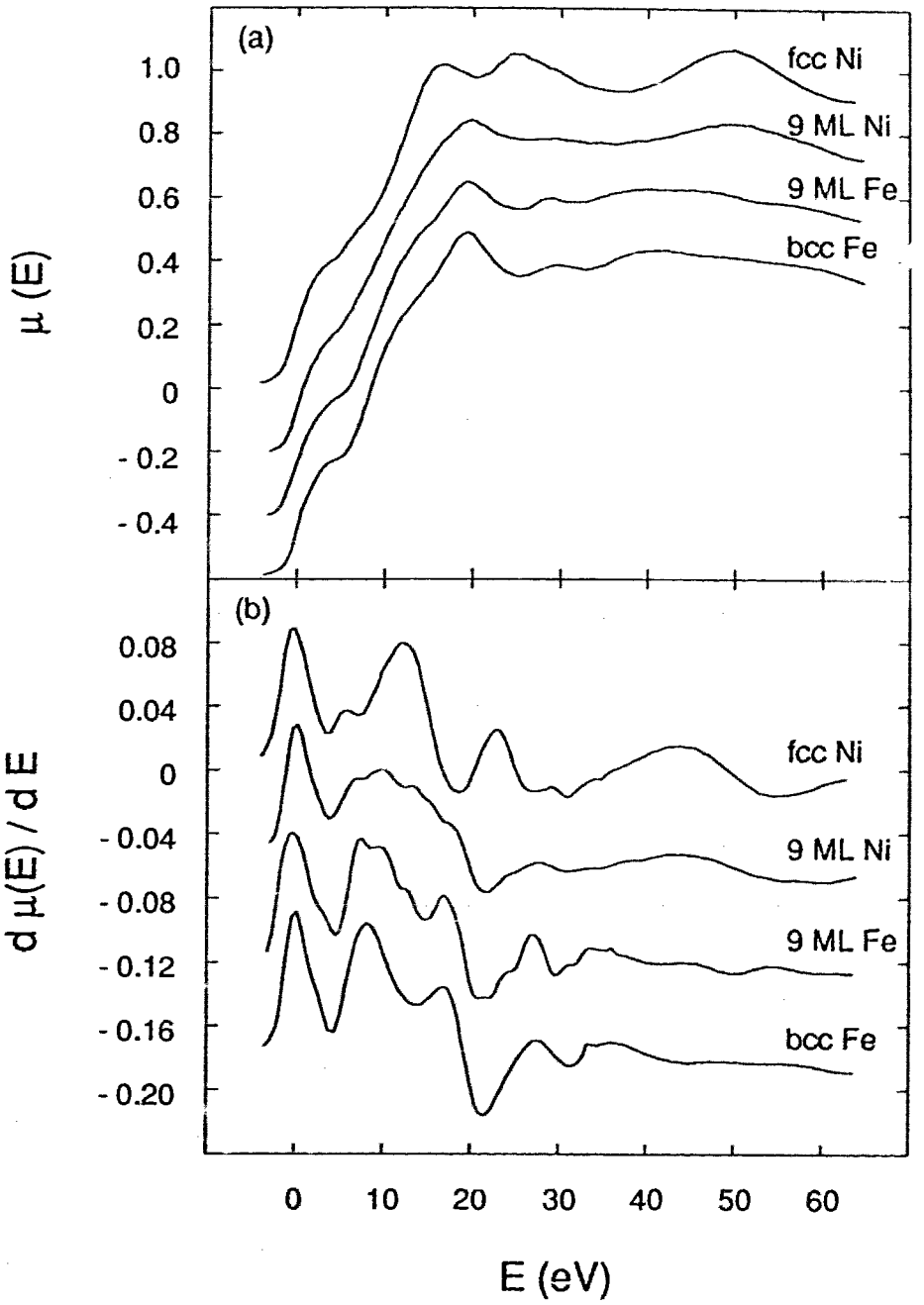

Fig. 9 XANES of Au(10ML)/Ni(9ML)/Fe(9ML)/Ag(001) and references. (a) XANES of the sample and references. (b) The derivatives of the XANES with respect to energy.

3.2) Qualitative Analysis of the EXAFS of 9 ML Ni/Fe(001)

3.2.1) Comparison of $\chi(k)$

In Fig.10 we compare the EXAFS interference functions. First of all, the resemblance between the 9 ML Fe and bcc Fe is quite obvious. Nearly all the major peaks of bcc Fe are coincident with those in the 9 ML of Fe, except the features above 11 $Å^{-1}$. In contrast to what we might have expected on the basis of the XANES comparison, we see the EXAFS of the 9 ML Ni is strikingly different from that of the 9 ML Fe and bcc Fe. Neither is the 9 ML Ni as similar to the fcc Ni as was in the case of the stabilized phase.

The spectra for the 9 ML Ni and the 9 ML Fe in Fig.10 clearly demonstrate the advantage of using EXAFS on such systems, i.e. the element selectivity enables us to easily separate the signals coming from different layers. On the other hand, the quality of the sample growth is also tested. If severe alloying had happened at the Ni/Fe interface in the final form of the sample, the Ni K-edge data and the Fe K-edge data would look the same because the backscattering amplitudes of Ni and Fe atoms are indistinguishable in the sense of EXAFS signals.[37]

Another point worth mentioning about these opposite trends in comparisons of XANES and EXAFS is that it is not reliable, at least for the systems discussed here, to correlate the features in the XANES of the 9 ML Ni *directly* to the interatomic distances.[38]

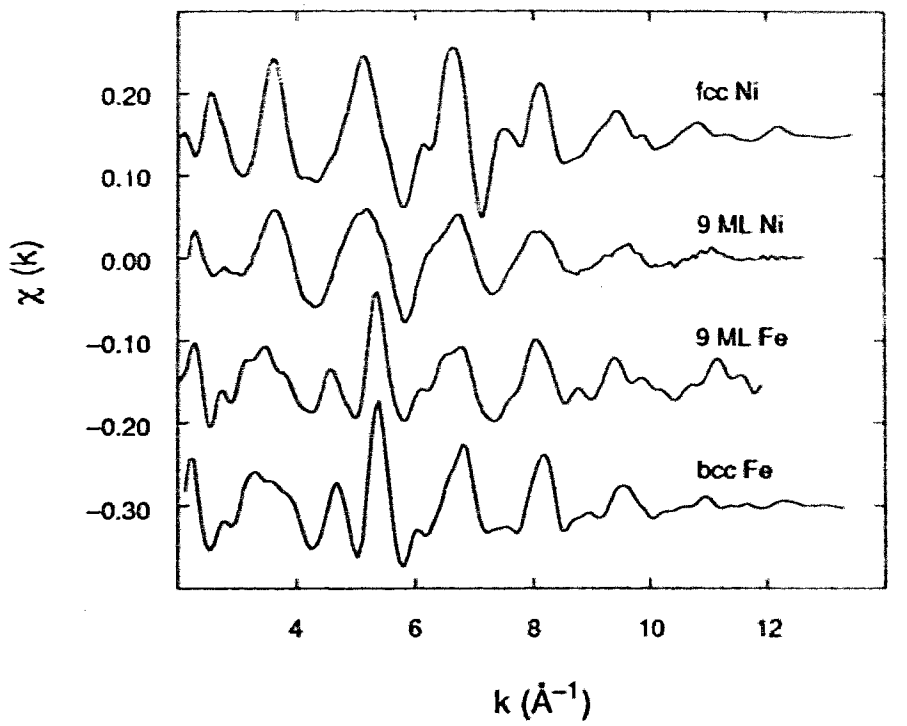

Fig. 10 Comparison of interference functions for Ni and Fe. The curves were obtained by removing the background from the raw data using a k^1 weighted 7th order polynomial fit to the background. For the curve of the 9 ML Fe one extra step, a Fourier filtering (from 0 to 9 Å in *R*-space), was used to filter out the high frequency noise.

3.2.2) Comparison of the Fourier Transforms

The significance of the differences shown in EXAFS in Fig. 10 can be more clearly seen from their Fourier transforms as shown in Fig.11. The transforms were obtained using 10% Gaussian windows with *k*-space intervals of 2.142 - 12.52 Å^{-1} for Ni data and 2.11 - 11.66 Å^{-1} for Fe data. Notice the different vertical scales of the upper and lower panels. In Fig. 11 the short vertical lines and the numbers indicate approximately the positions of the neighboring atomic shells. The Fourier transforms in Fig. 11 include the EXAFS phase shifts, so the peak positions do not correspond directly to interatomic

distances. The features below 1.5 Å correspond to low frequency modulations in $\chi(k)$, i.e. the residual of background signal modulations.

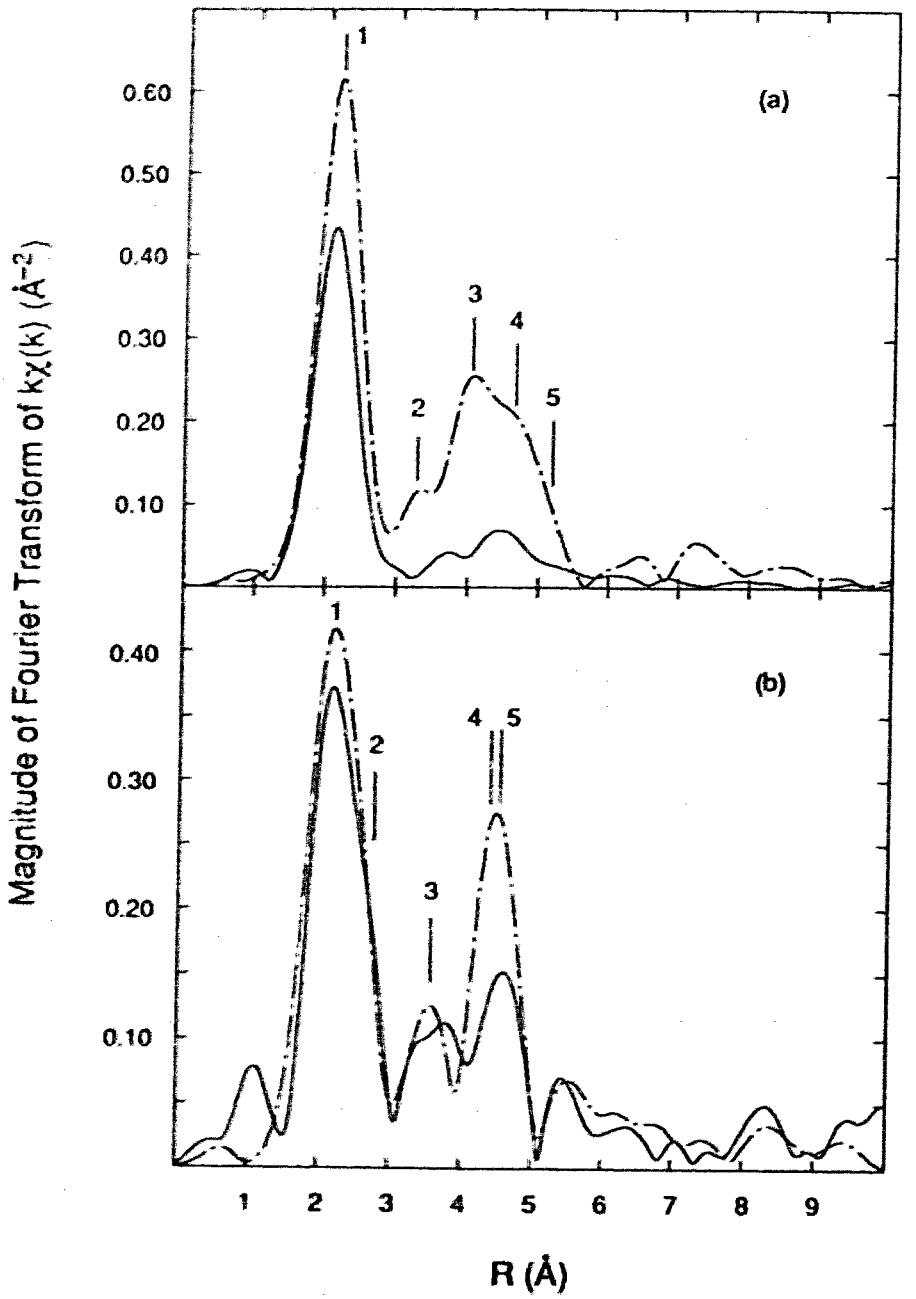

Fig. 11. Magnitude of Fourier transforms for Ni and Fe. (a) The solid line is the 9 ML Ni and the dash-dot line is fcc Ni metal; (b) The solid line is the 9 ML Fe and the dash-dot line is bcc Fe.

In Fig.11(b) we can see that the 9 ML Fe is indeed very close to that of the bcc Fe. The asymmetry in the highest peak, peak 1, and the abnormal large magnitude of the peak between 4 and 5 Å, are the characteristic features of a bcc structure. However, the structure of the 9 ML Fe also deviates from a perfect bcc one in a few ways. The differences are readily apparent beyond the second nearest neighbor. We are unable to provide a quantitative analysis of the large *R*-region, but we will make the following qualitative comments. First of all, the 3rd, 4th and 5th shells are expanded relative to those of bcc Fe metal. Second, the peak corresponding to the third shell in a bcc structure splits indicating that either a new shell may be formed in between the third and fourth shells of bcc Fe or the nearest neighbor triangular multiple-scattering paths may be substantially different from that in normal bcc Fe. Thirdly, the 180° multiple-scattering peak (the fifth shell in the bcc structure) between 4 an 5 Å is much weaker in the 9 ML Fe than in bcc Fe. That means some of the body-center-diagonal Fe-Fe-Fe bridges are lost or the angle between the two bonds is not 180° anymore. This may indicate that the vertical lattice constant of the 9 ML Fe is not equal to that in bcc Fe, or, there is a displacement of the an individual layer in the (001) plane relative to its neighboring layers. But, the overall structure of the 9 ML Fe is still pretty much a bcc one.

As shown in Fig.11, the assignment of atomic shells for the 9 ML Ni is not at all clear. Later we will show that the highest peak around 2 Å is a single shell peak. Notice that this peak shifts slightly to a shorter distance relative to that in fcc Ni and the peak height is about the same as that of the bcc Fe metal. The latter observation indicates, to the zeroth approximation, the nearest neighbor coordination number of the 9 ML Ni may be higher than that of the equivalent bcc Fe because the peak for bcc Fe has two shells under it. Another thing easily noticeable is that for the 9 ML Ni the apparent second shell peak, at about 3.65 Å on the figure, is at a larger interatomic distance than either bcc Fe or fcc Ni case. That seems to suggest this shell is stretched apart from the central absorbing atom.

However, at such a distance the multiple-scattering contribution starts to become the dominant effect in a fcc lattice, so the apparent lattice stretching could also be due to the modification of the multiple-scattering paths of a fcc lattice. The part of the transform with $R > 3$ Å has a smaller relative intensity relative to either of the references and that of the 9 ML Fe. This could mean either or both i) large static disorder exists in the high R part; and ii) there are some missing atoms (e.g. defects) in the plane. There is also a third possibility for the large magnitude reduction in the high R-region, i.e. in the 9 ML Ni, the density and the level of the static disorder are still more or less the same as in the reference cases but the latice is distorted in such a particular way that the contribution from many multiple-scattering paths are suppressed (e.g. many bond angles are near 90°[19]). Intuitively, this third possibility is less likely than the previous two.

3.2.3) Beating Analysis

The assignment of a single shell to the peak around 2 Å for the transform of the 9 ML Ni is achieved by the beating analysis. The $k\chi(k)$ data from 2.107 to 11.658 Å^{-1} were Fourier transformed, the contents in the range from 1.518 to 3.059 Å of the transforms were filtered and back-transformed and hence the corresponding phase function was extracted. In Fig. 12 we compare the derivative of the extracted phases of the 9 ML Ni, the 9 ML of Fe and bcc Fe. The three data sets were processed in exactly the same way for the purpose of comparison. In the figure we see there is a clear dip around 4 Å^{-1} for both the 9 ML Fe and bcc Fe, which is the first order beat node corresponding to the distance difference between the second and the first shells in the bcc Fe structure. In the same region, the curve for the 9 ML Ni is completely flat, i.e. there is only a single shell in the R range selected. The curvatures in both ends of curves for the 9 ML Ni and bcc Fe are due to transform artifacts because their existence and position are related to the detail of the transform procedures, e.g. slightly different window width, different k weighting in the forward-transform. Real features cannot be eliminated by any sensible processing

procedures. On the other hand, if the dip of the 9 ML Ni around 2.5 $Å^{-1}$ were the first order beat node, then we should be able to see the third order node around 7.5 $Å^{-1}$, but this is not the case. This is another way to distinguish a real feature from artifacts. The shallow dip near the high *k* end of the curve for the 9 ML Fe is not dependent on the detailed data processing procedures, but it is in the region where the data quality is rather poor so it is not clear at this point whether it is a real feature.

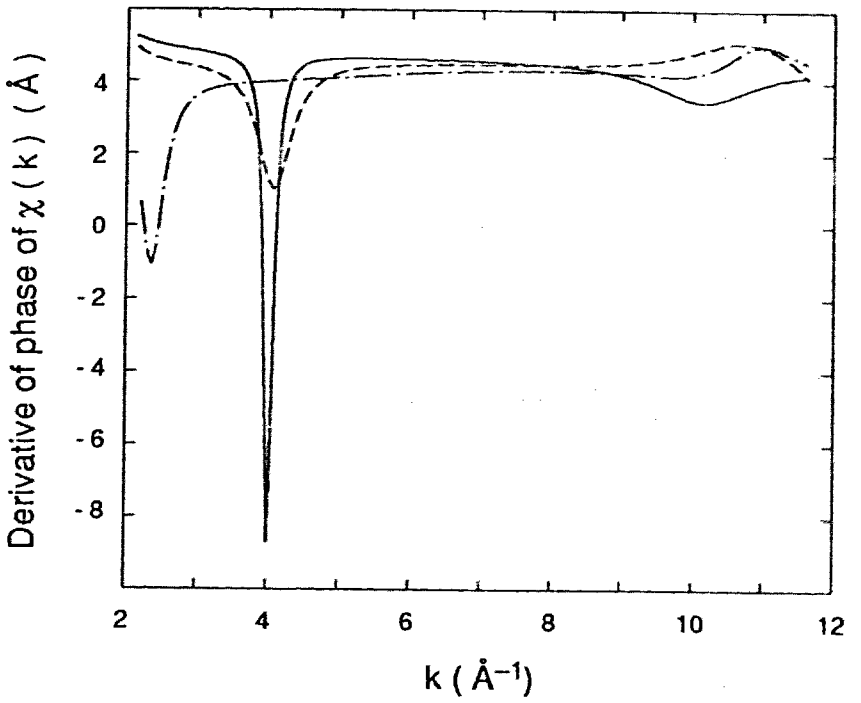

Fig. 12. Derivatives of the phases extracted from data of the 9 ML Ni (dash-dot), the 9 ML Fe (solid) and bcc Fe (dash).

Through the above qualitative analyses, one point which becomes quite clear is that at this intermediate stage in forming the stabilized phase (>13 ML) the structure of the Ni overlayers is definitely not mainly bcc anymore.

3.3)Quantitative Analysis of the EXAFS of 9 ML Ni/Fe(001)

3.3.1) Phase-difference and log-ratio results

The first shell of the 9 ML Ni is quantitatively analyzed in this section. In Table III the results from the phase-difference and log-ratio method are summarized, where the reference backscattering amplitude and phase of a Ni atom were extracted from the transmission data taken on a Ni foil. Whenever comparison is made between the reference and the unknown, the two data sets were processed in exactly the same way in order to cancel out the effects of the transform artifacts as much as possible. It was found that the E_0 of the 9 ML Ni needed to be shifted by –2.5 eV relative to that of the fcc Ni to enable the linear least-squares fit of the phase difference to pass through the origin. This E_0 shift was also confirmed by using the method of Lee and Beni[16, 25] as discussed in the analysis of the 37 ML Ni case. It is interesting to notice that the amount of the E_0 shift relative to the fcc Ni in this 9 ML Ni case is the same as in the case of Al covered 37 ML Ni (see II.2.3). The drawback of this analysis technique is that the results are related to the linear fitting intervals believed to be unaffected by the transform artifacts, so it is not very objective to assign error bars to the results. In Table III we listed the results from two out of many different ways tested for processing the data, the deviations between the results provide a typical estimation of the reliability of the results. Fig. 13 shows the data and the linear fits used to obtain the results in Table III.

In Table III and Fig. 13 we can see that the nearest-neighbor distance in the 9 ML Ni is contracted compared with that in fcc Ni by about 0.06 Å. From the difference in the EXAFS Debye-Waller coefficient we can see that the static disorder in the 9 ML Ni is only slightly larger than that in fcc Ni metal. From the average of the ratio in the last column of Table III and the crystallography value of fcc Ni, the nearest-neighbor coordination number of the 9 ML Ni becomes 9.08 ± 0.07. The error bar loosely assigned here is simply the from difference from the two rows in Table III.

The reason we show the results from the phase-difference and log-ratio in such a detailed way is because in the following we will see that the R_1 result from the curve-fitting is about 0.03 Å larger than that in Table III. Although both the analyses show there is a contraction for the first nearest neighbor distance of the 9 ML Ni compared to that in fcc Ni, the difference in quantitative results is larger than the usual error bar for the nearest neighbor distance, e.g. ±0.01 Å in the 37 ML Ni case discussed earlier. We do not know what is the origin of this systematic difference.

Table III. Phase-difference and log-ratio results on the 1st shell of 9 ML Ni. The first three columns describe the Fourier filtering: k weighting, k-space data range used and R-space filter range. $\Delta R = R_{9ML} - R_{fcc}$ and $\Delta\sigma_1^2 = \sigma_{9ML}^2 - \sigma_{fcc}^2$.

	k-interval (Å^{-1})	R-interval (Å)	ΔR (Å)	$\Delta\sigma_1^2$ (10^{-3}Å^2)	$[N_{9ML}R_{fcc}^2/N_{fcc}R_{9ML}^2]$
$k\chi(k)$	2.333-12.607	1.560-2.652	–0.063	0.866	0.772
$k^3\chi(k)$	2.188-12.607	1.620-2.725	–0.062	0.962	0.780

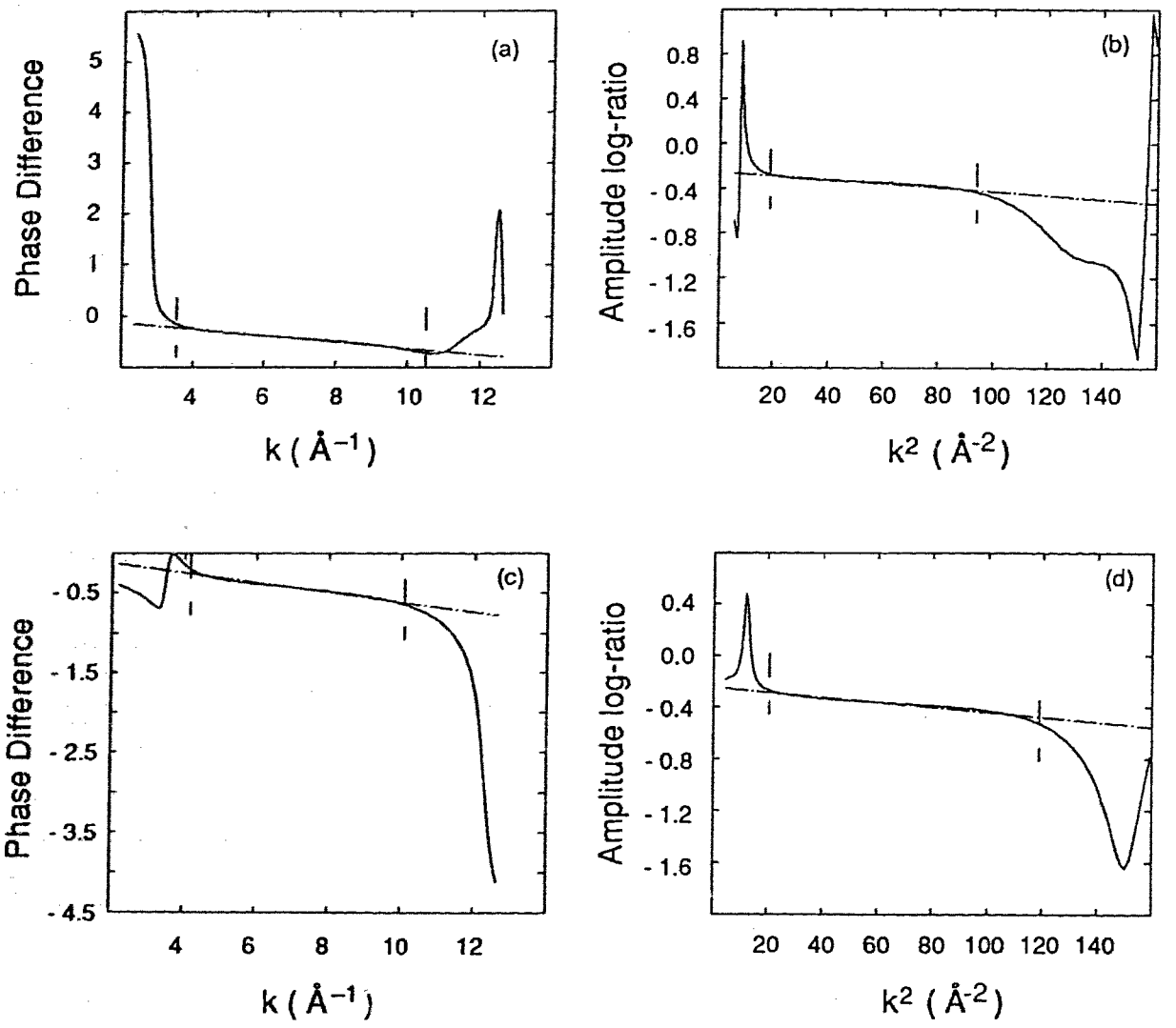

Fig. 13. Linear least-squares fits for the phase differences and amplitude log-ratios between the 9 ML Ni and the fcc Ni samples. (a) and (b) correspond to the first row of results in Table III, (c) and (c) correspond to the second row.

3.3.2) Fitting Results

Table IV and Fig. 14 show the results of one shell curve-fitting for the first shell of the 9 ML Ni. The good quality of the fit shows that a single shell model is enough to interpret the data in that R-space range. Therefore the fitting confirms that there is no residual bcc structure left in the data, which is consistent with the beating results. That means the structure of the Ni overlayers in this case cannot be a mixture of bcc and fcc phase.

Table IV. One shell curve-fitting for the 9 ML Ni. Theoretical amplitude and phase calculated using FEFF code were used in the fit function and $\Delta E_1 = -5.17$ eV was fixed. Transform: k^1 weighting, Hamming window, 3.232 to 12.431 Å^{-1} for k-space interval. Fitting ranges are shown in Fig. 14.

R_1 (Å)	σ_1^2 (10^{-3} Å^2)	N_1	χ^2 (10^{-5} Å^{-4})
2.451	6.59	8.43	2.25
±0.003	±1.1	$\pm^{1.0}_{0.9}$	

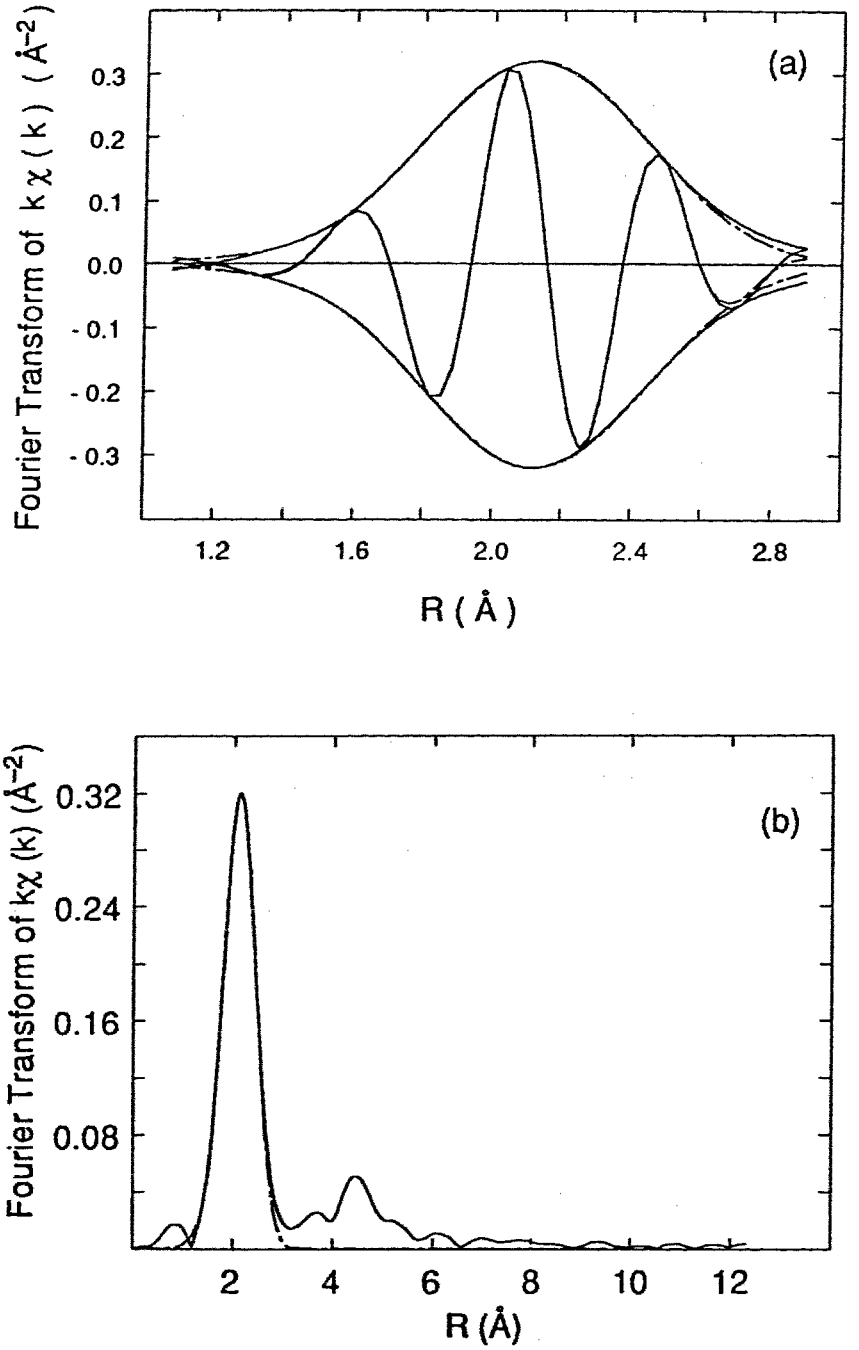

Fig. 14 Curve-fitting for the 1st shell of the 9 ML Ni: (a) magnitude of the transform plus the imaginary part, data (solid) and fit (dash-dot); (b) magnitude of the transform of data (solid) and fit (dash-dot) in a larger *R* space range.

Proceeding similarly to what we did in the 37 ML Ni case, we correct the R_1 by adding to the value in Table IV the systemic deviation 0.36% due to the theoretical phase used and include other systematic uncertainties in the final error bar. We have for the 9 ML Ni from curve-fitting: $\underline{R_1 = 2.460 \pm 0.005}$ Å. This shows the nearest neighbor distance contracts by 0.032 Å from that of fcc Ni (2.492Å). Notice the difference in the amount of this contraction obtained from the curve-fitting and from the phase-difference method (see Table III). For N_1, we add to the value in Table IV the systematic deviation, 5.5%, and include in the uncertainty the residual anomalous dispersion effect in the worst case, 6%. Thus we have $\underline{N_1 = 8.89 \pm 1.5}$. This is in good agreement with 9.08 obtained by the log-ratio method. In the error bar we include the uncertainty due to ignoring the background multiplicative factor $F_0(E)/F_0(E_0)$ (see chapter II.3.1) which was estimated by a model calculation to be 0.4×10^{-3} Å^2. This results in $\sigma_1^2 = 6.59 \pm 1.5$ (10^{-3} Å^2). Comparing the Debye-Waller coefficients in Table IV with that in Table I we have the difference $\underline{\Delta\sigma^2_{1\,9ML-fcc} = 0.76 \pm 1.5}(10^{-3}$ Å^2), which is in fair agreement with 0.91 (10^{-3} Å^2) obtained by the log-ratio. This value gives the estimation of how much softer and more disordered the 9 ML Ni is compared with fcc Ni metal.

3.4) Conclusions and Discussion on 9 ML Ni/Fe(001)

The main results on the 9 ML Ni are summarized here:

1) The structural parameters obtained from EXAFS are

$$R_1^* = 2.445 \pm 0.015 \text{ Å},$$

$$N_1 = 8.89 \pm 1.5,$$

$$\Delta\sigma^2_{1\,9ML-fcc} = 0.76 \pm 1.5 \text{ Å}^2;$$

---

* This is the average of the phase-difference and curve-fitting results.

2) The beating analysis excludes the possibility that the structure has any significant amount of bcc phase, i.e. after the first phase transition or at least at 9 ML thickness the layers originally in bcc phase are also transformed into a new phase,

3) XANES of the 9 ML Ni overlayers resembles that of bcc Fe,

4) The apparent second major shell of the 9 ML Ni appears to be at approximately 3.65 Å, which is larger than that in either bcc Fe or fcc Ni.

The transition from bcc to the stabilized phase involves a continuous change. This was observed by LEED previously and now from the XAFS aspect we have provided the local view in the middle of the continuous structural change.

The result of the contraction of R_1 was surprising. The amount of the Debye-Waller coefficient increase of the first shell in the 9 ML Ni seems not large enough to cause the asymmetry in the pair distribution function which would generate a false shrinkage of the bond length.[27] So the contraction we saw from both the phase-difference method and the curve-fitting seems to be real, and the ΔR change is somewhere in between –0.03 to –0.06 Å. Note that this contraction in R_1 may not necessarily mean the atomic volume in the 9 ML Ni overlayers is smaller than that in fcc or bcc Ni structures. The point is that the second major shell in the 9 ML Ni appears to be at a much larger distance than in either of the two cases which may provide the balance for the atomic volume. However, this is complicated by the contribution of the nearest neighbor triangular multiple-scattering paths to $\chi(k)$. It is known that the first few monolayers of the Ni overlayers started as a pure bcc structure for which R_1 would be 2.483 Å. The contraction of R_1, hence the contraction of the c lattice constant may be the indication of the transition of the bcc (001) into a fcc (110) plane which is a plausible model for the thicker overlayer case. The interplane spacing of fcc Ni (110) is about 13% smaller than that of bcc Fe(001).

The result of N_1, average nearest neighbor coordination, shows from an aspect other than interatomic distances that the local symmetry of the Ni site in the Ni overlayers is

unlikely to be bcc which needs the nearest coordination of 8. An average coordination of 9 would mean that the structure has to contain some missing atoms at Ni sites, i.e. a defect model is needed.

It is interesting to notice that the nearest neighbor coordination of the 9 ML Ni is very close to the nearest neighbor coordination estimated for the 37 ML Ni (≤8.8, see section V.2.4). In both of these two cases the nearest neighbor coordination is far less than that in a pure fcc structure where N_1 =12, but it is rather close to that in a bcc structure (N_1 = 8). The similarity between the modulated structure Ni overlayers and bcc Ni in terms of the nearest neighbor distance and coordination number may be relevant to the interpretation of the magnetic properties of these films[6, 7] assuming a bcc structure for the Ni overlayers. However, the XAFS results presented in this work indicate that on a microscopic level the assumption is not valid.

V.4) 3 ML Ni/Fe(001)---the bcc phase

We attempted to probe the local structure of the bcc phase of the Ni overlayers in two different experiments, but we could not obtain the XAFS data adequate for a detailed determination of the local structure. Here we will provide a brief summary for these two experiments.

In our first attempt to detect the local structure of the bcc Ni, we grew a 6 ML Ni film on Fe(001)C at room temperature and then the sample was covered with 54 Å of Al evaporated at a low substrate temperature (–134°C). In the particular growth the structural modulation in the Ni overlayers occurred around 4.5 ML as indicated by the additional weak RHEED features. In view of what we have found in the 9 ML Ni case in the previous section, it is very likely that after the phase transition the first 4.5 ML of the Ni overlayers was no longer bcc. At the time of the experiment this was not realized (it was believed that

the additional RHEED features merely reflected a mild reconstruction on the very top layer). This sample was measured in a glancing-incidence XAFS experiment and the results indicated that substantial alloying occurred at the Al/Ni interface.[36]

Our second try to detect the local structure of the bcc Ni was made on a sample with 3 ML of Ni grown on substrate Fe(001)C and 10 ML of Au grown on top of the Ni layers (see section IV.3.1). The thickness of Ni was chosen to ensure that the Ni was in the pure bcc state (see RHEED patterns in section IV.3.1). The glancing-incidence XAFS data of this sample were taken on beam lined IV-1 at SSRL. A Si(111) double-crystal monochromator was used with the entrance slit set at 0.5mm. To reduce harmonic contamination in the incident beam the monochromator was detuned above the Ni K-edge such that the current reading in the I_0 chamber was 50% of its maximum value (see chapter IV Fig. 1 for the experimental set up). The XAFS data were acquired in all the three detection modes, namely fluorescence, total-electron-yield and reflectivity.

Although much effort was made, the quality of the data obtained for this sample was inadequate for a detailed analysis. Even if the high quality data were available, the analysis would not be straightforward because the top and bottom layers of the 3 ML Ni layers had Au and Fe as nearest neighbors respectively. This would be the case even if ideally sharp interfaces were assumed. In Fig. 15 the XANES of the 3 ML Ni are shown. Comparing the XANES in Fig. 15 with the XANES of bcc Fe (see Fig.9 of this chapter), we can see that some similarities exist. But it is difficult to compare detailed features in view of the low data quality shown in Fig. 15. Nevertheless, the XANES of the 3 ML Ni is certainly different from that of fcc Ni (see Fig. 9 of this chapter) and it seems that in the gradual structural transition from the 3 ML to 9 ML the essential features of the XANES are retained.

We will leave this section with the statement that the 3 ML Ni XANES results are not inconsistent with the bcc structure assessment obtained in RHEED and LEED studies.

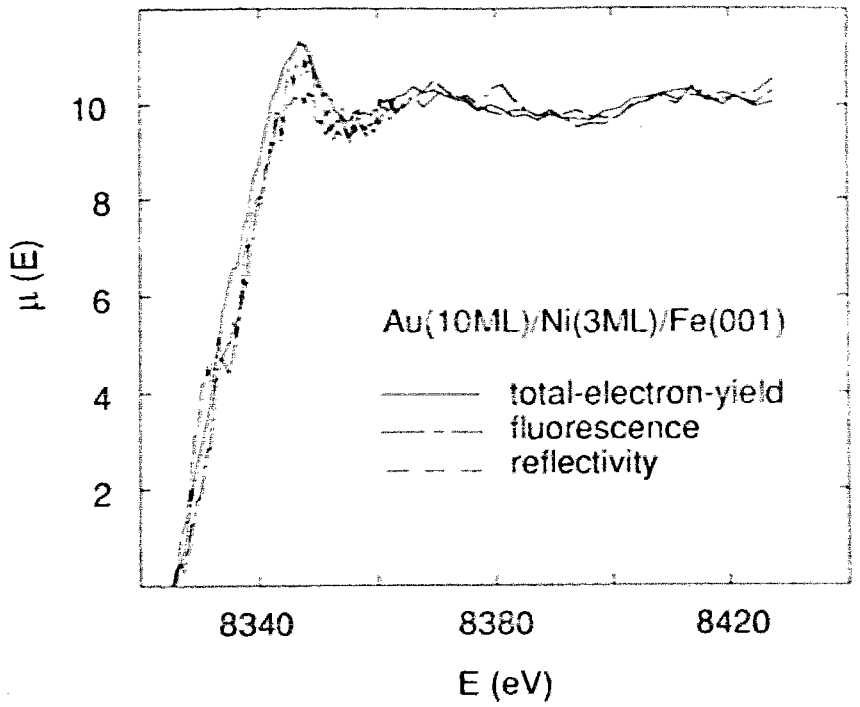

Fig. 15. XANES of 3 ML Ni on Fe(001).

Chapter VI Data Analysis and Results on Cu/Ag(001)

VI.1) Introduction

In the Ni/Fe(001) system, the magnetic properties of the Ni overlayers are intimately coupled with that of ultrathin Fe(001) films. It is then not very straightforward to unravel the roles played by the Ni or Fe alone in the combined magnetic properties measured from such system.[1] In view of the similarity of Ni and Cu atoms (they are adjacent in the periodic table) and considering that Cu is nonmagnetic, it is then natural to study whether the Cu overlayers on Fe(001) behave similarly to Ni and if so, the magnetic property of Fe films after the Cu transforms away from a pure bcc structure could be singled out.[2] This idea intrigued a series of interesting results in the studies of the coupling between ultrathin magnetic films buffered with a Cu ultrathin film.[3] On the side of structural studies of the Cu overlayers, we applied the glancing-incidence XAFS technique on a prototype of such systems: Cu overlayers grown on a bulk Ag(001) surface.[4]

In this chapter we present our glancing-incidence XANES and EXAFS results for a single 8 ML Cu film epitaxially grown on a Ag(001) surface and covered with 10 ML of Au. The structure of the Cu in the Cu/Ag(001) system as determined by using XPD[5] and RHEED[3] has been reported to be close to bcc. Our EXAFS shows that the Cu is body centered tetragonal with the c-axis (perpendicular to the substrate) being expanded 7.6% relative to the *a*-axis. This system is important in the context of the magnetic behavior of Fe/Cu/Fe trilayers on Ag(001). Heinrich and coworkers have shown that the exchange coupling depends on the thickness of the Cu interlayer, changing from ferromagnetic to antiferromagnetic for greater than 8 ML of Cu.[3] Initial theoretical attempts to explain the antiferromagnetism assuming a pure bcc structure of Cu were unsuccessful.[6]

VI.2) Experimental

The sample measured was a 8 monolayer single crystal Cu film epitaxially grown in the MBE chamber (see chapter IV) on a Ag(001) surface, in the form of a disk with 1.5 cm diameter. On top of the Cu film a single crystal Au layer of 10 ML was grown to protect the Cu film from oxidation when it was later taken out of the ultra-high vacuum for the glancing-incidence EXAFS studies.

The XAFS data were taken on beam line IV-1 at SSRL operating in dedicated mode with SPEAR providing a 3 GeV electron beam at a typical current of 50 mA. A Si(220) double-crystal monochromator was used with the entrance slit set at 0.5mm. To reduce harmonic contamination in the incident beam the monochromator was detuned above the Cu K-edge such that the current reading in the I_0 chamber was 50% of its maximum value.

VI.3) Experimental Results

3.1) Anomalous Dispersion Results

Because both the Au and Cu layers are very thin, the effective critical angle φ_c of the sample is determined mainly by the Ag substrate. In the energy range of Cu K-edge XAFS, the effective φ_c is about 6.8 mrad. In order to establish the angular scale, the fluorescence, total electron yield and reflectivity were measured as a function of the incident angle while the photon energy was kept at different constant values below and above the Cu K-edge. XAFS spectra were then obtained at angles ranging from ~ $0.5\varphi_c$ to $1.5\varphi_c$. While taking the initial spectra, any Bragg peaks and other reproducible suspicious features (e.g. monochromator crystal "glitches" [7]) were located by cross-examining the data collected simultaneously in the three methods, and the azimuthal orientation of the sample and the monochromator detuning condition were adjusted to optimize the XAFS signal.

Due to anomalous dispersion, the near edge structure obtained by total electron yield and reflectivity changes with the incident angle φ, leading to a severe distortion in the near edge part of the data when φ approaches φ_c. This is shown in Fig. 1 (a) and (b) indicated by the systematic lineshape change as the incident angle varies. However, the fluorescence signal was found to be independent of the incident angle φ (see Fig. 1(c)): the background fluorescence signals were mainly from the L edges of the Ag substrate and M edges of the Au cover layer and these relatively low energy fluorescence photons were stopped by the 0.64 mm thick plexiglas cap of the total-electron yield detector. In a sense the total-electron detector housing acted as a high pass filter for fluorescence photons. As a result the anomalous dispersion made a very small contribution to the fluorescence signal detected, and its effect was not visible in our data. Calculations show that the distortion in the near edge structure of the 8 ML Cu is about 1% of the edge jump at 10 eV above the first inflection point when $\varphi \sim \varphi_c$, compared with about 20% distortion if all the fluorescence signal were detected. At incident angles $\varphi \leq 0.78\varphi_c$ the data obtained from all three detection methods tend to agree with each other.

According to the calculation in chapter II, when the sample thickness is of the order of 10 ML the distortion in the EXAFS amplitude due to the anomalous dispersion is negligible. This is demonstrated in Fig. 1(d) where the $\chi(k)$'s at the Cu K-edge are plotted for different x-ray incident angles. Clearly, there is no detectable angular dependence of the amplitude of $\chi(k)$ in this case. Therefore we can treat the glancing-incidence XAFS data in the usual fashion. The maximum error caused by the anomalous dispersion in this case is only a few percent. The potential consequence of this and other small effects to the analysis will be addressed later in this chapter.

In this chapter we analyze the fluorescence data, not only because it is almost free from the anomalous dispersion effect but also a relatively simple way of estimating the correction needed in the EXAFS amplitude and phase is available.[8]

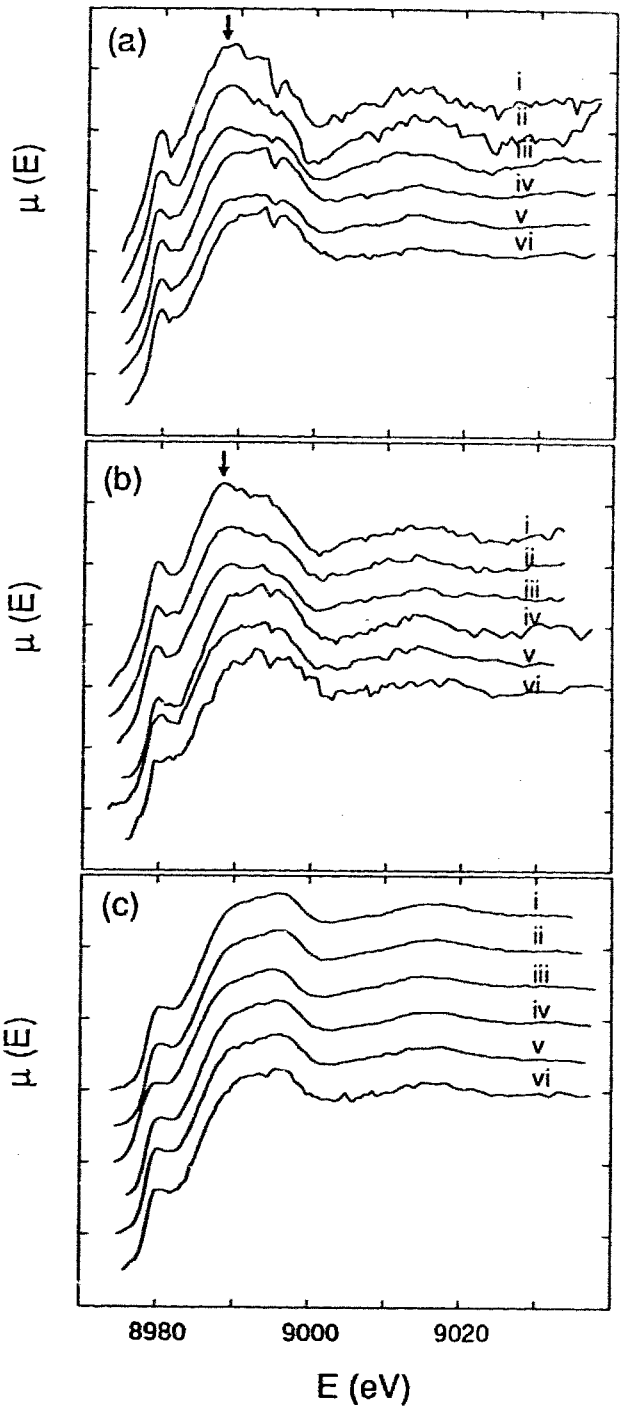

Fig. 1. Anomalous dispersion effect in an ultrathin sample case. (a) XANES by total-electron-yield; (b) XANES by reflectivity and (c) XANES by fluorescence yield. In each panel the x-ray incident angles are: i) $1.11\varphi_c$; ii) φ_c; iii) $0.89\varphi_c$; iv) $0.78\varphi_c$; v) $0.67\varphi_c$ and vi) $0.53\varphi_c$. The arrow-head indicates the region where the systematic angular dependence is most visible. The curves are vertically displaced for clarity.

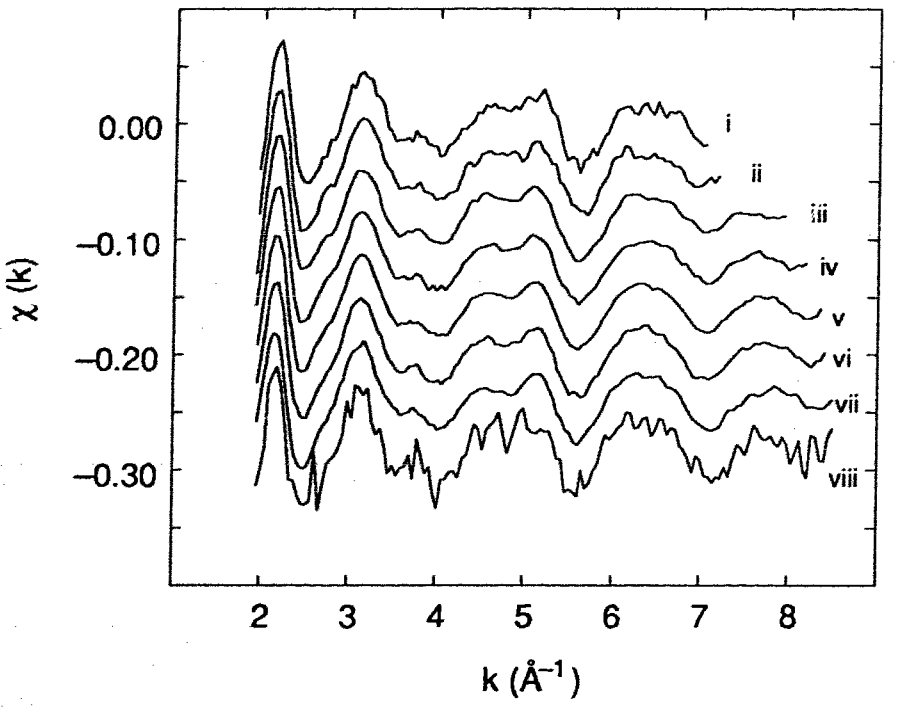

Fig. 1(d). $\chi(k)$ of 8 ML of Cu on Ag(001) at different x-ray incident angles: i) $1.56\varphi_c$; ii) $1.33\varphi_c$; iii) $1.11\varphi_c$; iv) φ_c; v) $0.89\varphi_c$; vi) $0.78\varphi_c$; vii) $0.67\varphi_c$ and viii) $0.53\varphi_c$. Higher angle data are restricted because of the appearance of a Bragg peak. The data acquisition time was different for different incident angles, but generally the data were noisier at high and low ends of the range of incident angle. The curves are vertically displaced for clarity.

The fact that glancing-incidence EXAFS is observable when Cu is covered with a heavier element Au even at incident angles much smaller than the critical angle is noteworthy. In applications of the glancing-incidence EXAFS technique it is normally stated that a buried film or substrate can only be studied at angles less than its critical angle for total reflection, φ_c, if the φ_c of the covering layer is smaller. But this is not valid for thin covering layers. Calculations indicate that experimentally useful penetration into the Cu layer will occur for covering films of Au up to 30 Å thick.

3.2) Results about the Structure of the 8 ML Cu

3.2.1) XANES

The x-ray absorption near edge structure, XANES, of fcc Cu, 8 ML Cu and bcc Fe are plotted in Fig. 2(a). The reference data of fcc Cu and bcc Fe were obtained by the transmission method on pin-hole-free metal foils of thickness 3 μm. The 8 ML Cu data were obtained by averaging the data sets taken in an incident angle range of $0.67\varphi_c \leq \varphi. \leq 0.87\varphi_c$ using fluorescence detection. The 8 ML Cu XANES was prepared by first subtracting a linear fit to the pre-edge background and then normalizing to the linear fit above the edge.

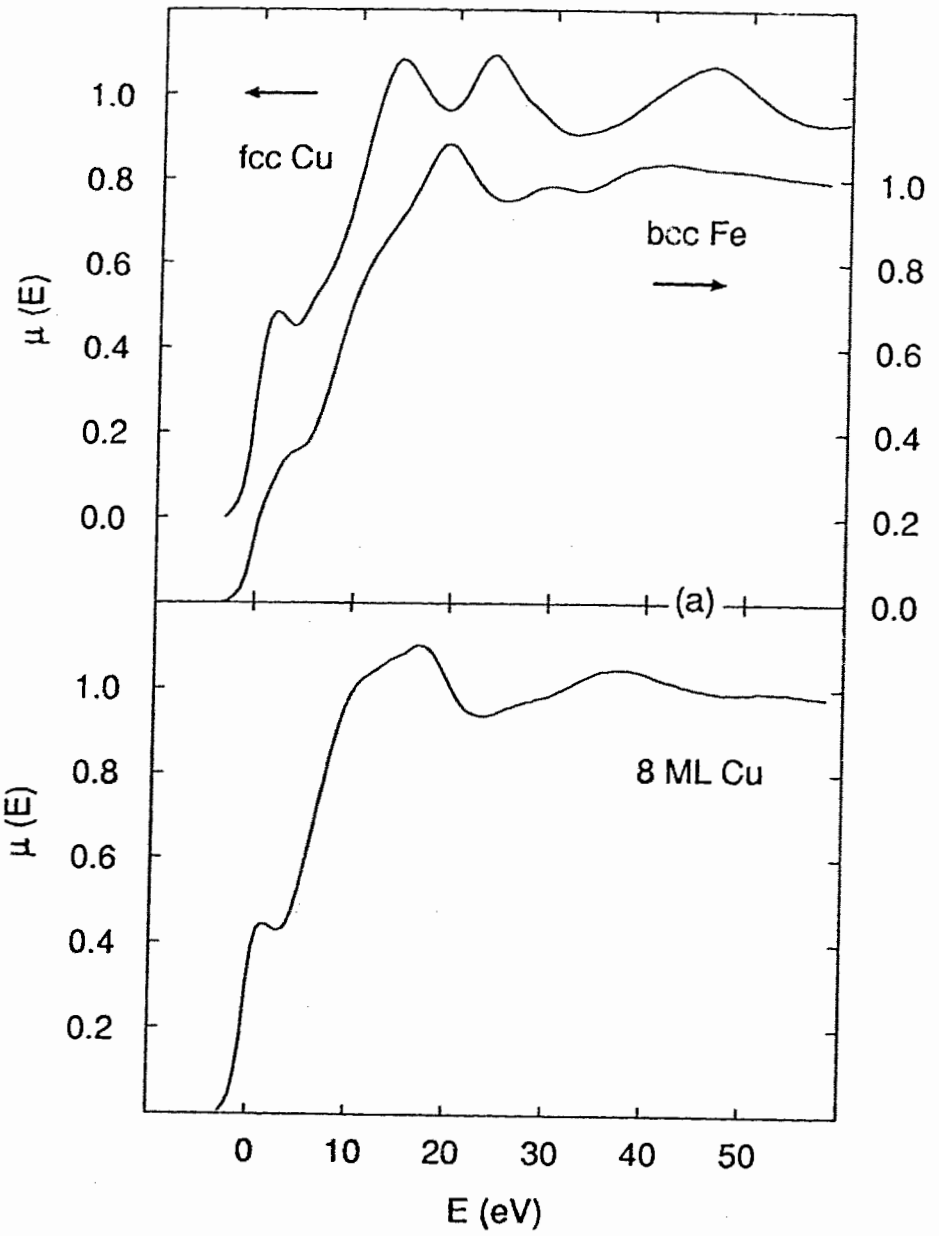

Figure 2.(a) The XANES spectra of the K-edges of bulk samples of fcc Cu, bcc Fe and of Cu in the epitaxially grown system, Au(10ML)/Cu(8ML)/Ag(001). The absorption coefficient μ(E) has been normalized to unity at the edge as per text. The zero of the energy scale coincides with the first inflection point for each edge. The inflection point for the 8 ML Cu is 0.16 eV below that for fcc Cu.

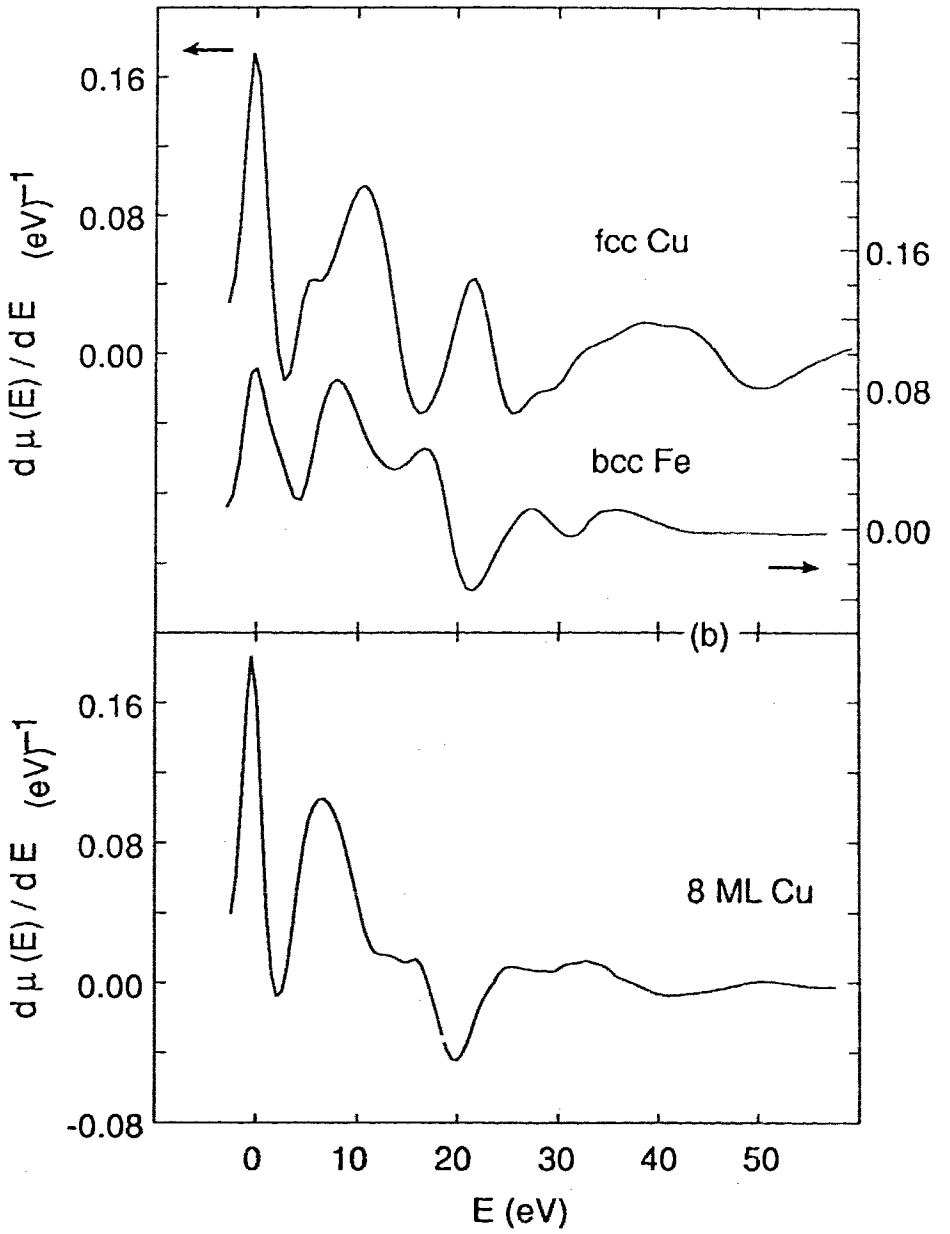

Fig.2(b) The derivative of the XANES spectra of Fig.2(a).

There is a small, but reproducible, shift of the first inflection point of the 8 ML Cu spectrum to 0.16 ± 0.1 eV below that of fcc Cu.

In the XANES of fcc Cu the three peaks in the energy range 0-30 eV have been shown to be well correlated with the positions of energy eigenvalues of X_4', X_5' and L_3' band states.[9] States lying on the Brillouin zone boundary have a high density of states because the bands are flattened and hence correspond to peaks in the absorption spectrum. However, in the XANES of 8 ML Cu in the same energy range the second and third peak in fcc Cu are replaced by one broadened peak and the spectrum is different from that of fcc Cu. On the other hand, the XANES of 8 ML Cu is more similar to that of bcc Fe with respect to peak positions and strengths throughout the XANES energy range. The similarities are more evident in the derivative plots shown in Fig. 2(b).

Based on these observations we expected that the 8 ML Cu could have a structure close to that of bcc Fe. The following EXAFS analysis confirmed this. No quantitative analysis is attempted here on the XANES of the 8 ML Cu. However, this XANES of a Cu crystal completely different from the natural bulk structure should serve as a good test for the first principle theoretical calculations of XANES that have been developed to give agreement with fcc Cu.[10-13]

3.2.2) EXAFS

The $\chi(k)$ shown in Fig. 3 were extracted from the raw data by removing the post-edge background by a polynomial fit and normalizing by the edge jump obtained by extrapolation of linear fits in a range about 30 eV to 130 eV above the edge. Since the $\chi(k)$ of the 8 ML Cu was eventually curve fitted using empirical amplitude and phase shifts from fcc Cu, a McMaster correction for the energy dependence of the background was not applied.[14] The $\chi(k)$ of 8 ML Cu is limited to the range shown because of the existence of a Bragg peak at 9 $Å^{-1}$.

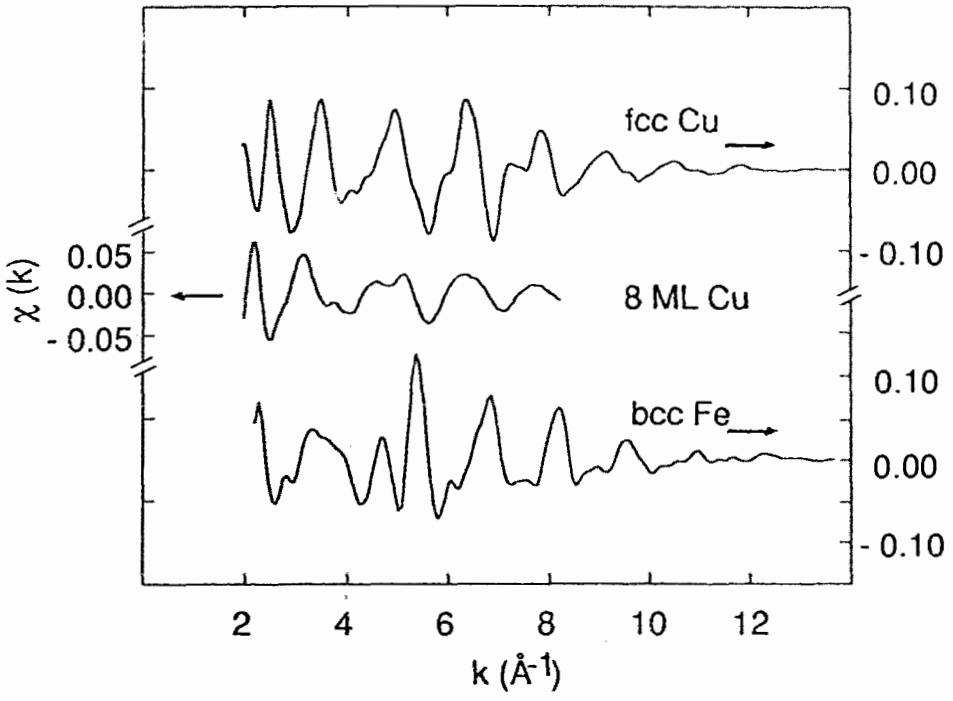

Figure 3. The EXAFS interference functions $\chi(k)$ of fcc Cu, bcc Fe and the 8 ML of Cu grown on Ag(001).

The Fourier transforms of $k\chi(k)$ are shown in Fig. 4 using the limited range of the 8 ML Cu data. In the insets of Fig. 4 are shown the transforms of the reference data using a larger *k*-space range. The transforms of 8 ML Cu and bcc Fe show two peaks in the range 1.5Å ~ 3Å with a different degree of separation, while the transform of fcc Cu in this range is different. Although one can not directly assign two atomic shells to the two peaks, it is plausible that there is more than one shell in 8 ML Cu. There is a big difference between the transforms of 8 ML Cu and bcc Fe in the range 4Å ~ 5Å. In this range the transform of the bcc Fe is determined by the fourth and fifth nearest neighbors. The fifth nearest neighbor is on the body-center diagonal site; focussed multiple scattering makes the peak in the transform extraordinarily high (see the inset). The strong damping of this feature in the transform of 8 ML Cu indicates again the deviation from a regular bcc structure.

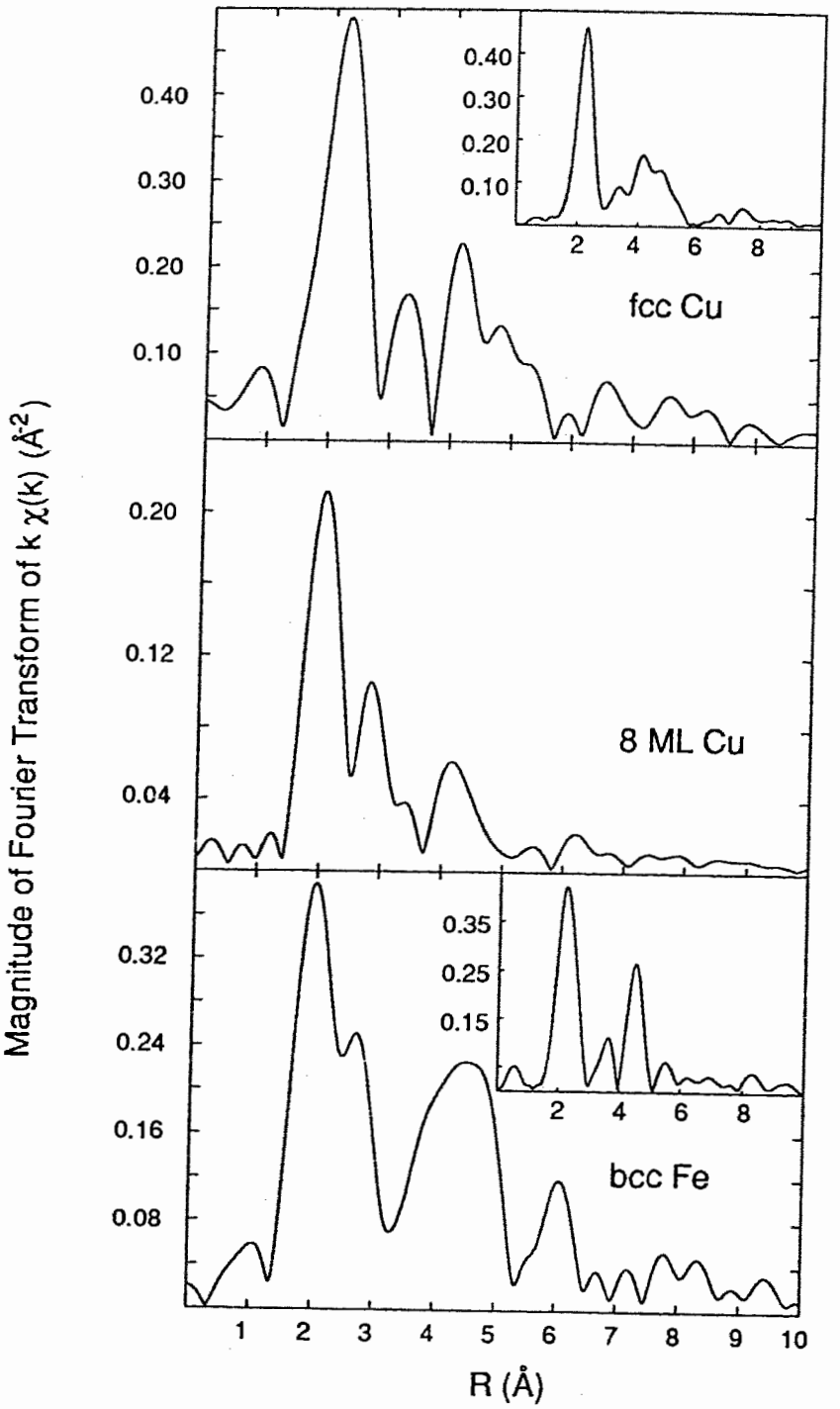

Figure 4. The magnitude of the Fourier transform of $k\chi(k)$ for fcc Cu (top), 8 ML of Cu (middle) and bcc Fe (bottom). The $\chi(k)$ of Fig.3 were transformed over the range $2.3 < k < 8.0$ Å^{-1} using a rectangular window function. The insets show the magnitudes of the Fourier transforms with $k_{max} = 15$ Å^{-1} and a 10% Gaussian window.

VI.4) Data analysis

4.1) Beating analysis

When a large k-range $\chi(k)$ is available, the beating analysis can quantitatively determine[15] ΔR as we have already shown in section II.2.2.3. To indicate the accuracy with which ΔR can be determined, we consider the case of bcc Fe. In bcc Fe the distance difference between the first two shells is $\Delta R = 0.385$ Å.[16] Using a Fourier transform with a k-space transform range of 2 ~ 16 Å^{-1} and a R-space back-transform range of 1.42 ~ 3.07 Å, the first order beat node was determined consistently in both the amplitude and phase derivative to be $k_1 = 4.05 \pm 0.04$ Å^{-1}, where the error bar was estimated by changing the ranges of the transform windows. Using $k_1 \Delta R = \pi/2$, we get $\Delta R = 0.388 \pm 0.004$ Å, i.e., an error less than 0.01 Å compared to the exact value.

In the case of the 8 ML Cu film, the k-space data range is limited to about 8 Å^{-1} and consequently the first two shells are not well separated from higher shells in the transform. When Fourier filtering is applied, the transform artifacts and the correlation between the beat node position and quantities like coordination numbers and Debye-Waller factors start to have noticeable effects on the value determined for the beat node. Tests of using the beating analysis on the bcc Fe data over the restricted k-space data range showed that the error in ΔR could be as much as 0.03 Å depending on the details of the transform procedures. However, if the analysis is applied to the 8 ML Cu and bcc Fe in a systematic way, comparison provides structural information which then can be used as a guideline for a detailed modeling and, permits one to check the consistency of results from different analysis techniques.

Using a rectangular window the Fourier transform of $k\chi(k)$ (Fig.4) of the 8 ML Cu between 1.38 Å and 3.35 Å was Fourier filtered and the amplitude and phase were extracted. Fig.5 shows the results for the derivative of the phase as a function of k. For comparison the results for bcc Fe and fcc Cu, prepared in the same manner, are also

shown. The strong beating effect in both bcc Fe and the 8 ML Cu are clearly evident, i.e. similar to bcc Fe the first and second shells of the 8 ML Cu have a small separation. The gradual modification in the low k part of the derivative of the phase of fcc Cu is probably due to transform artifacts. For the 8 ML Cu the beating node is at 4.52 Å^{-1}; by applying $k\Delta R = \pi/2$ we have $\Delta R^{Cu} = 0.348$ Å. Similarly for bcc Fe the node is at 4.25 Å^{-1}, giving $\Delta R^{Fe} = 0.370$ Å, which is 0.015 Å shorter than the exact value. Due to the limited resolution these numbers depend on the details of the transforms, however the relative beating node separation is meaningful. In Fig.5 it also can be seen that the depth of the dip in the phase derivative of 8 ML Cu is much smaller than that of bcc Fe. From a detailed modeling study, in which $\chi(k)$ was constructed from equation (II-3a), we conclude that the smaller depth of the dip for the Cu is mainly due to a decrease in N_2/N_1 and an increase in $\sigma_2^2 - \sigma_1^2$. The mean free path is not important here.

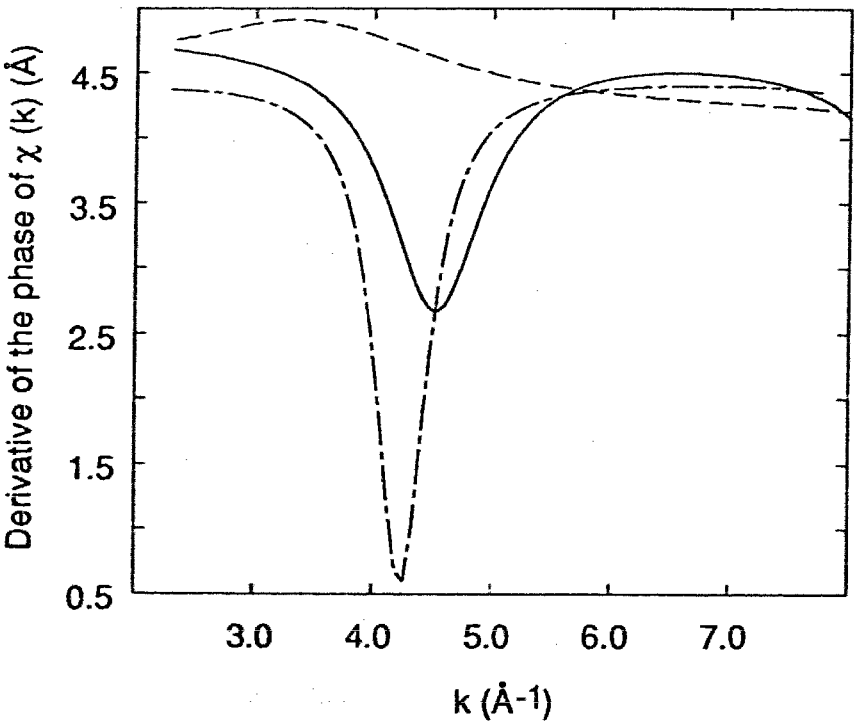

Figure 5. The phase derivatives of the 8 ML Cu (solid), bcc Fe (dash dot) and fcc Cu (dash).

Qualitatively the above beating analysis provide us with the following facts: the 8 ML Cu has a structure somewhat similar to a body-centered one, the bond length difference between the first two coordination shells is shorter than that in bcc Fe and the quantity $\frac{N_2}{N_1}$ $e^{-(\sigma_2^2 - \sigma_1^2)}$ of 8 ML Cu is smaller than that of bcc Fe. These are the constraints for the model-dependent analysis discussed in the following.

4.2) Curve-fitting

To solve the structure quantitatively we applied a non-linear least squares curve fitting. The empirical Cu scattering amplitude and phase were extracted from bulk transmission data using the conventional Fourier filtering technique. The directly extracted empirical EXAFS amplitude function was $\frac{1}{kR_1^2} N_1 S_o^2 f(k) e^{-2\sigma^2 k^2} e^{-2R_1/\lambda}$ which was multiplied by kR_1^2/N_1 to get the effective atomic scattering amplitude $S_o^2 f(k) e^{-2\sigma^2 k^2} e^{-2R_1/\lambda}$. The R_1 and N_1 used for fcc Cu were 2.556 Å and 12.[16] This means that we neglected any possible differences between the values for S_o^2 and λ in bulk and in the thin film state. The ΔE_0 was always fixed at 0.

The $k^3\chi(k)$ (2.85 Å ≤ k ≤ 7.42 Å) of 8 ML Cu was Fourier transformed using a 10% Gaussian window and the curve fitting was applied to its Fourier transform in R-space within the range 0.8 Å ≤ R ≤ 2.8 Å. Four parameters were varied: the nearest and the second nearest neighbor bond lengths, R_1 and R_2, and the corresponding mean-squared-relative displacements σ_1^2 and σ_2^2. The result is listed in TABLE I where $\Delta\sigma_i^2 = \sigma_{i\ 8ML\ Cu}^2 - \sigma_{fcc\ Cu}^2$. The error bars are defined in the same way as discussed in chapter V.

TABLE.I. Results of fitting the Cu K-edge EXAFS spectrum. Fixed parameters: $\Delta E_0 = 0$, $N_1 = 8$, $N_2/N_1 = 0.75$.

R_1 (Å)	$\Delta\sigma_1^2$ (10^{-3} Å^2)	R_2 (Å)	$\Delta\sigma_2^2$ (10^{-3} Å^2)
2.56±0.02	1.8±2.7	2.88±0.036	$5.8^{+6.0}_{-4.7}$

The coordination numbers were fixed to reduce the inter-correlation between floating parameters to an acceptable level. The values of N_1 and N_2 in Table I are those for a perfect bcc structure. The results of R_1 and R_2 were not sensitive to the changes in N or σ^2: varying N_1 between 7 and 8 and N_2/N_1 between 0.60 and 0.75 gave essentially the same results for the R's. When all the parameters were allowed to float the results for the bond lengths remained within the error bars quoted in TABLE I., but the residual sum of squares was two or three times larger.

Fig.6 shows the the magnitude and the imaginary part of the Fourier transform of $k^3\chi(k)$ of the 8 ML Cu and the fit using the parameters in Table I. The vertical dash line at 2.8 Å in the graph indicates the upper bound of the fitting range. Beyond this line the effect of multiple scattering from the nearest neighbor triangular path becomes appreciable and is not included in our single scattering approximation.

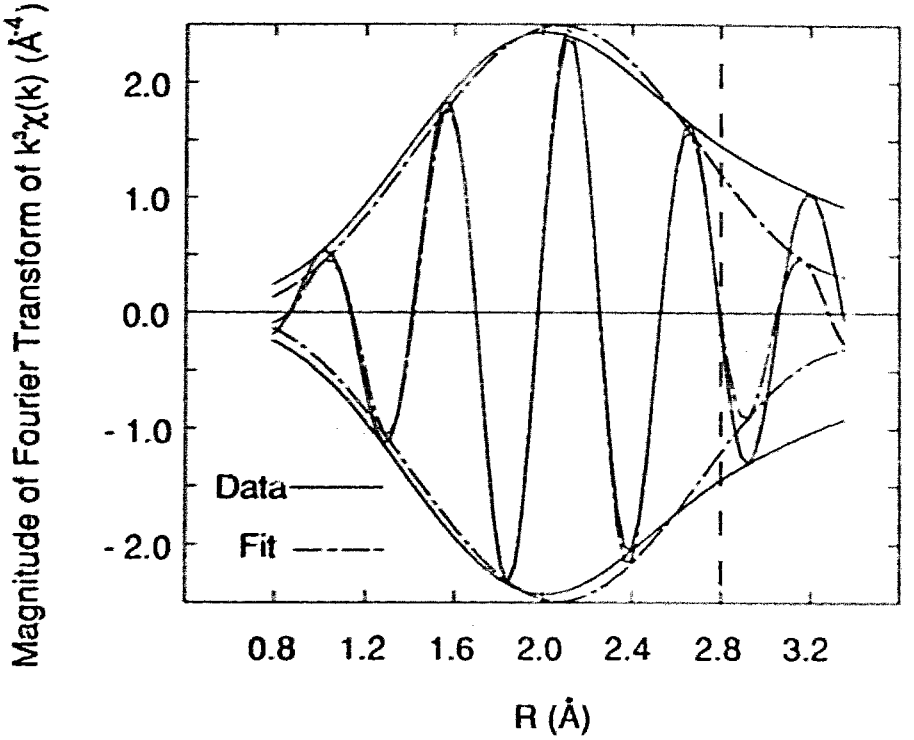

Figure 6. R-space curve fitting of 8 ML Cu. The vertical dash line at 2.8 Å indicates the upper limit of the fitting range, above which the contribution of multiple scattering from the nearest neighbor triangular path is significant.

As can be seen from TABLE 1, the difference between the two shells is 0.32 ± 0.04 Å, which is consistent with the result of 0.348 Å obtained from the beating analysis discussed earlier.

In our experimental arrangement the polarization direction of the incoming synchrotron radiation was parallel to the (001) surface of the sample. For a perfect cubic structure there is no polarization dependence in the spectrum.[17] However, it will be shown in the next section that the results in Table I lead to a tetrangonal structure with its *c* axis along the sample surface normal. This departure away from a perfect bcc structure makes the angle between the first nearest neighbor bond and the (001) surface normal to be 52.74° which is about 2° less than the magic angle[18] in a bcc case. Using the formulae in

Ref. 19, reductions in the effective coordination numbers for the first and second shells are calculated to be 5% and 0% respectively. Besides the polarization effect the residual anomalous dispersion effect will also cause a reduction in the effective coordination number, and in addition, a small constant EXAFS phase shift. It can be shown that the effect becomes less important as the film becomes thinner. In our particular case of 8 ML Cu, the effective coordination number reduction is only about 3% when $\varphi < \varphi_c$ and the additional constant phase shift is less than 0.06 rad for any incident angle. Both the amplitude and phase corrections are practically independent of photon energy in the EXAFS range. With these amplitude and phase corrections implemented, the fitting result for R_1, R_2 and the residual sum of squares essentially remain the same as the values in Table I, but $\Delta\sigma_1^2$ and $\Delta\sigma_2^2$ are changed to $0.5\text{x}10^{-3}$ and $6.5\text{x}10^{-3}$ respectively.

VI.5) Discussion

The fcc Ag (001) surface rotated 45° can be viewed as a primitive square lattice with a transverse lattice constant $a_{Ag}/\sqrt{2} = 2.89$ Å, where $a_{Ag} = 4.09$ Å is the lattice constant of fcc Ag. It is known from the RHEED study that the transverse lattice in the Cu film has a four-fold symmetry and has a transverse lattice constant very close to that of the square Ag atom array.[3] To minimize the surface free energy the logical sites for the first monolayer Cu atoms are the four-fold symmetry hollow sites in the center of the square cornered by four Ag atoms which are the minima of the substrate-induced periodic potential. For the same reason, the second and the following Cu layers should also grow on the four-fold symmetry sites. This process leads us to have either body-centered cubic or face-centered cubic or tetragonal lattices which depend only on the length of the lattice constant c along the surface normal direction. If c equals the transverse lattice constant, a', the structure is bcc, if $c = \sqrt{2}\,a'$, it is fcc, and in all the other cases it is tetragonal. In our experiment the polarized incident synchrotron radiation had its electric vector parallel to the sample surface,

so the bonds of length $R = c$ in the normal direction were not detected. Therefore there was no need to include another shell very close to the second nearest neighbor in the fitting. The second nearest neighbor distance R_2 =2.88Å then is equal to the transverse lattice constant a'. Although this square lattice has a 20% lattice mismatch with fcc Cu (lattice constant[16] $a_{Cu} = 3.615$ Å), the lateral atomic registry on the Ag surface is conserved. In this regard the EXAFS result essentially agrees with that from RHEED. The vertical lattice constant in a body-centered tetragonal is $c = (4R_1^2 - 2R_2^2)^{1/2}$. From the data in TABLE I. we have $c = 3.10 \pm 0.09$ Å, where the error bar is deduced from those of R_1 and R_2. So based on the fitting analysis we conclude that the 8 ML Cu has a body-centered tetragonal lattice with $c/a = 1.076 \pm 0.043$, i.e. it is (7.6 ± 4.3)% expanded from a bcc structure along the surface normal direction. The error bars were estimated conservatively and represent an overestimate (see discussions in chapter V).

To this point our structural conclusions are based only on EXAFS data. If we assume the transverse lattice constant of 2.90 Å as measured with RHEED and assume a bcc structure, then the nearest neighbor distance would be 2.515 Å which is significantly smaller than the value $R_1 = 2.56 \pm 0.02$ Å determined from EXAFS. The value of R_1 in bct is the same as in fcc Cu ($R_1 = 2.556$ Å), but the atomic volume for bct is 9% larger than for fcc Cu.

Using XPD Egelhoff and Jacob reported that the vertical expansion of Cu on Ag(001) surface is about 4%.[5] The sample in the XPD study had 6.5 ML Cu on Ag(001) and no covering material on top of it. It has been observed that around 8 ML during the growth the LEED became slightly smeared.[20] The expansion obtained by the glancing-incidence EXAFS is somewhat larger. This may be due to differences between the samples studied.

Since the glancing-incidence XAFS technique averages over all of the Cu atoms in the sample and the growth of Cu on Ag is not thermodynamically favorable (the surface-free-energy of Cu is slightly higher than that of Ag[21]), the possibility of interdiffusion at the interfaces must be considered. If during the growth of the first few monolayers of Cu on

the Ag the adsorbed atoms were agglomerated or intermixed with the substrate atoms, the RHEED intensity oscillations would not start from the first monolayer deposited.[22, 23] However for the sample used in this study the RHEED intensity oscillations were observed from the beginning to the end of the growth of Cu layers. A similar structure of Cu epitaxially grown on Ag(001) has been studied by XPD,[5] which is an effective technique for detecting surface alloying or interdiffusion:[24, 25] no interdiffusion was reported. For the interface between the Au cover layer and the Cu film the intermixing of the two elements is more unlikely. This growth is thermodynamically favorable from the surface-free-energy point of view and the result from a photoemission study on a Au/Cu(bulk polycrystal) interface indicates that no interdiffusion is observed.[26] This is supported by our RHEED measurements during the growth of the Au overlayer. Cu grows in a simple square lattice while Au shows a complex reconstruction corresponding to a corrugated (111) surface layer of epitaxial Au(001). It is expected that intermixing would affect the characteristic reconstruction of Au. Since the reconstruction was not affected it seems that the interdiffusion is unlikely.

To assess the sensitivity of EXAFS to interdiffusion we have considered two models for the EXAFS interference function $\chi(k)$. The first model assumed a perfect epitaxial structure Au(001)/8 ML of bct Cu/Ag(001). In this case, the Cu in the bottom layer has 4 Ag atoms as nearest neighbors and 4 n.n. Cu and the Cu in the top layer has 4 Au n.n. and 4 Cu n.n. Averaging over the 8 ML of Cu, the effective n.n. coordination of Cu becomes 7.0 Cu, 0.5 Au and 0.5 Ag. The second model assumed diffusion occurs with the top and bottom layer of Cu interchanging completely with the interfacial Au and Ag layers respectively, without altering the structure or lattice parameters. The effective n.n. coordination number for Cu becomes 5 Cu, 1.5 Au and 1.5 Ag. Both model $\chi(k)$ were fitted under the assumption that the Cu has only Cu atoms as nearest neighbors. The second model gave a χ^2, residual sum of errors, that was a factor of five larger than for the first model and could be safely rejected. However it would be difficult to distinguish the

first model from the case in which Cu had only Cu as nearest neighbors. Based on these discussions we rule out the possibility of severe interdiffusion in our sample.

Our study of the 8 ML Cu film is relevant to the magnetic behavior of Fe/Cu/Fe trilayers on Ag(001). Heinrich has shown that the exchange coupling depends on the thickness of the Cu interlayer, changing from ferromagnetic to antiferromagnetic for greater than 8 ML of Cu.[3] Recently an *ab initio* calculation was carried out by Herman, Sticht and Schilfgaarde on the magnetic properties of Fe/Cu superlattices assuming a perfect bcc Cu in the film and the result did not reproduce the sign change in the magnetic coupling between Fe layers with different Cu layer thickness.[6] It would be quite interesting to see whether the tetragonal model suggested in this study can provide some further clue for the understanding of the physical mechanism of the oscillatory magnetic coupling.

In conclusion, we have applied glancing-incidence XAFS to a buried single crystal Cu film only 8 monolayers thick. It is demonstrated that when the top passive layer is a heavier element, but thin (10 ML in this case), the glancing-incidence technique is still applicable. When the film of interest has a thickness of a few monolayers like the case here, the anomalous dispersion effects in fluorescence yield can be eliminated by filtering out the signal from the substrate and the covering layer. This makes it possible to get practically distortion free XANES without complicated data processing which would need detailed knowledge of the optical parameters of every layer. The XANES obtained for the novel Cu structure is strikingly different from that for normal fcc Cu. This XANES of a Cu crystal completely different from the natural bulk structure should serve as a good test for the first principle theoretical calculations of XANES of Cu metal.

From detailed EXAFS analysis, we conclude that the structure of the 8 ML Cu film is body centered tetragonal with lattice constants $a = 2.88$ Å and $c = 3.10$ Å, with the c-axis (perpendicular to the substrate) being expanded 7.6% relative to the bcc structure.

Chapter VII Summary and Outlook

In the work of this thesis we have successfully applied glancing-incidence XAFS spectroscopy to structural studies of ultrathin metastable metallic Ni and Cu films on Fe(001) and Ag(001) surfaces respectively.

From the technical view point, we have investigated the interpretation of the XAFS data for the epitaxial systems obtained in glancing-incidence in different sample thickness situations and compared different detection mechanisms under the same experimental conditions. We found that in the ultrathin film limit (< 10 ML) the EXAFS spectrum obtained in the glancing-incidence mode is virtually distortion free and the distortion in XANES can be virtually eliminated by energy discrimination of the detected signal.

The ultrathin Ni/Fe(001) and Cu/Ag(001) systems were found to possess interesting structural and magnetic properties.[1,2] In this work the local structures of these systems were characterized for the first time. For the Ni/Fe(001) epitaxial systems studied in this work, we have determined the local structure of the novel Ni overlayers on Fe(001) in both the stabilized state (e.g. 37 ML) and the transition state (e.g. 9 ML): in the stabilized state the Ni overlayers have a local structure almost identical to that of fcc Ni metal while in the transition state the Ni overlayers have a local structure distinctly different from either the bcc or fcc structure but with an average atomic volume close to that of bcc Fe. These results indicate that the microscopic origin of the magnetic properties has to be related to a defect-induced model because once the Ni thickness passes the critical region (3-6 ML) the structure is definitely not bcc. The local structural parameters of Ni/Fe(001) obtained in this work will serve as strong constraints in any further modeling of the entire structure which is essential for thorough understandings of the magnetic properties of this system.

In the other system we have studied, Cu(8ML)/Ag(001), by combining the information from RHEED and glancing-incidence XAFS we have determined the structure

to be bct with the *c* axis (perpendicular to the substrate) being expanded 7.6% relative to the *a* axis. This result may be helpful in unravelling the difficulties encountered in understanding theoretically the role played by the Cu layers in the magnetic couplings in Fe/Cu/Fe trilayers on Ag(001). An initial first principles calculation carried out by Herman *et. al.*[3] showed that in an Fe/Cu superlattice with Cu having a bcc structure the exchange coupling between successive Fe slabs does not exhibit the ferromagnetic to antiferromagnetic crossover observed experimentally at about 9 ML of Cu. With improved numerical accuracy the same calculation indicated that the exchange coupling indeed switches from ferromagnetic to antiferromagnetic, but the corresponding crossover Cu thickness was far smaller than the experimentally observed value. The large structural distortion in the Cu structure found in this work (*c/a* deviates by 7.6% from unity) can have drastic effects on the detailed shape of the Fermi surface and on the density of states at the Fermi level, even tilting the balance from ferromagnetic to antiferromagnetic coupling at some Cu spacer thickness.[3]

The above results indicate to some degree both the power and the limitation of applying the glancing-incidence XAFS to ultrathin epitaxial systems. The technique provides an efficient (due to the surface sensitivity warranted by the glancing-incidence technique) and nonambiguous (due to the element selectivity of XAFS) identification of local structure of the element of interest which can be used to distinguish different crystal structural models proposed for the system. Contrasted to the electron-detection based surface structural tools (where normally only the top few monolayers are sampled) and the diffraction-based tools (where the coherent parts of the signal are dominant), glancing-incidence XAFS samples together virtually *all* the atoms of the element of interest in such ultrathin epitaxial systems. Another advantage of glancing-incidence XAFS over the conventional surface tools like RHEED and LEED is that the buried layers can be studied without extra difficulties. In an analogy to the fact that the overlayer structure can be "defined" by the substrate template, it is also possible that the epitaxial covering layers on

the top will also modify the sample structure to a certain extent. In such cases the structural study using glancing-incidence XAFS is truly *in situ*. The limitation of the technique lies upon the fact that by the local structure information alone it is not enough to characterize thoroughly the structural properties of such systems.

The work in this thesis represents one of the first attempts of applying the XAFS on metastable epitaxial metallic layers. There is still a great deal of the potential capability of the glancing-incidence XAFS technique to be explored. For example, all the results presented in this work were obtained with the electric vector of the synchrotron radiation parallel with the sample surface, which means that the vertical interplanar distances could only be deduced indirectly. Using the available sample positioning apparatus described in chapter III, an experiment with the electric vector perpendicular to the sample surface can be performed. The results obtained in this sample orientation would greatly increase the accuracy of the interplanar distance determination. When the system does not have a cubic symmetry, this piece of information will be very helpful in understanding the structure. To correlate the structural changes in different thicknesses of the epitaxial overlayers with the continuous modulation of the magnetic properties of the system, a structural study on a series of samples with different Ni thicknesses ought to be conducted. With the realization that the glancing-incidence XAFS technique can be applied on a system with a heavier element grown on top, many more novel structures (for example the interesting Pd/Fe(001)bilayers on Ag(001)[4]) can now be characterized by this technique.

Another rich field to be explored is to have detailed understanding of the XANES of the epitaxial phases obtained by the glancing-incidence XAFS technique. XANES can provide valuable information about the electronic and structural properties of the epitaxial phases. As mentioned above, the additional complexity of the XANES obtained in the glancing-incidence mode can be virtually eliminated in the ultrathin film cases. This reduces the question to interpreting an ordinary XANES spectrum. But, up to this time, the interpretation of an XANES spectrum is still an involved task. To this end, the XANES of

the new phases obtained by the glancing-incidence technique should serve as good tests for the first-principles theoretical calculations (e.g. the XANES of the bct Cu discussed in chapter VI).

With a synchrotron radiation source, one can jointly apply glancing-incidence x-ray diffraction and glancing-incidence XAFS on the epitaxial layers. This combined technique may be able to provide the ultimate structural characterization of a complex epitaxial system such as the Ni(>6ML)/Fe(001).

References

Chapter I

1. M.N. Baibich, *et al.*, Phys. Rev. Lett. **61**, 2472(1988).
2. B. Heinrich, *et al.*, Appl. Phys. A **49**, 473(1989).
3. J.J. Krebs, P. Lubitz, A. Chaiken , and G.A. Prinz, Phys. Rev. Lett. **63**, 1645(1989).
4. B. Heinrich, *et al.*, Phys. Rev. Lett. **64**, 673(1990).
5. Z. Celinski, *et al.*, Phys. Rev. Lett. **65**, 1156(1990).
6. S.T. Purcell, A.S. Arrott , and B. Heinrich, J. Vac. Sci. Technol. B **6**, 794(1988).
7. E. Bauer, in *Techniques of Metals Research* (eds. Bunshah, R.F.), Reflection Electron Diffraction, 502 (Wiley Interscience, New York, 1969).
8. see for example: W.F. Egelhoff Jr., CRC Crit. Rev. Solid State Mater. Sci. **16**, 3(1990).
9. W.F. Egelhoff Jr., I. Jacob, J.M. Rudd, J.F. Cochran , and B. Heinrich, J. Vac. Sci. Technol. A **8**, 1582(1990).
10. W.F. Egelhoff Jr., Phys. Rev. Lett. **59**, 559(1987).
11. Z.Q. Wang, Y.S. Li, F. Jona , and P.M. Marcus, Solie State Comm. **61**, 623-626(1987).
12. P.M. Marcus, V.L. Moruzzi, Z.Q. Wang, Y.S. Li , and F. Jona, (preprint).
13. H. Li, *et al.*, Phys. Rev. B (Rapid Comm.) **42**, 9195(1990).
14. H. Li, D. Tian, J. Quinn, Y.S. Li , and F. Jona, Phys. Rev. B **43**, 6342(1991).
15. H. Li, *et al.*, Phys. Rev. B (Rapid Comm.) **44**, 1438(1991).
16. I.K. Robinson, Phys. Rev. Lett. **50**, 1145(1983).
17. I.K. Robinson, in *The Structure of Surfaces* (eds. Van Hove, M.A. & Tong, S.Y.), (Springer, New York, 1984).
18. J. Bohr, *et al.*, Phys. Rev. Lett. 1275(1985).
19. P.H. Fuoss, *et al.*, Phys. Rev. Lett. 2389(1989).
20. M. Sauvage-Simkin, *et al.*, Surf. Sci. **211/212**, 39(1989).
21. D.T. Jiang, N. Alberding, A.J. Seary , and E.D. Crozier, J. Phys. (Paris) Colloq. **47**, C8-825(1986).

22. Y.U. Idzerda, W.T. Elam, B.T. Jonker , and G.A. Prinz, Phys. Rev. Lett. **62**, 2480(1989).

23. D.T. Jiang, N. Alberding, A.J. Seary, B. Heinrich , and E.D. Crozier, Physica B **158**, 662(1989).

24. Y.U. Idzerda, W.T. Elam, B.T. Jonker , and G.A. Prinz, J. Appl. Phys. **67**, 5385(1990).

25. H. Oyanagi, *et al.*, Physica B **158**, 694(1989).

26. H. Magnan, D. Chandesris, B. Villette, O. Heckmann , and J. Lecante, Phys. Rev. Lett. **67**, 859(1991).

27. D.T. Jiang, E.D. Crozier , and B. Heinrich, Phys. Rev. B **44**, 6401(1991).

28. S.M. Durbin, L.E. Berman, B.W. Batterman, M.B. Brodsky , and H.C. Hamaker, Phys. Rev. B **37**, 6672(1988).

29. D.T. Jiang and E.D. Crozier, Nucl. Instru. A **294**, 666(1990).

30. S.M. Heald, H. Chen , and J.M. Tranquada, Phys. Rev. B **38**, 1016(1988).

31. L.G. Parratt, Phys. Rev. **95**, 359(1954).

32. H. Kiessig, Ann. Phys. Lpz. **10**, 729(1931).

33. D.T. Cromer and D. Liberman, J. Chem. Phys. **53**, 1891(1970).

34. D.T. Cromer and D. Liberman, Acta. Cryst. A **31**, 267(1981).

35. D.T. Cromer, J. Appl. Cryst. **16**, 437(1983).

36. B. Heinrich, *et al.*, Mat. Res. Soc. Symp. Proc. Vol. **151**, 177(1989).

37. B. Heinrich, *et al.*, in *Thin Film Growth Techniques for Low-Dimensional Structures* (eds. Farrow, R.F.C., Parkin, S.S.P., Dobson, P.J., Neave, J.H. & Arrott, A.S.), Epitaxial Growths and surface science techniques applied to the case of Ni overlayers on single crystal Fe(001), (Plenum Publishing Corp., 1987).

38. F. Herman, J. Sticht , and M. Van Schilfgaarde, J. Appl. Phys. **69**, 4783(1991).

Chapter II

1. see for example: E.A. Stern, in *X-Ray Absorption: Principles, Applications, Techniques of EXAFS, SEXAFS and XANES* (eds. Koningsberger, D.C. & Prins, R.), Chapter 1, p.13 (JOHN WILEY & SONS, 1988).

2. P.J. Durham, in *X-Ray Absorption, Principles, Applications, Techniques of EXAFS, SEXAFS and XANES* (eds. Koningsberger, D.C. & Prins, R.), Theory of XANES, (Wiley, New York, 1988).

3. see for example: E.A. Stern, in *X-Ray Absorption: Principles, Applications, Techniques of EXAFS, SEXAFS and XANES* (eds. Koningsberger, D.C. & Prins, R.), Chapter 1, (JOHN WILEY & SONS, 1988). Note: formula (47a).

4. G. Bunker, Nucl. Instru. **207**, 437(1983).

5. A.G. McKale, G.S. Knapp , and S.K. Chan, Phys. Rev. B 841(1986).

6. A.G. McKale, B.W. Veal, A.P. Paulikas, S.K. Chan , and G.S. Knapp, J. Am. Chem. Soc. **110**, 3763(1988).

7. see for example: P.A. Lee, P.H. Citrin, P. Eisenberger , and B.M. Kincaid, Rev. Mod. Phys. **53**, p.769-806(1981).

8. For a derivation by a physically sound but elementary argument (classical discussion) see for example: J.D. Jackson, *Classical Electrodynamics* , 6th ed., Section 7.5, p.285 (John Wiley & Sons, 1975).

9. for a clear but sketchy quantum mechanics derivation see: J.M. Ziman, *Principles of the Theory of Solids* , 2nd ed., Section 8.2, p.261 (Cambridge University Press, 1972).

10. for a thorough semi-classical discussion see for example: R.W. James, *The Optical Principles of the Diffraction of X-rays* , Chapter IV (G. Bell and Sons, London, 1965).

11. see for example: J. Wooten, *Optical Properites of Solids* , p.71.

12. R.W. James, *The Optical Principles of the Diffraction of X-rays* , Chapter III, p.109 and 114(3.47) (G. Bell and Sons, London, 1965).

13. R.W. James, *The Optical Principles of the Diffraction of X-rays* , Chapter IV, p.145-146 (G. Bell and Sons, London, 1965).

14. D.T. Cromer and D. Liberman, J. Chem. Phys. **53**, 1891(1970).

15. D.T. Cromer and D. Liberman, Acta. Cryst. A **31**, 267(1981).

16. D.T. Cromer, J. Appl. Cryst. **16**, 437(1983).

17. L.G. Parratt, Phys. Rev. **95**, 359(1954).

18. J.D. Jackson, *Classical Electrodynamics* , 6th ed., Equation (7.34), p.279 (John Wiley & Sons, 1975).

19. M. Born , and E. Wolf, *Principles of Optics* , 3rd ed., p.615 (Pergamon Press, 1965). Note: the form of Snell's law still holds in the absorbing medium once the complex refraction index is introduced.

20. If one wonders how to explain the energy conservation in this phenomenon, the relevant discussion can be found in: M. Born and E. Wolf, *Principles of Optics* , 6th ed., p.49 and references therein (Pergamon Press, 1980).

21. CRC, *CRC Handbook of Chemistry and Physics* , 70th ed., p. E-197 (CRC Press, 1990). Note: in the case of Ni, Z ~ 28, the relative transition probablility $K\beta/K\alpha$ ~ 0.135, then in terms of energy the estimated intensity ratio is 17.3%.

22. J. Stohr, in *X-Ray Absorption: Principles, Applications, Techniques of EXAFS, SEXAFS and XANES* (eds. Koningsberger, D.C. & Prins, R.), Chapter 10, (JOHN WILEY & SONS, 1988).

23. R.B. Greegor, F.W. Lytle , and D.R. Sandstrom, SSRL Report 80/01 p.VII-50(1980).

24. W. Bambynek, *et al.*, Rev. Mod. Phys. **44**, 716(1972).

25. S.M. Heald, in *X-ray Absorption: Principles, Application, Techniques of EXAFS, SEXAFS and XANES* (eds. Koningsberger, D.C. & Prins, R.), Chapter 3, pp. 113, (John Wiley, New York, 1988).

26. M. Born and E. Wolf, *Principles of Optics* , 6th ed., p.614 (Pergamon Press, 1980).

27. J.D. Jackson, *Classical Electrodynamics* , 6th ed., p.311 (John Wiley & Sons, 1975).

28. W.H. McMaster, N. Kerr Del Grande , and J.H. Mallet, *Compilation of X-ray Cross Sections* , (National Technical Information Service, Springfield, 1969).

29. S.M. Heald, H. Chen , and J.M. Tranquada, Phys. Rev. B **38**, 1016(1988).

30. G. Martens and P. Rabe, J. Phys. C: Solid State Phys. **14**, 1523(1981).

31. M.P. Seah and W.A. Dench, Surf. Interface Anal. **1**, 2(1979).

32. for a summary of earlier works on this see: J. Stohr, in *X-Ray Absorption: Principles, Applications, Techniques of EXAFS, SEXAFS and XANES* (eds. Koningsberger, D.C. & Prins, R.), Chapter 10, p.462 (JOHN WILEY & SONS, 1988).

33. A. Erbil, G.S. Cargill III, R. Frahm , and R.F. Boehme, Phys. Rev. B **37**, 2450(1988).

34. W.T. Elam, J.P. Kirkland, R.A. Neiser , and P.D. Wolf, Phys. Rev. B **38**, 26(1988).

35. F.W. Lytle, D.E. Sayers , and E.A. Stern, Physica B **158**, 701(1988).

36. G. Martens and P. Rabe, Phys. Stat. Sol. (a) **57**, K31(1980).

37. G. Martens and P. Rabe, Phys. Stat. Sol. (a) **58**, 415(1980).

38. G. Martens and P. Rabe, J. Phys. C: Solid State Phys. **13**, L913(1980).

39. J.D. Jackson, *Classical Electrodynamics* , 6th edition, pp. 683-684 (John Wiley & Sons, 1975).

40. S. Pizzini, *et al.*, Rev. Sci. Instrum. **60**, 2525(1988).

41. N.T. Barrett, *et al.*, J. Phys. D. Appl Phys. (UK) **22**, 542(1989).

42. N.T. Barrett, *et al.*, J. Cryst. Growth **94**, 689(1988).

43. H. Chen and S.M. Heald, Physica B **158**, 322(1989).

44. B. Poumellec, R. Cortes, F. Lagnel , and G. Tourillon, Physica B **158**, 282(1989).

Chapter III

1. S.M. Heald, in *X-ray Absorption: Principles, Application, Techniques of EXAFS, SEXAFS and XANES* (eds. Koningsberger, D.C. & Prins, R.), Chapter 3 and 4, (John Wiley, New York, 1988).

2. H. Winick, in *Sychrotron Radiation Research* (eds. Winick, H. & Doniach, S.), Properties of Synchrotron Radiation, (Plenum Press, New York, 1980).

3. D.T. Jiang, N. Alberding, A.J. Seary , and E.D. Crozier, J. Phys. (Paris) Colloq. **47**, C8-825(1986).

4. D.T. Jiang, N. Alberding, A.J. Seary , and E.D. Crozier, Rev. Sci. Instrum. **59**, 60(1987).

5. Kaientai Electronics Merchants Ltd., Vancouver BC, model KP6R2.

6. A.J. Seary, N. Alberding , and E.D. Crozier, SSRL Report No. 83-03(1983).

7. C.E. Bouldin, EXAFS Data Collection on Beamline X23-A2, NSLS, (1989).

8. B.C. Lu and S.A. Rice, J. Chem. Phys. **68**, 5558(1978).

9. D. Sluis and S.A. Rice, J. Chem. Phys. **79**, 5658(1983).

10. L. Bosio, R. Cortes, A. Defrain , and M. Oumezine, J. Non Cryst. Solids **61** & **62**, 697(1984).

11. L. Bosio and M. Oumezine, J. Chem. Phys. **80**, 959(1984)

12. A.H. Weiss, M. Deutsch, A. Braslau, B.M. Ocko , and P.S. Pershan, Rev. Sci. Instrum. **57**, 2554(1986).

13. A. Braslau, *et al.*, Phys. Rev. Lett. **54**, 114(1985).

14. J. Als-Nielsen, Physica B **126**, 145(1984).

15. P.S. Pershan and J. Als-Nielsen, Phys. Rev. Lett. **52**, 759(1984).

16. J.M. Bloch, *et al.*, Phys. Rev. Lett. **54**, 1039(1985).

17. B.A. Bunker, S.M. Heald , and J. Tranquada, in *EXAFS and Near Edge Structure III* (eds. Hodgson, K.O., Hedman, B. & Penner-Hahn, J.E.), EXAFS Investigations of Ion-Implanted Si Using Fluorescence Detection and a Grazing-incidence X-Ray Beam, 482-483 (Springer-Verlag, Berlin, 1984).

18. ORIEL Encoder MIKETM Actuator, Model 18212.

19. D.T. Jiang and E.D. Crozier, Nucl. Instru. A **294**, 666(1990).

20. J. Goulon, C. Goulon-Ginet, R. Cortes , and J.M. Dubois, J. Phys. (Paris) **43**, 539(1982).

21. K.R. Bauchspiess and E.D. Crozier, in *EXAFS and Near Edge Structure III* (eds. Hodgson, K.O., Hedman, B. & Penner-Hahn, J.E.), Crystal Glitches of X-ray Monochromators, (Springer-Verrlag, Berlin, 1984).

22. Z.U. Rek, G.S. Brown , and T. Troxel, in *EXAFS and Near Edge Structure III* (eds. Hodgson, K.O., Hedman, B. & Penner-Hahn, J.E.), Analysis and Application of Multiple Diffraction Phenomena in Perfect Crystal Monochromators, (Springer-Verlag, Berlin, 1984).

23. C.E. Bouldin, A. Carter, J. Kirkland , and R. Neiser, Physica B **158**, 339-341(1989).

24. C.E. Bouldin, R.A. Forman , and M.I. Beli, Rev. Sci. Inst. **58**, 1891(1987).

25. E.A. Stern, W.T. Elam, B.A. Bunker, K.Q. Lu , and S.M. Heald, Nulc. Instru. and Methods **95**, 345-346(1982).

26. F. Lytle, (unpublished).

27. P. Bandyopadhyay and B.A. Bunker, Physica B **158**, 653(1989).

28. H. Oyanagi, *et al.*, Physica B **158**, 694(1989).

29. C.E. Bouldin, R.A. Forman , and M.I. Bell, Phys. Rev. B **35**, 1429(1987).

30. S.M. Heald, in *X-Ray Absorption: Principles, Applications, Techniques of EXAFS, SEXAFS and XANES* (eds. Koningsberger, D.C. & Prins, R.), Chapter 4, (JOHN WILEY & SONS, 1988).

Chapter IV

1. see for example: A. Zangwill, *Physics at Surfaces* , (Cambridge University Press, New York, 1988).

2. S.T. Purcell, Ph.D. Thesis, Simon Fraser University, (1989).

3. K.B. Urquhart, Ph.D. Thesis, Simon Fraser University, (1989).

4. for example: L.E. Davis, N.C. MacDonald, P.W. Palmberg, G.E. Riach , and R.E. Weber, *Handbook of Auger Electron Spectroscopy, Physical Electronics* , (Perkin-Elmer, Eden Prairie Minnesota, 1978).

5. M.P. Seah and W.A. Dench, Surface and Interface Analysis **1**, 2(1979).

6. S.T. Purcell, A.S. Arrott , and B. Heinrich, J. Vac. Sci. Technol. B **6**, 794(1988).

7. J.H. Neave, B.A. Joyce, P.J. Dobson , and N. Norton, Appl. Phys. A **31**, 1(1983).

8. S.T. Purcell, B. Heinrich , and A.S. Arrott, Phys. Rev. B **35**, 6458(1987).

9. T. Takeuchi and S. Ikeda, Trans. ISJI **9**, 484(1969).

10. B. Heinrich, A.S. Arrott, J.F. Cochran, C. Liu , and K. Myrtle, J. Vac. Sci. Technol. A **4**, 1376(1985).

11. B. Heinrich, *et al.*, in *Thin Film Growth Techniques for Low-Dimensional Structures* (eds. Farrow, R.F.C., Parkin, S.S.P., Dobson, P.J., Neave, J.H. & Arrott, A.S.), Epitaxial Growths and surface science techniques applied to the case of Ni overlayers on single crystal Fe(001), (Plenum Publishing Corp., 1987).

12. B. Heinrich, *et al.*, Phys. Rev. B **38**, 12879(1988).

13. E. Bauer, in *Techniques of Metals Research* (eds. Bunshah, R.F.), Reflection Electron Diffraction, 502 (Wiley Interscience, New York, 1969).

14. B. Heinrich, A.S. Arrott, J.F. Cochran, C. Liu , and K. Myrtle, J. Vac. Sci. Technol. **4**, 1376(1986).

15. Z.Q. Wang, y.S. Li, F. Jona , and P.M. Marcus, Solie State Comm. **61**, 623-626(1987).

16. G. Zajac, S.D. Bader , and R.J. Friddle, Phys. Rev. B **31**, 4947(1985).

17. D.T. Jiang, N. Alberding, A.J. Seary, B. Heinrich , and E.D. Crozier, Physica B **158**, 662(1989).

18. A.S. Arrott, B. Heinrich, S.T. Purcell, J.F. Cochran , and K.B. Urquhart, J. Appl. Phys. **61**, 3721(1987).

Chapter V

1. B. Heinrich, A.S. Arrott, J.F. Cochran, C. Liu , and K. Myrtle, J. Vac. Sci. Technol. **4**, 1376(1986).

2. Z.Q. Wang, Y.S. Li, F. Jona , and P.M. Marcus, Solie State Comm. **61**, 623-626(1987).

3. P.M. Marcus, V.L. Moruzzi, Z.Q. Wang, Y.S. Li , and F. Jona, (preprint).

4. S.T. Purcell, Ph.D. Thesis, Simon Fraser University, (1989).

5. B. Heinrich, *et al.*, Mat. Res. Soc. Symp. Proc. Vol. **151**, 177(1989).

6. B. Heinrich, *et al.*, Phys. Rev. B **38**, 12879(1988).

7. B. Heinrich, *et al.*, in *Thin Film Growth Techniques for Low-Dimensional Structures* (eds. Farrow, R.F.C., Parkin, S.S.P., Dobson, P.J., Neave, J.H. & Arrott, A.S.), Epitaxial Growths and surface science techniques applied to the case of Ni overlayers on single crystal Fe(001), (Plenum Publishing Corp., 1987).

8. see for example:: A. Bianconi, in *X-Ray Absorption* (eds. Koningsberger, D.C. & Prins, R.), XANES spectroscopy, (Wiley, New York, 1988).

9. J.E. Muller, in *EXAFS and Near Edge Structure III* (eds. Hodgson, K.O., Hedman, B. & Penner-Hahn, J.E.), Band Structure Approach to the X-Ray Spectra of Metals, (Springer-Verlag, Berlin, 1984).

10. P.R. Bevington, *Data Reduction and Error Analysis for the Physical Sciences* , (McGraw-Hill, Yew York, 1969).

11. see for example:: E.O. Brigham, *The Fast Fourier Transform* , (Prentice-Hall, Inc., Englewood Cliffs, New Jersey, 1974).

12. see for example: D.E. Sayers , and B.A. Bunker, in *X-Ray Absorption: Principles, Applications, Techniques of EXAFS, SEXAFS and XANES* (eds. Koningsberger, D.C. & Prins, R.), Chapter 6 DATA ANALYSIS, (Wiley, New York, 1988).

13. G. Martens, P. Rabe, N. Schwentner , and A. Werner, Phys. Rev. Lett. **39**, 1411(1977).

14. T. Sasaki, T. Onda, R. Ito , and N. Ogasawara, Jpn. J. Phys. **25**, 640-643(1986).

15. E.D. Crozier, Physica B **158**, 14(1988).

16. see for example: P.A. Lee, P.H. Citrin, P. Eisenberger , and B.M. Kincaid, Rev. Mod. Phys. **53**, p.769-806(1981).

17. T.M. Hayes , and J.B. Boyce, in *SOLID STATE PHYSICS, Advances in Research and Application Vol.36* (eds. Ehrenreich, H., Seitz, F. & Turnbull, D.), Extended X-Ray Absorption Fine Structure Spectroscopy, (Academic Press, New York, 1982).

18. B.K. Teo, *EXAFS: Basic Principles and Data Analysis* , (Springer-Verlag, Berlin, 1986).

19. see for example: E.A. Stern, in *X-Ray Absorption: Principles, Applications, Techniques of EXAFS, SEXAFS and XANES* (eds. Koningsberger, D.C. & Prins, R.), Chapter 1, (JOHN WILEY & SONS, 1988).

20. J. Mustre de Leon, J.J. Rehr, S.I. Zabinsky , and R.C. Albers, Phys. Rev. B **44**, 4146(1991).

21. K.R. Bauchspiess, Ph.D. thesis, Simon Fraser University, (1990).

22. F.W. Lytle, D.E. Sayers , and E.A. Stern, Physica B **158**, 701(1988).

23. R.W.G. Wyckoff, *Crystal Structures* , (Wiley, New York, 1963).

24. J. Rehr, (private communication).

25. P.A. Lee , and G. Beni, Phys. Rev. B **15**, 2862(1977).

26. E.D. Crozier and A.J. Seary, Can. J. Phys. **59**, 876(1981).

27. E.D. Crozier, R. Ingalls , and J.J. Rehr, in *X-Ray Absorption: Principles, Techniques of EXAFS, SEXAFS and XANES* (eds. Koningsberger, D.C. & Prins, R.), Chapter 9: Amorphous and Liquid Systems, (Wiley, New York, 1988).

28. E. Sevillano, H. Meuth , and J.J. Rehr, Phys. Rev. B **20**, 4908-4911(1979).

29. F.H. Herbstein, Adv. Phys. 313(1961).

30. W.H. McMaster, N. Kerr Del Grande , and J.H. Mallet, *Compilation of X-ray Cross Sections* , (National Technical Information Service, Springfield, 1969).

31. J. Mustre, Y. Yacoby, E.A. Stern , and J. Rehr, Phys. Rev. B **42**, 10843(1990).

32. B.A. Bunker, S.M. Heald , and J. Tranquada, in *EXAFS and Near Edge Structure III* (eds. Hodgson, K.O., Hedman, B. & Penner-Hahn, J.E.), EXAFS Investigations of Ion-Implanted Si Using Fluorescence Detection and a Grazing-incidence X-Ray Beam, 482-483 (Springer-Verlag, Berlin, 1984).

33. S.M. Heald, H. Chen , and J.M. Tranquada, Phys. Rev. B **38**, 1016(1988).

34. S.M. Heald , and E.V. Barrera, J. Mater. Res. **6**, 935(1991).

35. J.M. Poate, K.N. Tu , and J.W. Mayer, in *Thin Films - Interdiffusion and Reactions* (eds. Poate, J.M., Tu, K.N. & Mayer, J.W.), An Overview, (John Wiley & Sons, New York, 1978).

36. D.T. Jiang, N. Alberding, A.J. Seary, B. Heinrich , and E.D. Crozier, Physica B **158**, 662(1989).

37. T.K. Sham and R.G. Carr, J. Chem. Phys. **83**, 5914(1985).

38. F.W. Lytle and R.B. Greegor, Phys. Rev. B **37**, 1550(1988).

Chapter VI

1. B. Heinrich, *et al.*, Phys. Rev. B **38**, 12879(1988).

2. B. Heinrich, (private communication).

3. B. Heinrich, *et al.*, Phys. Rev. Lett. **64**, 673(1990).

4. D.T. Jiang, E.D. Crozier , and B. Heinrich, Phys. Rev. B **44**, (1991).

5. W.F. Egelhoff Jr., I. Jacob, J.M. Rudd, J.F. Cochran , and B. Heinrich, J. Vac. Sci. Technol. A **8**, 1582(1990).

6. F. Herman, J. Sticht , and M. Van Schilfgaarde, J. Appl. Phys. **69**, 4783(1991).

7. K.R. Bauchspiess , and E.D. Crozier, in *EXAFS and Near Edge Structure III* (eds. Hodgson, K.O., Hedman, B. & Penner-Hahn, J.E.), Crystal Glitches of X-ray Monochromators, (Springer-Verrlag, Berlin, 1984).

8. S.M. Heald, H. Chen , and J.M. Tranquada, Phys. Rev. B **38**, 1016(1988).

9. R.C. Albers, A.K. McMahan , and J.E. Muller, Phys. Rev. B **38**, 3435(1985).

10. J.E. Muller , and W.L. Schaich, Phys. Rev. B **27**, 6489(1983).

11. J.E. Muller , and J.W. Wilkins, Phys. Rev. B **27**, 4331(1984).

12. J.J. Rehr, R.C. Albers, C.R. Natoli , and E.A. Stern, Phys. Rev. B **34**, 4350(1986).

13. G.N. Greaves, P.J. Durham, G. Diakun , and P. Quinn, Nature **294**, 139(1981).

14. W.H. McMaster, N. Kerr Del Grande , and J.H. Mallet, *Compilation of X-ray Cross Sections* , (National Technical Information Service, Springfield, 1969).

15. G. Martens, P. Rabe, N. Schwentner , and A. Werner, Phys. Rev. Lett. **39**, 1411(1977).

16. R.W.G. Wyckoff, *Crystal Structures* , (Wiley, New York, 1963).

17. see for example: E.A. Stern, in *X-Ray Absorption: Principles, Applications, Techniques of EXAFS, SEXAFS and XANES* (eds. Koningsberger, D.C. & Prins, R.), Chapter 1, (JOHN WILEY & SONS, 1988).

18. for a summary of earlier works on this see: J. Stohr, in *X-Ray Absorption: Principles, Applications, Techniques of EXAFS, SEXAFS and XANES* (eds. Koningsberger, D.C. & Prins, R.), Chapter 10, p.462 (JOHN WILEY & SONS, 1988).

19. J. Stohr, in *X-Ray Absorption: Principles, Applications, Techniques of EXAFS, SEXAFS and XANES* (eds. Koningsberger, D.C. & Prins, R.), Chapter 10, 487 (JOHN WILEY & SONS, 1988).

20. W.F. Egelhoff Jr., (private communication).

21. A.R. Miedema , and J.W.F. Dorleijn, Surf. Sci. **95**, 447(1980).

22. D.A. Steigerwald and W.F. Egelhoff Jr., Surf. Sci. **192**, L887(1987).

23. W.F. Egelhoff Jr. and I. Jacob, Phys. Rev. Lett. **62**, 921(1989).

24. D.A. Steigerwald and W.F. Egelhoff Jr., Phys. Rev. Lett. **60**, 2558(1988).

25. see for example: W.F. Egelhoff Jr., CRC Crit. Rev. Solid State Mater. Sci. **16**, 3(1990).

26. T.K. Sham and J. Hrbek, (private communication).

Chapter VII

1. B. Heinrich, *et al.*, Phys. Rev. B **38**, 12879(1988).

2. B. Heinrich, *et al.*, Phys. Rev. Lett. **64**, 673(1990).

3. F. Herman, J. Sticht , and M. Van Schilfgaarde, J. Appl. Phys. **69**, 4783(1991).

4. Z. Celinski, *et al.*, Phys. Rev. Lett. **65**, 1156(1990).